

**A scalable analytic model for single event upsets in radiation-hardened field
programmable gate arrays in the PHENIX interaction region**

by

Steven Eugene Skutnik

A thesis submitted to the graduate faculty
in partial fulfillment of the requirements for the degree of
MASTER OF SCIENCE

Major: Nuclear Physics

Program of Study Committee:
John G. Lajoie, Major Professor
Craig Ogilvie
Kevin De Laplante

Iowa State University

Ames, Iowa

2005

Copyright © Steven Eugene Skutnik, 2005. All rights reserved.

Graduate College
Iowa State University

This is to certify that the master's thesis of
Steven Eugene Skutnik
has met the thesis requirements of Iowa State University

Major Professor

For the Major Program

TABLE OF CONTENTS

LIST OF TABLES	vi
LIST OF FIGURES	viii
1 INTRODUCTION	1
2 BACKGROUND AND EXPERIMENTAL MOTIVATION	3
2.1 Experimental motivation for considering rad-hard FPGA designs	3
2.1.1 Advantages of FPGA-based solutions over traditional ASIC designs	3
2.1.2 Advances in rad-tolerant designs	4
2.2 Challenges to FPGA designs in radiation-hostile environments	5
2.2.1 Introduction	5
2.2.2 Single Event Upset (SEU)	6
2.2.3 Sources of SEU failures	9
2.2.4 Other failure modes: Single Event Fault Interrupt (SEFI), Single Event Transient (SET), and Latchup (SEL)	12
2.2.5 Long-term effects of radiation damage	14
2.3 Mitigating radiation-induced upsets	16
2.3.1 Triple module redundancy with voting	16
2.3.2 Eliminating half-latch vulnerabilities	16
2.3.3 SEU detection and repair with partial reconfiguration	18
2.3.4 SEU resistance from transistor body ties	19
2.4 Summary	20
3 EXPERIMENTAL BACKGROUND AND SETUP	22
3.1 Introduction	22
3.2 Device under test	22
3.3 Data Acquisition and Monitoring	23

3.3.1	FIVIT software and SEU measurement	23
3.3.2	Data acquisition procedure	24
3.3.3	Online monitoring and analysis	25
3.4	Dosimetry measurements	25
3.4.1	Introduction	25
3.4.2	Dose as measured by TLD badge	25
3.5	Observed SEU rate as a function of integrated luminosity	26
3.6	Summary	28
4	DETAILED EVALUATION OF THE PISA MODEL CALCULATIONS	29
4.1	Overview of PISA model	29
4.1.1	Introduction to PISA	29
4.1.2	Assumptions used in PISA model	30
4.1.3	Simulation details	31
4.2	Calculation of absorbed dosages	32
4.2.1	Use of dosimetry badges in the experiment	33
4.2.2	Overview of key concepts in radiation dosimetry	33
4.2.3	Dose from γ radiation	34
4.2.4	Dose from neutrons	36
4.2.5	Comparison of predicted doses to measured TLD values	38
4.3	Calculated particle fluences and momenta spectra from PISA model	40
4.3.1	Particle fluences by type	40
4.3.2	Momentum spectra for selected particle types	45
4.4	Summary	54
5	PREDICTIONS AND ANALYSIS OF RESULTS FROM PISA MODEL	57
5.1	Estimation of SEU cross-section contribution of individual particles by particle type	58
5.1.1	Estimation of a Weibull curve for neutrons based upon integrated cross-section data	58
5.1.2	Calculation of SEU cross-section contribution for other particle species	63
5.1.3	Relative SEU cross-section contribution for various particle types in PISA model	65
5.2	Comparison of observed SEU rates to predicted rates	66
5.3	Comparison of SEU cross-section contribution of various particle types to internal ion fragmentation	68

5.4	Evaluation of systematic errors within PISA model	70
5.5	Remaining sources of uncertainty	71
5.5.1	Contribution from thermal neutrons	71
5.5.2	Uncertainties in particle generation within PISA	72
5.5.3	Variances from the experimental geometry in the PISA model	72
5.5.4	SEU cross-section scaling	73
5.6	Areas for improvement within experiment	73
5.7	Summary	74
6	CONCLUSION	77
6.1	Estimating SEU rates per fill from luminosity data	77
6.2	Comparison of predicted SEU rates as a function of fill time	79
6.3	Probability of concurrent TMR failure	83
6.4	Estimating per-fill dose rates	84
6.5	Summary	85
	APPENDIX A CALCULATION OF MINIMUM-Z FOR THRESHOLD $\frac{dE}{dx}$ USING THE BETHE-BLOCH FORMULA	86
	APPENDIX B DETAILS OF MONTE CARLO CALCULATIONS	89
	BIBLIOGRAPHY	96
	ACKNOWLEDGMENTS	99

LIST OF TABLES

Table 3.1	Measured results from TLD badges in human-equivalent rem dose.	26
Table 3.2	Corrected TLD results in rem/event.	26
Table 3.3	Chronological Summary of SEUs ($r = 250$ cm).	27
Table 3.4	Chronological Summary of SEUs ($r = 53$ cm).	27
Table 4.1	$(1 - g)$ values for photon absorption from [1].	35
Table 4.2	Comparison of measured human-equivalent radiation dose by TLD badges to dose calculated by PISA for $r = 53$ cm (rem/event).	39
Table 4.3	Comparison of measured human-equivalent radiation dose by TLD badges to dose calculated by PISA for $r = 250$ cm (rem/event).	39
Table 4.4	GEANT Particle ID types.	41
Table 5.1	Neutron SEU cross-sections per device for a Xilinx Virtex-II family device, as measured by iRoC [2] and Xilinx [3].	60
Table 5.2	Predicted SEU cross-section values for a Virtex II-family device from a minimized Weibull-form fit to Xilinx and iRoC data, with offsets from measured values.	61
Table 5.3	Predicted SEU cross-section values for a Virtex II-family device from a minimized linear fit to Xilinx and iRoC data, with offsets from measured values.	61
Table 5.4	Fractional SEU cross-section contribution by particle type for the near and far positions in PISA.	63
Table 5.5	SEU statistics for events observed in experiment and predicted values from PISA. (Integrated luminosity values are measured in counts).	66

Table 5.6	Statistical evaluation of upsets in the experiment and model. Given are the mean number of upsets over the measured interval for the experiment, from the model, the σ value from the Poisson distribution, and the probability of the experimentally observed number of upsets based upon the predicted values from the model.	67
Table 5.7	Ratio of heavy ion production for individual particle type to that of protons, as compared to luminosity ratio by particle type scaled by average nuclear interaction cross-section ratio, $r = 53$ cm.	68
Table 5.8	Ratio of heavy ion production for individual particle type to that of protons, as compared to luminosity ratio by particle type scaled by average nuclear interaction cross-section ratio, $r = 250$ cm.	69
Table 5.9	Tabulation of systematic errors in the predicted SEU cross-section for various aspects of the PISA model.	71
Table 5.10	Comparison of SEU rate for the PISA simulation with and without the Aluminum heatsink layer.	73
Table 6.1	Fit parameters for the ZDC rate distribution as a function of time for fits with $\tilde{\chi}^2 < 2.5$	77
Table 6.2	Mean SEUs per fill for the design under test with 16,394,483 configuration logic bits, assuming a 4-hour fill with a typical RHIC I and RHIC II luminosity profile.	82
Table 6.3	Probability of a concurrent TMR failure for the design under test with 16,394,483 configuration logic bits, assuming a 4-hour fill with a typical RHIC I and RHIC II luminosity profile.	84
Table 6.4	Doses from charged particles (calculated from PISA) and from gammas and neutrons as measured by attached TLD badges, converted to radiation-absorbed dose per event (rad/event).	84
Table 6.5	Mean total ionizing dose (TID) for RHIC I and RHIC II fills, for both near and far positions (rad/fill).	85
Table A.1	Minimum Z required to achieve LET_{th} as a function of β for Xilinx Q-Pro and comparable Actel series of rad-hardened FPGAs.	88
Table B.1	SEU rate predictions from 10,000 events in the simple Monte Carlo for the two annular positions.	94

LIST OF FIGURES

Figure 2.1	Per-bit SEU cross-section for Xilinx devices as a function of feature size for neutrons [3]. Note that newer technologies are marked by decreasing feature size (i.e., leftward on the axis). Series 1 and 2 indicate testing of the various Xilinx models from atmospheric neutrons with the Rosetta board and accelerated neutron testing at LANSCE, respectively.	5
Figure 2.2	Diagram of critical nodes within an FPGA circuit [3].	6
Figure 2.3	Example of heavy ion creation (and resulting ionization) within the Silicon die by inelastic scattering neutrons with the Silicon nuclei [3].	7
Figure 2.4	Example of a neutron-induced Silicon nuclear “recoil” reaction, resulting in heavy local ionization which can serve as a source of single event upsets [4]. . .	7
Figure 2.5	SEU cross-section for configuration bits as a function of proton energy [5]. . . .	8
Figure 2.6	Example of a mux select failure [6].	9
Figure 2.7	Diagram of PIP short and open failures [6].	10
Figure 2.8	Diagram of buffer short and open failures [6].	11
Figure 2.9	Example of a LUT upset failure [6].	11
Figure 2.10	Diagram of Virtex programmable inversion bits, labeled V, E, F, and G [6]. . .	12
Figure 2.11	POR SEFI cross-section for a Virtex II family device for protons [5].	13
Figure 2.12	Example of a single event latchup condition [7].	14
Figure 2.13	Simplified energy-band diagram of a semiconductor. a) Before radiation damage, carriers are directly promoted across the band gap from the valence band to the conduction band, b) After exposure to ionizing radiation, defects in the lattice give rise to “trap states” in the mid-gap region which must be filled entirely before carriers can be promoted to the conduction band.	15

Figure 2.14	Top: Illustration of intended constant “1” value (V_{cc}) and its half-latch implementation. Bottom: Example of half-latch vulnerability to a proton-induced upset [8].	17
Figure 2.15	SEU-resistant alternative to the half-latch reliant design shown in Figure 2.14. The constant value for clock enable (CE) is now driven by a separate flip-flop (PRE asynchronously set to “1”) which can self-correct when upset [8].	18
Figure 2.16	Example schematic of body ties on an SOI-MOS transistor [9].	19
Figure 2.17	Diagram of an SRAM circuit with feedback resistors R and capacitors C added to draw off radiation-induced currents. Gates are denoted as G, sources as S, and drains as D [9]. This strategy is similar to the design employed by Actel’s internal charge pump design [10], which is designed to drain off radiation-induced leakage currents.	20
Figure 2.18	Cross-section curves for SRAM device with and without body tie circuit [9]. . .	21
Figure 3.1	Picture of the test box setup (left) attached to the frame of the GEM detector (right) in the PHENIX IR.	23
Figure 3.2	Screen shot of FIVIT software (Xilinx).	24
Figure 3.3	Observed upsets as a function of integrated luminosity, ($r = 250$ cm)	27
Figure 3.4	Observed upsets as a function of integrated luminosity, ($r = 53$ cm)	28
Figure 4.1	Diagram of PISA geometry used for purposes of simulation (not drawn to scale).	31
Figure 4.2	GEANT rendering of sample geometry used for simulations (drawn to scale).	32
Figure 4.3	Graph of C_k fit used for purposes of calculating shallow-depth photon dose [1].	36
Figure 4.4	Graph of C_k fit used for purposes of calculating lens-depth photon dose [1].	37
Figure 4.5	Graph of C_k fit used for purposes of calculating deep-depth photon dose [1].	37
Figure 4.6	Graph of human-equivalent dose for neutrons (in rem) extracted from 10CFR835, as a function of neutron energy (in MeV) [11].	38
Figure 4.7	GEANT partIDs for particles incident upon the chip in PISA at $r = 53$ cm.	42
Figure 4.8	GEANT partIDs for particles incident upon the chip in PISA at $r = 250$ cm.	43
Figure 4.9	GEANT particle IDs for particle tracks in PISA originating inside the silicon annular region at $r = 53$ cm.	43
Figure 4.10	GEANT particle IDs for particle tracks in PISA originating inside the silicon annular region at $r = 250$ cm.	44

Figure 4.11	GEANT parent partIDs for heavy particle fragments (PID > 40) created inside the annular region at $r = 53$ cm.	44
Figure 4.12	GEANT parent partIDs for heavy particle fragments (PID > 40) created inside the annular region at $r = 250$ cm.	45
Figure 4.13	Momentum distribution of protons and anti-protons incident upon the annular region at $r = 53$ cm.	46
Figure 4.14	Momentum distribution of protons and anti-protons incident upon the annular region at $r = 250$ cm.	46
Figure 4.15	Origin of low-momentum ($p < 200$ MeV) protons and anti-protons incident upon the annular region at $r = 53$ cm.	47
Figure 4.16	Origin of low-momentum ($p < 200$ MeV) protons and anti-protons incident upon the annular region at $r = 250$ cm.	48
Figure 4.17	Momentum distribution of neutrons and anti-neutrons incident upon the annular region at $r = 53$ cm.	48
Figure 4.18	Momentum distribution of neutrons and anti-neutrons incident upon the annular region at $r = 250$ cm.	49
Figure 4.19	Origin coordinates of neutrons incident upon the annular region at $r = 53$ cm. .	50
Figure 4.20	Origin coordinates of neutrons incident upon the annular region at $r = 250$ cm.	50
Figure 4.21	Momentum distribution of neutrons originating from the magnet media incident upon the annular region $r = 53$ cm.	51
Figure 4.22	Momentum distribution of neutrons originating from the magnet media incident upon the annular region $r = 250$ cm.	51
Figure 4.23	Momentum distribution for neutrons/anti-neutrons with child particles created inside the annular region.	52
Figure 4.24	Momentum distribution of kaons incident upon the annular region at $r = 53$ cm.	53
Figure 4.25	Momentum distribution of kaons incident upon the annular region at $r = 250$ cm.	53
Figure 4.26	Momentum distribution of pions incident upon the annular region at $r = 53$ cm.	54
Figure 4.27	Momentum distribution of pions incident upon the annular region at $r = 250$ cm.	55
Figure 4.28	Origin of low-momentum ($p < 200$ MeV) pions incident upon the annular region at $r = 53$ cm.	55
Figure 4.29	Origin of low-momentum ($p < 200$ MeV) pions incident upon the annular region at $r = 250$ cm.	56

Figure 5.1	Graph of LANSCE neutron spectrum as compared to atmospheric Hess spectrum [2].	59
Figure 5.2	Comparison of minimized Weibull SEU cross-section distribution fit with systematic errors from parameter fitting (red) to linear SEU cross-section fit (blue). 14 MeV neutron cross-section as measured by iRoC is also plotted with corresponding systematic errors [2]. Cross-section is given in $\text{cm}^{-2} \cdot \text{bit}^{-1}$	62
Figure 5.3	Comparison of Weibull distribution for protons from Xilinx [5] (black), as compared to the estimated cross-section for anti-protons, estimated from the nuclear interaction cross-section ratio to protons.	64
Figure 5.4	Comparison of Weibull distribution for protons from Xilinx [5] (black), as compared to the estimated cross-section for π^- (red) and π^+ (blue), estimated from the nuclear interaction cross-section ratio to protons.	64
Figure 5.5	Comparison of Weibull distribution for protons from Xilinx [5] (black), as compared to the estimated cross-section for K^- (red) and K^+ (blue), estimated from the nuclear interaction cross-section ratio to protons.	65
Figure 6.1	Sample fit to PHENIX ZDC data with two exponential terms ($\chi^2 = 0.4162$). . .	78
Figure 6.2	Comparison of RHIC fill luminosity as a function of fill time without electron cooling (lower), to RHIC fill luminosity with electron cooling (upper) [12]. . . .	79
Figure 6.3	Mean SEUs per bit, per device as a function of fill time for Q-Pro Virtex II device in a RHIC I fill with initial luminosity of 14 KHz, far position ($r = 250$ cm). Black, solid: Mean (aggregate) Blue, filled: σ ; Red, filled: Predicted (with systematic errors).	80
Figure 6.4	Mean SEUs per bit, per device as a function of fill time for Q-Pro Virtex II device in a RHIC I fill with initial luminosity of 14 kHz, near position ($r = 53$ cm). Black, solid: Mean (aggregate) Blue, filled: σ ; Red, filled: Predicted (with systematic errors).	80
Figure 6.5	Mean SEUs per bit, per device as a function of fill time for Q-Pro Virtex II device in a RHIC II fill with a mean luminosity of ≈ 60 kHz, far position ($r = 250$ cm). Black, solid: Mean (aggregate) Blue, filled: σ ; Red, filled: Predicted (with systematic errors).	81

Figure 6.6	Mean SEUs per bit, per device as a function of fill time for Q-Pro Virtex II device in a RHIC II fill with a mean luminosity of ≈ 60 kHz, near position ($r = 53$ cm). Black, solid: Mean (aggregate) Blue, filled: σ ; Red, filled: Predicted (with systematic errors).	81
Figure 6.7	Table of Xilinx's Q-Pro radiation-hardened line of FPGAs, including the maximum number of configuration logic bits available for designs and the maximum rated ionizing dose (kRads) [13].	82

DEDICATION

To my parents, Eugene and Rita Skutnik, who have always supported me in all of my endeavors. I would not be where I am were it not for their steadfast encouragement.

To Anne, who showed unwavering faith in me even when I doubted myself the most, and who sat through many a physics lesson with patience, grace, and love - all for my sake.

And to John, who has throughout the years served in the roles of adviser, teacher, and friend. Everything I have learned about being a scientist I owe to him.

1 INTRODUCTION

Given the remarkable success of reprogrammable logic devices in areas such as telecommunications, aerospace, and defense applications, it is only natural that an interest should arise in their use for on-detector electronics solutions as well. However, while such devices present numerous advantages in terms of design flexibility, they come with the drawback of being susceptible to bit upsets induced by radiation, more commonly known as “single events upsets” (or SEUs).

While the SEU cross-section has been extensively tested for the particle flux types most commonly seen in aerospace applications (for example, atmospheric neutrons, protons, and heavy ions), few if any tests have been conducted within an actual detector environment. Thus, chief among the aims of this thesis is to present a scalable analytical model for simulating the radiation dosage for a given region in the interaction region (IR) in the PHENIX detector at the Relativistic Heavy Ion Collider (RHIC) at Brookhaven National Laboratory, and from this the SEU rate in a given device.

Two measures of the model’s quality shall be conducted. The first of these shall be a comparison of the calculated dose from the model of gammas and neutrons, as compared to the dose measured by two dosimetry badges which were attached to the device under test. These doses will give a “sanity check” to measure if the PISA model can accurately measure the radiation dose within the IR, and thus whether the predictions from such a model give an accurate picture of the actual PHENIX environment. Then, the predicted SEU rates from such a model will be compared to those observed from experiment, with appropriate attention being given to statistical and systematic errors in both the experiment and model.

The primary purpose of such a study would to characterize the nature of the radiation environment within PHENIX. Such a model would then ultimately be used to create a better understanding of single event upsets induced in a hypothetical FPGA in the IR; an issue of particularly importance in considerations for future experiments and detector upgrades. Ultimately, such a model would also provide a means of evaluating the feasibility of using field programmable gate arrays (FPGAs) to replace traditional ASIC components in on-detector electronics.

The benefits of such a design change would be twofold: first, in design flexibility, as FPGAs can be redesigned and reprogrammed on the fly, thus enabling design corrections and updates which would be cost prohibitive in a traditional ASIC implementation. In addition, radiation-tolerant FPGA solutions may offer considerable cost savings depending upon the number of units needed, as rad-hard FPGAs can be bought commercially for a fraction of the price of custom-cast ASIC designs purchased in relatively small quantities.

Over the course of 19 days, a VHDL-based implementation of a digital ALICE Pixel pilot module implemented by Jonathan Crandall [14] was used to program a XQR2V6000 rad-hard FPGA prototype provided by Xilinx, which was placed in the IR of the PHENIX detector at RHIC. Testing occurred at two locations: approximately 250 cm below the collision vertex as well as approximately 53 cm below. Meanwhile, the chip was checked at regular intervals for single event upsets induced by radiation exposure using software provided by Xilinx.

2 BACKGROUND AND EXPERIMENTAL MOTIVATION

In this section I shall present the motivation for pursuing this experiment, including the advantages and challenges involved in pursuing rad-tolerant FPGA solutions for on-detector electronics as well as an overview of the dominant issue of SEUs and several techniques for mitigating these effects. While much of what is to be discussed will be of relevance to all types of rad-hardened programmable logic devices, of chief focus will be the data available from Xilinx, as of this time they are the only manufacturer offering the reprogrammable devices with the level of radiation tolerance necessary for this experiment¹.

2.1 Experimental motivation for considering rad-hard FPGA designs

Given the advantages of FPGA-based designs already seen for detector electronics outside the IR, considerable interest has arisen toward investigating the feasibility of using such designs in on-detector electronics within the IR environment. This provoked a study of the current state in radiation-tolerant FPGA devices and their feasibility for use within the PHENIX IR, whose advantages shall be discussed in this section.

2.1.1 Advantages of FPGA-based solutions over traditional ASIC designs

Reprogrammable logic devices have already demonstrated themselves to be most useful on several PHENIX subsystems outside of the actual IR, most notably on the Level-1 Trigger. Given their ability to be inexpensively prototyped and tested within the design software before ever being deployed, they make an ideal alternative to traditional ASIC designs, which require significant lead time when ordered from a foundry and come at considerable expense in small orders.

As an additional benefit, this flexibility in design also yields the advantage of giving such devices a considerably longer usable life within the experiment, as the same hardware can be updated and extended for newer and more sophisticated functions as both engineering and physics considerations

¹Logic manufacturer Actel, for instance, produces a line of rad-tolerant programmable logic devices which will be discussed in brief, however these lack the comparable ability to be reprogrammed once set. This in turn eliminates many of its advantages when compared to the unlimited reprogrammability features of Xilinx's own rad-tolerant offerings.

dictate. This has proven especially true for the Level-1 trigger subsystems, where new trigger systems have been deployed using the pre-existing hardware infrastructure.

Likewise, while mistakes in engineering prove highly costly in traditional ASIC designs, in reprogrammable FPGA devices, the solution is as simple as downloading the new configuration into the device - a significantly less expensive alternative. Meanwhile, changes in logic design can be done with the hardware still in place in the experiment - a greatly appreciable advantage in terms of labor and materials costs savings.

Finally, FPGA-based solutions offer an additional protection against radiation damage from the form of cell rupture. For example, if a logic cell were to be destroyed by incident radiation in a traditional ASIC design, the functional portion of such a chip is simply “lost”; there is no way to reroute the design around the damaged portion and recover. The same is not true for static RAM-based FPGAs however, which can be reprogrammed around the damaged logic sections. While cell rupture was not observed in any of Xilinx’s own radiation testing, it nonetheless remains a conceivable possibility which static RAM (SRAM) devices provide an additional protection against [15].

2.1.2 Advances in rad-tolerant designs

While FPGAs present numerous advantages in terms of cost and design flexibility, until recently their usefulness in on-detector electronics has been limited due to the adverse effects of radiation damage. Recent advances in radiation hardening technology have begun to moot these concerns, with Xilinx’s latest series of Q-Pro rad-hardened devices² having a minimum total integrated dose tolerance of 200 kRad, well beyond the dose any given device may experience within its useful life in the PHENIX IR. Likewise, comparable device offerings from Actel’s RTAX-S rad-tolerant FPGA offerings³ advertise a total integrated dose (TID) tolerance of up to 300 kRad [18].

Additionally, in terms of single event latchup (a condition under which a heavy ion strike creates a “short” on an internal transistor from VDD to VSS, resulting in a parasitic feedback loop which can potentially damage the device until the power is cycled), both lines of products show latchup immunity to very high values of $\frac{dE}{dx}$ (known more commonly in engineering applications as linear energy transport, or simply LET), which is a measure of the energy deposited in a material through the energy lost by incident ionizing particles. Xilinx’s Q-Pro line advertises a latch-up immunity up to $120 \frac{\text{MeV}\cdot\text{cm}^2}{\text{mg}}$, while Actel’s RTAX-S series guarantees latchup immunity for $\frac{dE}{dx}$ values up to $63 \frac{\text{MeV}\cdot\text{cm}^2}{\text{mg}}$ [7, 18].

²For more on Xilinx’s QPro line of rad-hardened devices, see [16].

³For more information on Actel’s rad-hard offerings, see [17].

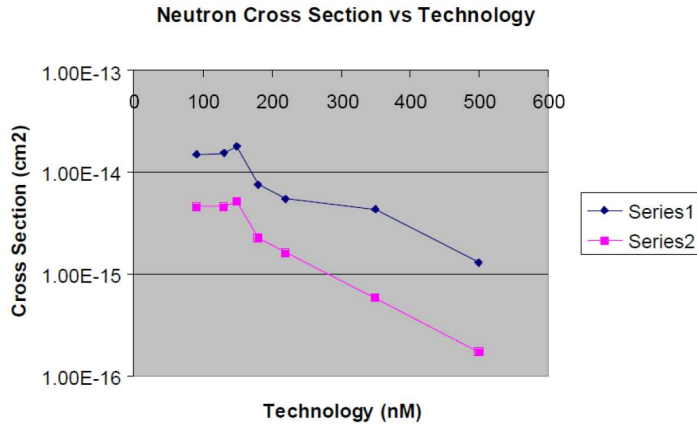


Figure 2.1 Per-bit SEU cross-section for Xilinx devices as a function of feature size for neutrons [3]. Note that newer technologies are marked by decreasing feature size (i.e., leftward on the axis). Series 1 and 2 indicate testing of the various Xilinx models from atmospheric neutrons with the Rosetta board and accelerated neutron testing at LANSCE, respectively.

A quick calculation using the Bethe-Bloch formula⁴ reveals that the minimum Z for a particle assumed to be of $\beta \approx 0.10$ (chosen arbitrarily as to maximize $\frac{dE}{dx}$) to create a latchup condition would be $Z \geq 44$ for the Q-Pro models and $Z \geq 31$ for Actel's comparable line, with this value increasing until the minimum of the $\frac{dE}{dx}$ function around $\beta \approx 0.96$ [19]. The conclusion that can be drawn from this is obvious - a latchup condition caused by interactions with single ionized particles (including α particles and most beam fragments) would be impossible outside of a case of direct exposure to heavier ions from the beam itself, of which the incident particles would be of much higher β and consequently, even lower $\frac{dE}{dx}$.

2.2 Challenges to FPGA designs in radiation-hostile environments

2.2.1 Introduction

Given the current state of radiation-hardening technology as discussed above, the main problems facing FPGA-based solutions in environments like the PHENIX IR are no longer issues directly related to radiation damage (such as eventual current drain and performance losses), but rather more subtle effects such as single event upsets (SEUs).

⁴See Appendix A for more information on the Bethe-Bloch formula and the minimum Z calculation for LET_{th} and a table of minimum Z values to realize LET_{th} as a function of β for each series.

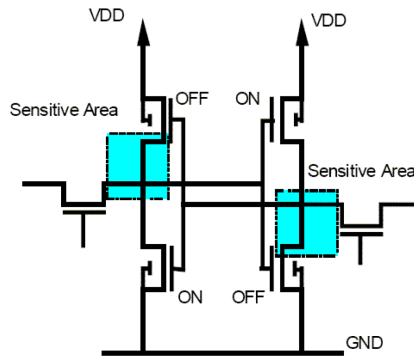


Figure 2.2 Diagram of critical nodes within an FPGA circuit [3].

As Figure 2.1 shows, as chip feature sizes have grown smaller and logic density has increased with new technology, SEU cross-sections due to neutrons and other particles have by contrast steadily climbed (reaching a relative plateau in recent designs). While such effects cannot be eliminated directly, they can be mitigated to a large degree by careful use of design techniques.

In the following sections, I shall discuss the nature of several types of single-event failures in devices due to incident particles as well as discuss strategies for mitigating the effects of these failures. In addition, I shall present an overview of the physical effects of long-term radiation damage and its effect upon device performance.

2.2.2 Single Event Upset (SEU)

Single event upsets are events in which an incident particle can strike key node within a device (Figure 2.2), resulting in a local ionization that can cause a state change in a bit with sufficient voltage [3].

Experiments with similar device types have shown that the minimum free charge required to change the state of a logic cell is approximately 100 fC. Given that the average energy to create an electron-hole pair in the Silicon is 3.6 eV and the average thickness of an active volume of a device is on the order of $2 \mu\text{m}$, an ionization of $1 \frac{\text{MeV}}{\mu\text{m}}$ is required - well beyond the average ionizing energy loss of protons (where $\frac{dE}{dX} \approx 40 \frac{\text{keV}}{\mu\text{m}}$ at an energy of 1 MeV) [20].

Thus, upsets are associated primarily with ion strikes in the Silicon which result in the creation of heavier secondary fragments such as α (Figure 2.3) and through elastic collisions with the Silicon nuclei (Figure 2.4) which result in nuclear “recoils”, leaving a local trail of heavy ionization [3, 4].

Experimental testing by Xilinx at Texas A&M University with their radiation-tolerant devices has yielded SEU (and other fault condition) cross-sections for configuration logic bits for protons and heavy

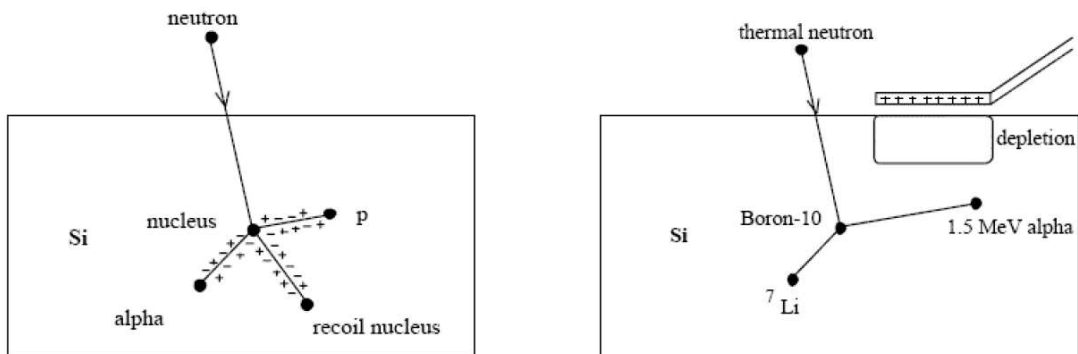


Figure 2.3 Example of heavy ion creation (and resulting ionization) within the Silicon die by inelastic scattering neutrons with the Silicon nuclei [3].

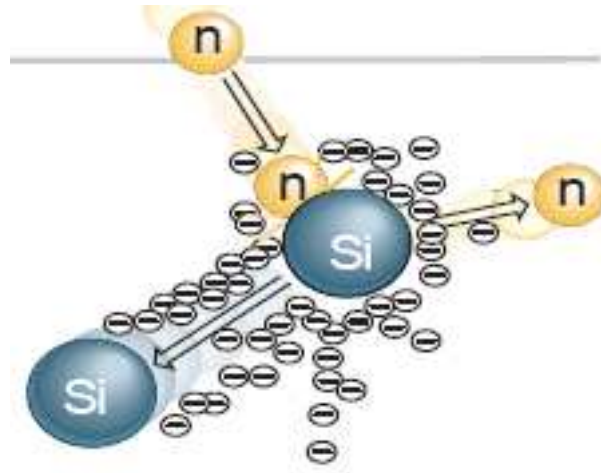


Figure 2.4 Example of a neutron-induced Silicon nuclear “recoil” reaction, resulting in heavy local ionization which can serve as a source of single event upsets [4].

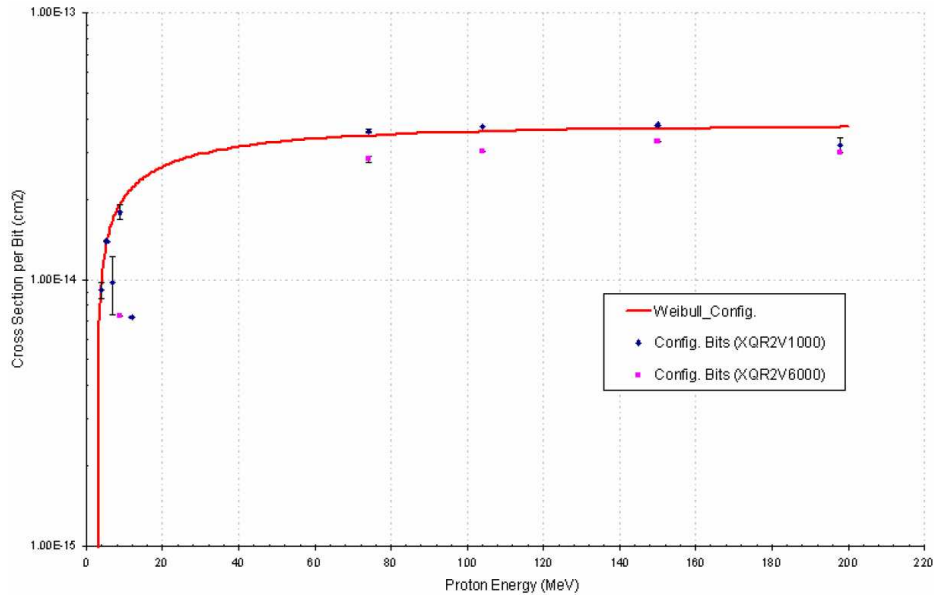


Figure 2.5 SEU cross-section for configuration bits as a function of proton energy [5].

ions, as a function of particle energy [5, 21]. What was observed for protons was that SEU cross-sections can be accurately fitted to a Weibull curve of the following form:

$$F(E_k) = \sigma_{sat} \left(1 - e^{-\left[\frac{(E_k - E_0)}{W}\right]^S} \right) \quad (2.1)$$

where E_k is the incident particle's kinetic energy, E_0 is the onset energy in which the SEU cross-section first appears, W is the “width parameter” and S is a “dimensional exponent” [5].

Neutron cross-sections have also been studied by Xilinx at the Los Alamos Neutron Science Center (LANSCE) as well as at several altitudes to measure the effects of atmospheric neutrons [3]. While the cross-section measurements for neutrons are more limited in scope (results were obtained for neutrons with energy greater than 1.5 MeV and greater than 10 MeV), they nonetheless provide useful information in formulating a model to simulate SEU rates for this experiment. More importantly, this integrated cross-section data (coupled with independent testing data by iRoC technologies, a soft-error testing and mitigation company) will be used in a following chapter to create a Weibull cross-section distribution fit for neutrons, giving a “true” energy-dependent cross-section distribution.

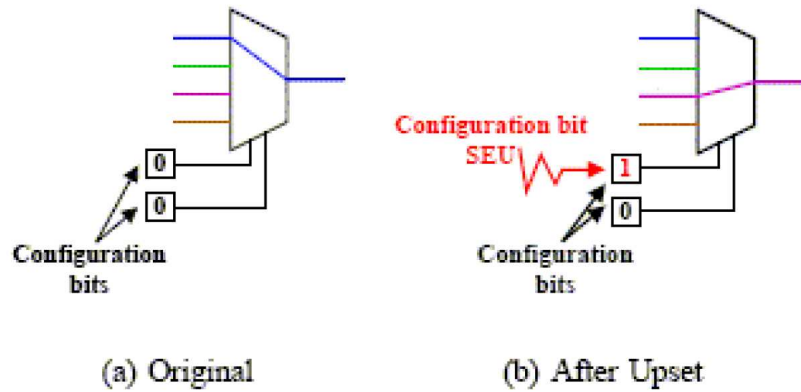


Figure 2.6 Example of a mux select failure [6].

2.2.3 Sources of SEU failures

2.2.3.1 Overview

SEUs in configuration logic blocks (CLBs) can manifest in several forms, each of which resulting in a bit flip in the configuration logic, but all also capable of being mitigated. The following vulnerabilities are specific the to Virtex design by Xilinx, but are illustrative of the general types of failures one might expect in programmable logic devices (PLDs). Such errors fall into two classes: errors in the routing logic and errors in the actual control logic itself.

2.2.3.2 Routing logic errors

The first example of a radiation-induced failure would be of a multiplexer (mux) select failure (Figure 2.6), resulting in an incorrect routing in that part of the chip. As muxes comprise much of the routing logic for an FPGA, they are particularly sensitive to SEUs, as any change in the mux select lines will result in an incorrect routing (assuming it is in a utilized portion of the device) [6].

The next point of vulnerability for a Virtex device is in what is known as a programmable interconnect point (PIP), a pass transistor between two wires which comprises another large part of the routing logic. A PIP can be toggled on or off to an incorrect state by a voltage spike caused by an incident particle (Figure 2.7), causing a short (resulting in power drain and output errors) or an open (breaking the flow of data through the circuit) [6].

The last kind of routing error that can occur is a buffer error, similar to a PIP error except for the fact that the vulnerable component is an active driver rather than a pass transistor (Figure 2.8), with the two types of errors being the same as before, resulting in an “open” or “short” buffer and causing

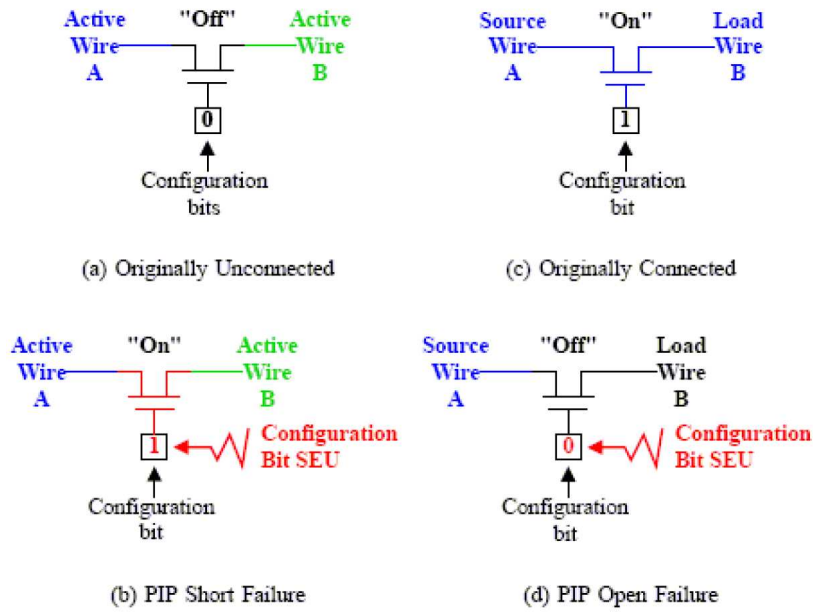


Figure 2.7 Diagram of PIP short and open failures [6].

similar routing problems [6].

2.2.3.3 Control logic failure

The next class of errors that can occur are within the control logic itself. The first of these is a failure in a lookup table (LUT), changing the value of one of the entries on the table itself and resulting in an incorrect logic function. Figure 2.9 gives an example of such a failure with a 4-input “and,” whereupon the resulting change in the LUT results in a constant-“0” function [6]. What should be noted about LUT upsets is that these only change the output bit for one value of the LUT - meaning that the behavior of most inputs will remain unchanged.

Last is the case of a toggling of a control bit, resulting in an inverted signal input and thus possibly radically altering the function of a given circuit, exhibited by Figure 2.10. Unlike the case of a bit upset in a LUT, an upset in a control bit will affect nearly all inputs, and consequently cause errors in almost all cases [6].

Equally important is to quantify the relative frequency of errors as a function of the location within the device. While the relative location of errors depends upon logic utilization and other factors, it was found that in the cases investigated by Xilinx that routing errors comprised 78-85% of all SEU errors, with configuration logic errors making up the rest [6].

Given this, for cases in which logic space is scarce, the relative probability of errors can be used to

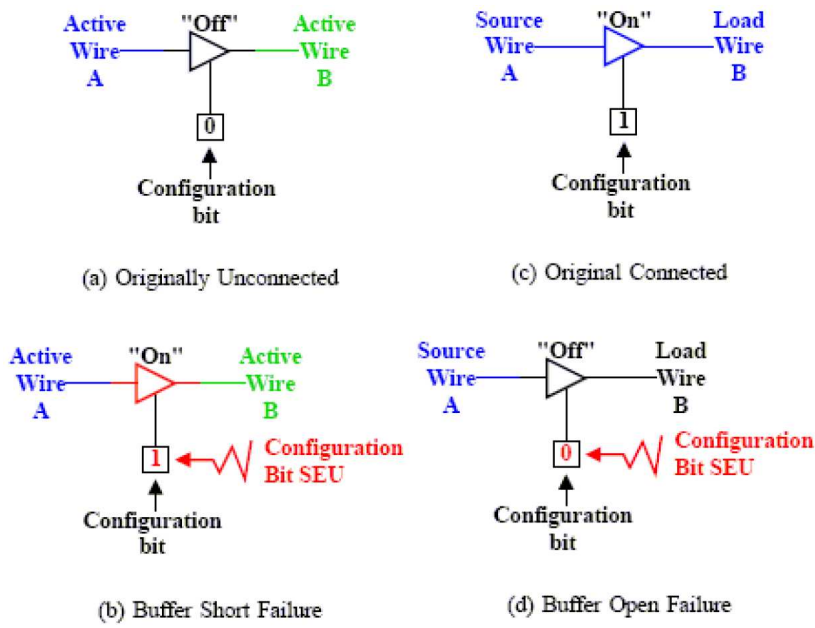


Figure 2.8 Diagram of buffer short and open failures [6].

LUT

1	F1	0	0	0	0	O — 1
1	F2	0	0	0	0	
1	F3	0	0	0	0	
1	F4	0	0	0	0	
1		0	0	0	1	

O=F1*F2*F3*F4

(a) Original 4-input AND Function

LUT

1	F1	0	0	0	0	O — 0
1	F2	0	0	0	0	
1	F3	0	0	0	0	
1	F4	0	0	0	0	
1		0	0	0	0	

O=0 (constant zero)

(b) Upset LUT Function (Constant "0")

Figure 2.9 Example of a LUT upset failure [6].

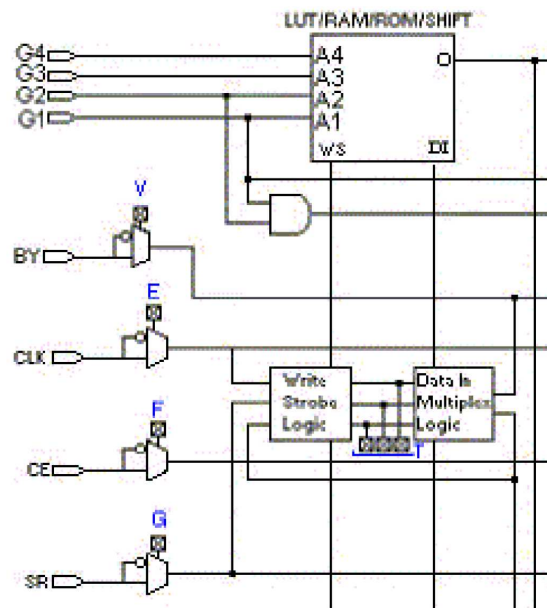


Figure 2.10 Diagram of Virtex programmable inversion bits, labeled V, E, F, and G [6].

determine where to apply SEU mitigation techniques such as triple module redundancy (TMR), which itself requires triple the amount of logic resources as normal to implement. (TMR will be discussed in further detail along with other means of mitigating SEUS in the following section).

2.2.4 Other failure modes: Single Event Fault Interrupt (SEFI), Single Event Transient (SET), and Latchup (SEL)

In addition to static bit upsets in the configuration logic, other (albeit less common) failure modes include single event fault interrupts (SEFI), single event transient (SET), and single event latchup (SEL).

An SEFI is characterized by an event which requires a complete device reconfiguration before normal operation is restored, but not a power cycle (in contrast to latchup, which requires a power cycle, and SEUs, which only require reconfiguration of the affected frame). From experiments, three types of SEFIs have been identified: power on reset (POR), JTAG configuration port (JCFG), and the SelectMap port, each corresponding to a particle striking the appropriate device circuitry [5].

A POR SEFI results in a global reset of all internally stored data and a complete loss of device state. In as much, it will be incapable of processing data until the device is completely reconfigured. Such a SEFI can be identified by the device current, which will undergo a sudden, marked decrease to

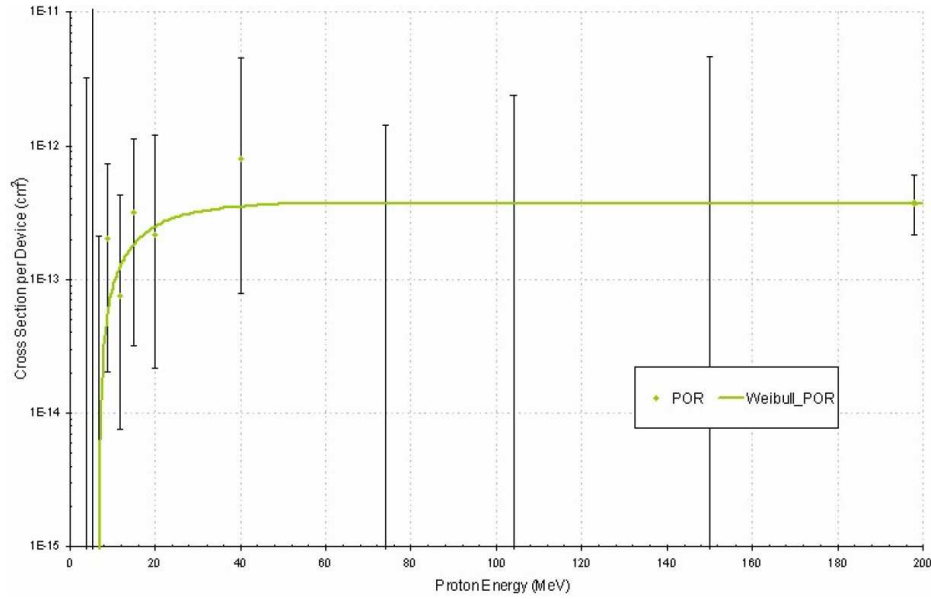


Figure 2.11 POR SEFI cross-section for a Virtex II family device for protons [5].

its initial value [5].

By contrast, JCFG and SelectMap SEFIs only affect control of the device itself by disabling read/write access to the configuration memory, leaving the configuration and state data intact. Both types of upsets can be identified by the data coming from the respective port: a constant value coming from the JCFG port or “junk” data coming from the SelectMap port. While the device can still process data (as the configuration state is unaffected), the user will be unable to perform a partial reconfiguration to scrub bit upsets until the device is taken offline and a full reconfiguration is completed [5]. This and other methods for mitigating SEUs will be discussed in sections that follow.

Figure 2.11 shows measured cross-sections for POR SEFIs for protons. Immediately clear is the fact that the SEFI cross-section is indeed much lower than the SEU cross-section (due to the much smaller affected physical area), making them far less common than bit upsets.

A single event transient is much like a single event upset or fault interrupt in the sense that it also results from a voltage spike induced by incident charged particles. However, for single event transients, such an upset occurs on a flip-flop register, causing a momentary voltage spike in the flip-flop output which changes upon the change of flip-flop state, typically upon a clock cycle. Hence such upsets are “transients,” clearing with the change in the clock signal. In as much, such transients would only be detected in the output voltage of a flip-flop register - such upsets would not appear upon an

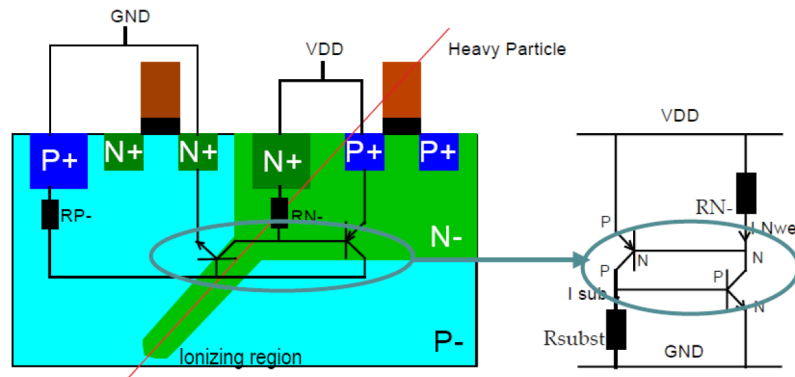


Figure 2.12 Example of a single event latchup condition [7].

investigation of the configuration logic. Thus detecting transients requires an experimental setup which would monitor the actual state of the outputs in realtime - something the proposed experiment did not do.

In the case of single event latchup, a heavy particle creates a low-impedance, high current path from VDD to VSS (Figure 2.12), resulting in possible permanent damage to the device itself if current is not limited [7]. Unlike SEFIs and SEUs, a latchup condition requires a complete power cycle of the device to restore normal operation[5, 21].

Fortunately, the epitaxial substrate layer on Virtex devices renders them immune to latchup up to LET values of $120 \frac{\text{MeV}\cdot\text{cm}^2}{\text{mg}}$ [7], well beyond the value that any single ionized light particle could deposit.

2.2.5 Long-term effects of radiation damage

Single event upsets are not the only type of damage incurred by exposure to radiation, despite being the most prevalent. Rather, the same nuclear interactions with the Silicon lattice which produce heavy particle fragments (and thus, upsets) also introduce deep-level defect states into the lattice. These “trap states” act as effective recombination centers inside the semiconductor bands by “trapping” majority carriers (in the case of Silicon, electrons) which would normally be promoted from the valence to conduction band in the newly formed mid-gap states, where they then recombine with minority carriers and annihilate [22].

Further complicating matters, these trap states must be filled entirely before carriers can be promoted to the conduction band (as illustrated by Figure 2.13), leading to the rise of a “leakage current,” where voltage applied does not correspond to promoted carriers and ultimately, switching current [23]. Hence, as defect states accumulate within the Silicon lattice, the performance of a device in terms of

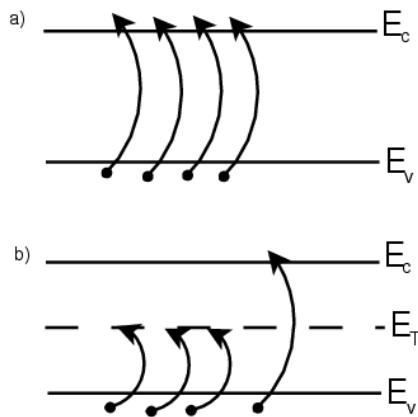


Figure 2.13 Simplified energy-band diagram of a semiconductor. a) Before radiation damage, carriers are directly promoted across the band gap from the valence band to the conduction band, b) After exposure to ionizing radiation, defects in the lattice give rise to “trap states” in the mid-gap region which must be filled entirely before carriers can be promoted to the conduction band.

response time and leakage current begins to degrade with increasing radiation dose.

Xilinx’s radiation-hardened Q-Pro line of Virtex II devices have been tested up to doses of 1.2 MRad, with the following observed effects [24]:

- At a TID of 300 kRad, the device no longer meets all timing specifications. While the device will still continue to operate properly, it may not be able to handle higher clock speeds (on the order of 250 MHz or more).
- At a TID of 400 kRad, the SEU cross-section of the device starts to noticeably rise.
- At a TID of 800 kRad, the ICC leakage current begins to increase.
- At a TID of 1.2 MRad, the ICC leakage current is now double the manufacturer’s nominal specified value.

As I will demonstrate later on in this paper, long-term effects of radiation will not be a concern in the tested configurations within the PHENIX environment, as to accumulate even the lowest level of TID for defects to become noticeable would take several operating runs.

2.3 Mitigating radiation-induced upsets

In this section, I will give an overview of common methods for mitigating the effects of static upsets in SRAM devices, including triple module redundancy with voting, partial reconfiguration, and finally fabrication techniques which can increase SEU resistance.

2.3.1 Triple module redundancy with voting

One of the most common techniques for mitigating the effects of static single event upsets is to triplicate the logic components for any given decision within a device, with the truth table value being determined by the majority vote of the three outputs. The advantage of such an approach is that it would require concurrent upsets in two cells on the same module in order to cause an upset in data output - a scenario of much lower probability, especially when coupled with other mitigation techniques [15].

The disadvantage of this approach is obvious - triplicating every module within an SRAM device is incredibly expensive in terms of logic (requiring three times the amount of logic utilization) as well as being potentially time-consuming to implement, particularly for more complex designs. While Xilinx has produced a software utility known as TMRTool which can handle the latter problem⁵, unfortunately this is not always the most feasible solution for designs which utilize a large portion of available device logic.

Likewise, it should also be noted that the voting logic itself would remain susceptible to upsets as well with traditional TMR (Xilinx's TMRTool is designed to ameliorate this problem, however). Given these challenges, the need for supplemental means of SEU mitigation becomes apparent.

2.3.2 Eliminating half-latch vulnerabilities

Another point of vulnerability is in a circuit component known as a "half-latch," frequently used in Virtex FPGA designs to simulate constant logical "0" or "1" values. Half-latches are most especially useful for cases in which a device input is left unconnected - for example, a clock enable on a flip-flop register. In this case, a half-latch is a useful way for the configuration bitstream (the instruction set downloaded into the chip) to generate a constant logic value without relying on unnecessary data structures like constant LUTs in order to generate such values [8].

The problem with half-latches, however, is in their susceptibility to inversion via upsets, whereupon an incident charged particle can induce a voltage spike and invert the value stored in the half-latch,

⁵See <http://www.xilinx.com/products/milaero/tmr/index.htm> for more information in Xilinx's TMRTool.

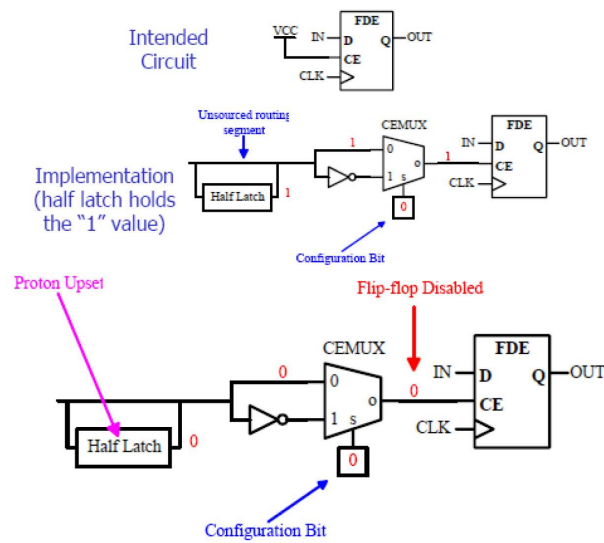


Figure 2.14 Top: Illustration of intended constant “1” value (V_{cc}) and its half-latch implementation. Bottom: Example of half-latch vulnerability to a proton-induced upset [8].

causing improper operation (Figure 2.14). Unlike static SEUs in configuration bits however, half-latch SEUs do not show up directly in the configuration bitstream, but rather in the data output itself, making them a dynamic problem rather than a static one.

One can solve this vulnerability by eliminating half-latches altogether from critical device inputs (for example, device structures like GCLK and others), although this proves to be no trivial task. Such a process can be accomplished by several means, including obtaining constant logic values from externally driven input pins, constant LUTs, or flip-flops as shown in Figure 2.14 .

The key point which should be emphasized is that whatever choice of explicitly logical inputs are used, these should be resources which can be programmed directly by the configuration bitstream. This means that when a constant logic source is upset, it can be detected and corrected using the same methods used to correct other static upsets in the configuration bitstream logic [8].

Such a removal process can be carried out through careful design at the HDL level, however it is noted that this will not guarantee removal of half-latch vulnerabilities, as different design tools and chip technologies may end up with the circuits being re-incorporated into the design at lower levels of device abstraction. If this were the case, half-latch vulnerabilities would not be a problem at all, as they could simply be rooted out in the highest abstraction levels of design. Rather, to ensure half-latch vulnerabilities are removed may require directly editing the FPGA design at the physical database level

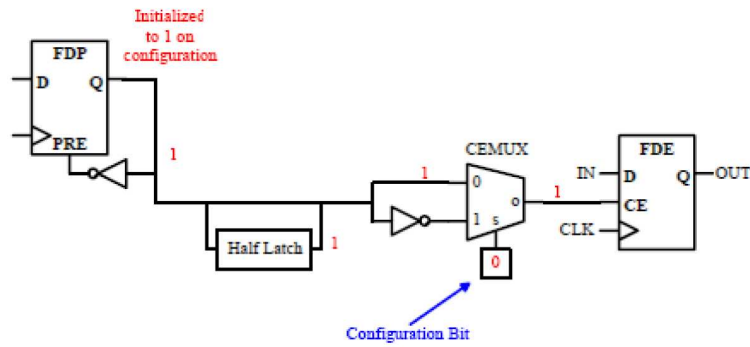


Figure 2.15 SEU-resistant alternative to the half-latch reliant design shown in Figure 2.14. The constant value for clock enable (CE) is now driven by a separate flip-flop (PRE asynchronously set to “1”) which can self-correct when upset [8].

(i.e., the .ncd and .xdl files used to create the .bit bitstream file) [8].

This method comes with the drawback of requiring a more intimate knowledge of the device structures themselves in order to make the correct modifications. One strategy devised in this case was to create an automated utility for an FPGA editor which would take one FPGA input pin (tied high) and use this signal (inverted as inputs demand) to replace the reliance upon half-latches for constant logical values. Whether this utility is currently available directly in commercial FPGA editing packages is unknown, however future tools like this may eventually make eliminating half-latch vulnerabilities as more trivial affair [8].

2.3.3 SEU detection and repair with partial reconfiguration

One can detect errors in a device’s configuration by comparing the configuration data bits as programmed into the device to the original configuration bitstream downloaded into the device as a reference . In the event that the two do not match, a user can initiate a reconfiguration of the device. It was through this process in fact that made it possible check the device under test in this experiment with the FIVIT software provided by Xilinx .

To create a device which has a high degree of reliability from errors induced by SEUs, this process can be automated at the design level itself. By implementing an algorithm in a dedicated readback and configuration device to check the configuration bitstream, a device can continuously check itself for upsets and initiate a reconfiguration when necessary. An application of this technique being developed by Xilinx at Los Alamos National Laboratory for a low earth orbit satellite (with an expected upset

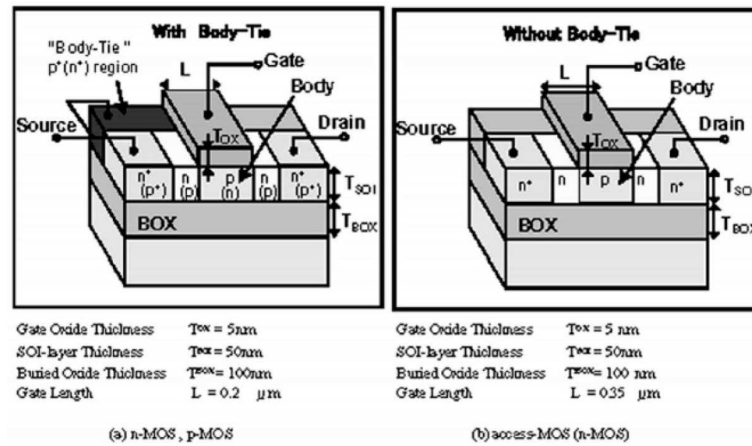


Figure 2.16 Example schematic of body ties on an SOI-MOS transistor [9].

rate of one upset across three devices per hour) shows a reliable uptime rate (no SEUs or SEFIs) of approximately 99.9989%, assuming a reconfiguration time of 20 ms [15].

One of the drawbacks of a device reconfiguration is that to do such requires taking the device offline - destroying the state and with it, any stored data. Yet by isolating the affected frame(s) and reconfiguring these directly, the required reconfiguration time can be taken down to as low as 3 μs if only a single frame requires reconfiguration. Meanwhile, such a method does not require taking the entire device offline - especially advantageous for an application such as the detector environment, where taking the device offline means losing valuable physics data [15].⁶

2.3.4 SEU resistance from transistor body ties

An entirely different approach to mitigating static upsets within a device is to direct any radiation-induced currents away from the sensitive areas of the device (Figure 2.16).

This can be accomplished by using feedback resistors and capacitors upon the sensitive areas of an SRAM logic circuit (Figure 2.17) [9]. (For reference, one may want to refer back to Figure 2.2 for an example of the unmodified circuit with sensitive areas highlighted).

This method is not only inexpensive to implement (requiring minimal changes to the fabrication process), but also highly successful at lowering the SEU cross-section profile (Figure 2.18) by shifting the activation LET and increasing the width of the Weibull curve. While the saturation value remains nearly unchanged, the upward shift in the LET threshold from $45 \frac{\text{MeV}\cdot\text{cm}^2}{\text{mg}}$ to $164.4 \frac{\text{MeV}\cdot\text{cm}^2}{\text{mg}}$ [9] is significant enough to provide highly useful hardening against static upset effects.

⁶For additional information on partial device reconfiguration, see Xilinx Application Note XAPP216, "Correcting Single-Event Upsets Through Virtex Partial Configuration."

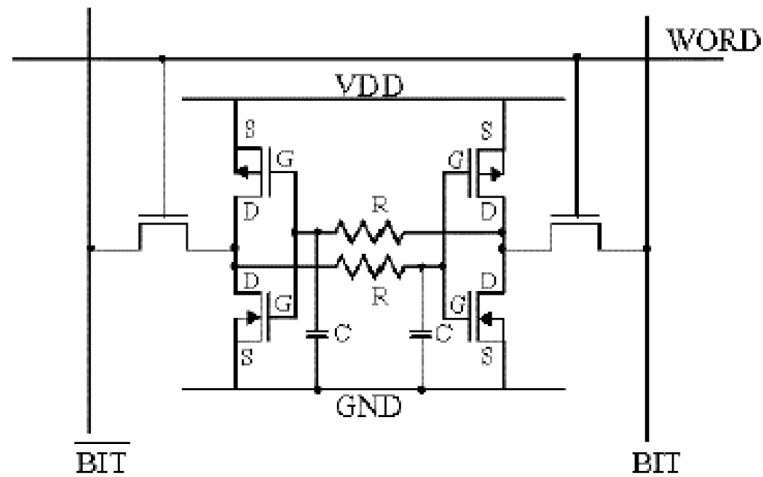


Figure 2.17 Diagram of an SRAM circuit with feedback resistors R and capacitors C added to draw off radiation-induced currents. Gates are denoted as G , sources as S , and drains as D [9]. This strategy is similar to the design employed by Actel’s internal charge pump design [10], which is designed to drain off radiation-induced leakage currents.

As an aside, it appears that this strategy of shunting off the induced leakage current is what is employed by Actel’s RTSX-S rad-hard FPGA series through the use of its internal charge pump, which has shown to effectively drain off leakage currents for a total integrated dose up to 60 kRad [10], however there is no indication this process is used in Xilinx’s rad-hard offerings.

2.4 Summary

In this section, I have presented an overview of the relevant background and motivation for pursuing this experiment. This has included a presentation of the advantages of radiation tolerant FPGA designs for on-detector electronics as well as the challenges involved in implementing such designs, primarily in terms of radiation-induced upsets within SRAM-based devices. Likewise, an overview of the physical causes of upsets in key components of Xilinx’s Virtex series architecture has been presented as well several means for mitigating such errors. These design techniques include triplicating logical decisions within the design and using majority voting to obtain the logical outputs; eliminating half-latch vulnerabilities within designs by routing constant values from alternative sources such as external logic pins or constant configuration bitstream logic sources which can be detected and corrected when upset; detecting and repairing upsets in configuration logic through detection of upsets by comparison to the

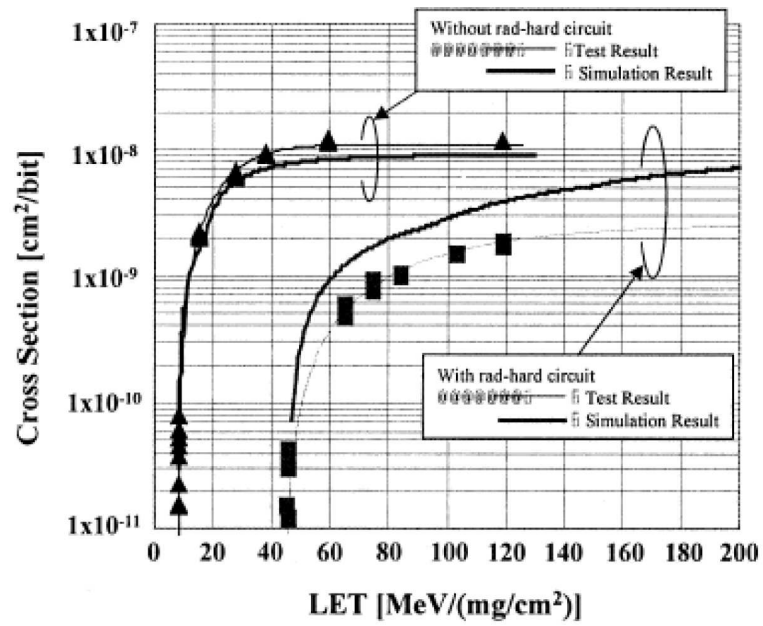


Figure 2.18 Cross-section curves for SRAM device with and without body tie circuit [9].

downloaded configuration bitstream and repairing only the affected logic; and finally, through the use of transistor body ties to drain off voltage spikes induced by charged particles.

3 EXPERIMENTAL BACKGROUND AND SETUP

3.1 Introduction

Despite the vast amount of information found on both the effects of radiation on such devices, most field tests of said devices had been conducted using cases of a beam with known fluence, unlike the case of the PHENIX IR, where the actual radiation dose as a function of position and particle type is much more complicated. Thus, the motivation for this experiment became that of finding a means making a tractable model on a device within the PHENIX IR and using such a model to evaluate the suitability of rad-hard FPGA devices for on-detector electronics.

When a simple Monte Carlo model¹ was used to predict radiation dosages and corresponding SEU rates of a hypothetical device within the IR and the results proved encouraging, this motivated further tests of the accuracy of the proposed model and ultimately the feasibility of rad-hard devices within the IR by placing an actual device within the environment and observing the total integrated dose (TID) and the SEU frequency.

The goal of this section shall therefore be to outline the hardware and software setup designed to collect this experimental data (which shall also be presented in this chapter).

3.2 Device under test

For this test, a prototype version of a Xilinx radiation-hardened FPGA (model XQR2V6000) was used with a Virtex II 1152 proto board, encased in an Aluminum enclosure. A standard JTAG interface was connected to a 100-foot parallel cable, which allowed for the testing equipment itself to remain outside of the IR in the experimental assembly hall. To ensure proper device communication, the individual JTAG headers were soldered directly to the corresponding pins upon the proto board.

The self-contained box was attached to a frame for a separate prototype GEM detector (Figure 3.1) which was placed upon the MVD lifting table on March 3, 2004 at the “far” position of approximately

¹See Appendix B for a more detailed discussion of the simple Monte Carlo model used for the preliminary calculations.

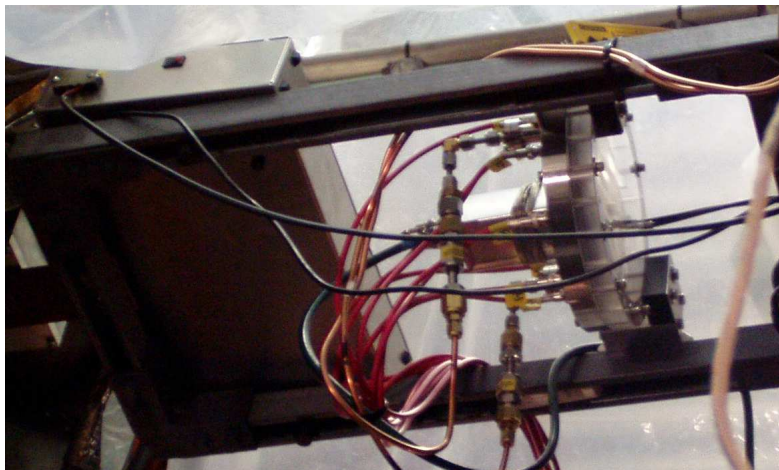


Figure 3.1 Picture of the test box setup (left) attached to the frame of the GEM detector (right) in the PHENIX IR.

250 cm below the beam collision point and raised up into the near position (approximately 53 cm below the collision point) from March 17th to March 19th, after which it was lowered back into its original far position.

Data collection began on March 5th when development on the data acquisition software stabilized and ended on March 24th with the end of 200 GeV running at RHIC.

3.3 Data Acquisition and Monitoring

3.3.1 FIVIT software and SEU measurement

To check for SEUs, Xilinx also provided us with their FIVIT (Fault Inject and Verification Tool) software. This software is capable of checking a programmable logic device for SEUs by comparing the current logic configuration with a mask file containing the chip configuration, in essence checking each individual configuration bit in the downloaded design to ensure the correct state for each.

The FIVIT software (Figure 3.2) is also capable of determining whether an upset occurs in the block RAM (BRAM) or the configurable logic blocks (CLB) the configuration logic of the chip, both of which are measured in terms of the used blocks only, which is not the same as the actual configuration and block ram capacity of the chip itself.

Throughout the experiment, only errors in the configurable logic blocks were observed, namely due to the fact that little design logic was stored in the block ram sections.

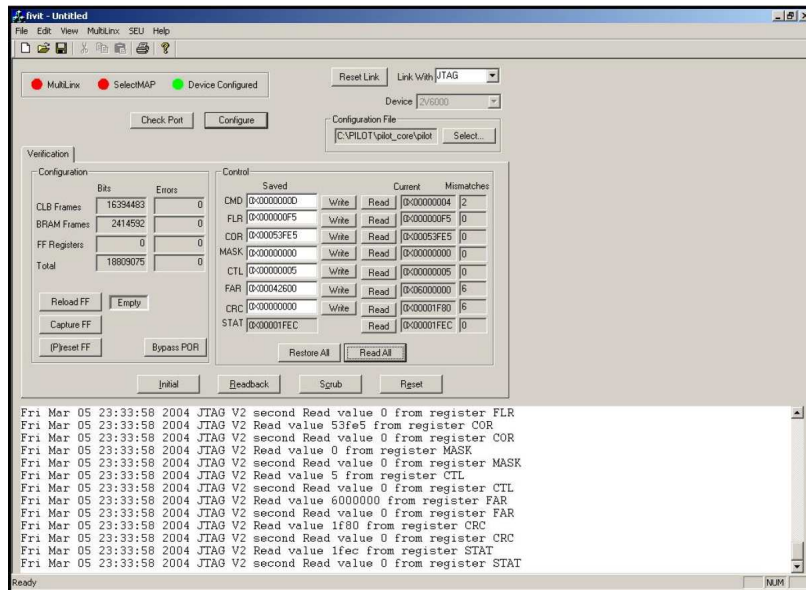


Figure 3.2 Screen shot of FIVIT software (Xilinx).

3.3.2 Data acquisition procedure

Data collection itself was done on a PC setup in the assembly hall, connected to the board via a 100-foot parallel cable and a standard JTAG interface whose connections were directly soldered to the appropriate pins on the proto board to ensure reliable communication with the device.

Every 2 minutes, the ZDC rate in the PHENIX IR was polled from the RHIC experimenter status page (which gives the ZDCLL1 rate) using a Perl script which recorded the result into a log file. The integrated luminosity was taken as the sum of the prior integrated luminosity and current ZDC rate multiplied by the time elapsed between measurements. The units of integrated luminosity are thus collisions, as the ZDC rate is in collisions per second, and the integrated luminosity is the measured ZDC rate multiplied by time.

Every 20 minutes, the chip configuration was checked by FIVIT using an AutoIt automation script [25] to handle GUI operations in conjunction with a Perl script which extracted results from the FIVIT log into a useful format. Confirmed upsets were distinguished from occasional, spurious JTAG communication errors by verifying that the errors were consistent upon a second and third readback. While SEUs were persistent errors upon multiple readbacks, cable communication errors could be distinguished by the fact that they were not. In addition, SEUs occurred in only a handful of bits at a time, whereas problems in both the power supply and JTAG communication resulted in errors which were several orders of magnitude greater than SEU events.

Upsets themselves were correlated to the closest measured integrated luminosity count in order to give a proper account of the time interval that could be expected between upsets. After a confirmed SEU event, the chip was reconfigured via FIVIT and the integrated luminosity count in the log reset.

3.3.3 Online monitoring and analysis

After each readback of the chip (irrespective of whether an SEU was observed), all of the results were parsed and presented in HTML format in addition to being run through a ROOT analysis macro [26], which output histograms of the integrated luminosity over both the last day and week as well as the SEU events in the configuration logic, the block RAM, and the total number of SEUs, all as a function of integrated luminosity.

These results were uploaded to a web server back at Iowa State so that progress (as well as any problems) could be monitored in realtime.

3.4 Dosimetry measurements

3.4.1 Introduction

Two TLD dosimetry badges were attached to the outside of the Aluminum frame over the course of running. The first was attached when the board was first put into the IR with the MVD lifting table in the low position and which was then exchanged on March 17th for a second badge. This second badge was attached to the board when the MVD table was raised into the high position near the beam and then remained on the board after the MVD lifting table was lowered once more on March 19th and remained on the board until the end of all Au+Au running for RHIC Run 4, whereupon the entire setup was removed from the IR.

3.4.2 Dose as measured by TLD badge

Table 3.1 gives the reported results from the TLD badge as they were received from BNL personnel monitoring, presented in the human-equivalent rem dose. Five categories of doses were measured, corresponding to the three tissue depths defined above (“shallow”, “lens”, and “deep”), and two neutron doses, one from LiF chip upon the badge itself (measuring “slow” neutrons with a kinetic energy less than 0.5 MeV) and a CR39 film for “fast” neutrons (of energy greater than 0.5 MeV) [27].

To evaluate these doses in terms of energy absorbed rather than the human-equivalent dose (i.e., radiation absorbed dose or rad), said measurements need to be re-scaled by the quality factors used

Table 3.1 Measured results from TLD badges in human-equivalent rem dose.

Position	Shallow	Lens	Deep	Slow Neut.	Fast Neut.	Int. Luminosity
250 cm	0.118	0.108	0.163	0.109	0.570	2,087,128,441
53 cm + 250 cm	0.347	0.354	0.112	0.330	1.114	1,228,730,933
53 cm (est.)	0.290	0.302	0.277	0.0328	0.863	214,306,673

Table 3.2 Corrected TLD results in rem/event.

Position	Shallow	Lens	Deep	Slow Neut.	Fast Neut.
250 cm	5.65E-11	5.17E-11	7.81E-11	5.22E-11	2.73E-10
53 cm (est.)	1.35E-09	1.41E-09	1.53E-10	1.29E-09	4.03E-09

in originally calculating the rem doses. From the U.S. Code of Federal Regulations (10CFR20 and 10CFR835), the accepted quality factors of 1 for gammas (“deep” dose), 2 for “slow” neutrons, an 14 for “fast” neutrons [11]. These are of course aggregate quality factors - the quality factor itself still varies as a function of energy (see, for example, Figure 4.6). As an additional complication, to convert the dose of the BNL-specific chip for slow neutrons into mrem, the generic value in thermoluminescent units is multiplied by a factor of approximately 11 (however, this factor will vary with the specific badge calibration) [27].

Given the fact that the conversion proves to be inexact at best, particularly for the energy-dependent neutron quality factors, the calculated doses in the PISA model were made in the human-equivalent rem dose. Hence, the quality of the PISA model shall be evaluated by comparing the measured dose from the TLD badges (Table 3.1), converted into a per-event rem dose (Table 3.2) to a per-event human dose rate as calculated by PISA.

3.5 Observed SEU rate as a function of integrated luminosity

Tables 3.3 and 3.4 give a chronological summary of bit upsets for both positions of the test device in the far (≈ 250 cm below collision vertex) and near (≈ 53 cm below collision vertex) positions, respectively. These tables are also graphed as Figures 3.3 and 3.4.

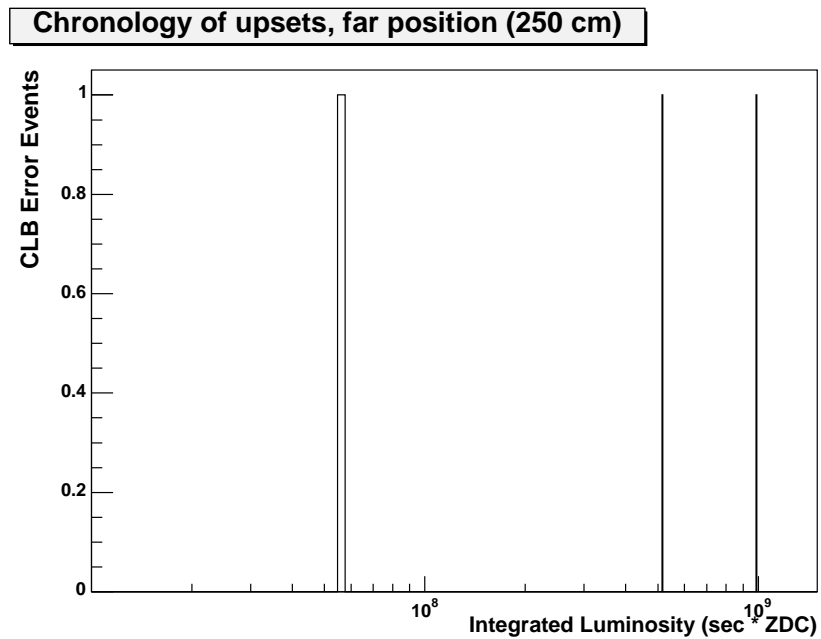
What one may immediately notice is that the rate of upsets does not scale as a factor of $\frac{1}{r^2}$, as one would intuitively expect flux to scale. However, this is only the case for an isotropic flux distribution. In this case, the bias around zero-rapidity for particle production breaks this scaling requirement, as flux is concentrated near the perpendicular axis to the collision point, thus allowing for many particles which would pass through both the near and far positions of the chip.

Table 3.3 Chronological Summary of SEUs ($r = 250$ cm).

Integrated Luminosity (counts)	CLB Bits	CLB Err	BRAM Bits	BRAM Err
987289774.33	16394483	1	2414592	0
57476342.26	16394483	2	2414592	0
515565649.96	16394483	1	2414592	0

Table 3.4 Chronological Summary of SEUs ($r = 53$ cm).

Integrated Luminosity (counts)	CLB Bits	CLB Err	BRAM Bits	BRAM Err
48579547.17	16394483	1	2414592	0
73473562.21	16394483	1	2414592	0
36534846.13	16394483	1	2414592	0

Figure 3.3 Observed upsets as a function of integrated luminosity, ($r = 250$ cm)

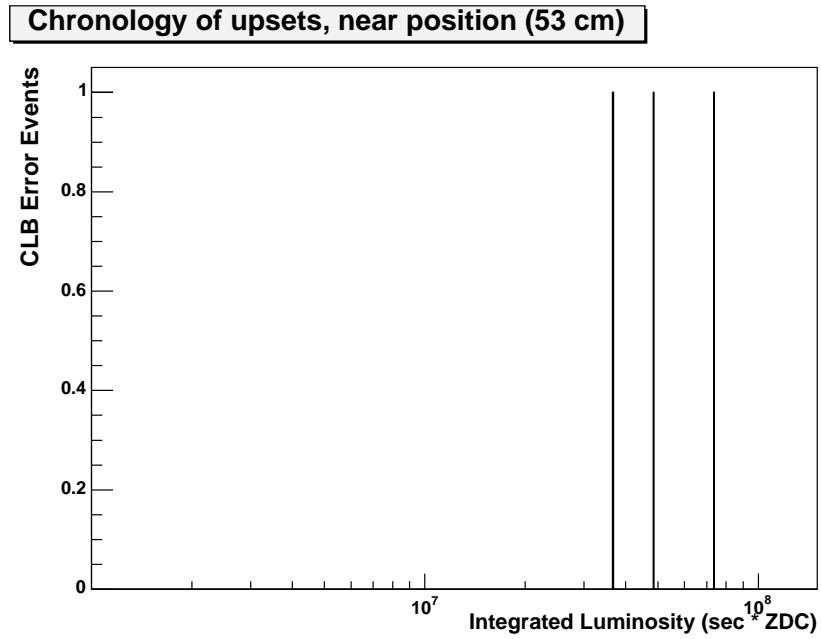


Figure 3.4 Observed upsets as a function of integrated luminosity, ($r = 53$ cm)

3.6 Summary

In this section, I have presented an overview of the experimental setup and procedure used to obtain SEU data for an Xilinx rad-tolerant XC2V6000 FPGA. To this end, I have provided specific information as to the hardware used in this test, the conditions the devices was conducted under, and in particular the data acquisition procedure, including the conditions which under which single event upsets were classified and measured.

4 DETAILED EVALUATION OF THE PISA MODEL CALCULATIONS

In this section I shall present an overview of the PISA model used to construct a general model of the radiation environment within PHENIX for the purposes of estimating the SEU rate of a given device as a function of position. In particular I shall present the assumptions made in constructing such a model, the specific geometry used in this simulation, and correction factors introduced in the PISA model to compensate for the nature of the experimental setup.

This model shall then be evaluated by directly comparing the predicted doses for gammas and neutrons to those observed by the attached TLD badges. In addition, the data produced by such a model to make SEU rate predictions shall be analyzed by examining the predicted particle fluences predicted, in terms of both raw fluences as well as momentum spectra for selected types (which are tabulated into the SEU cross-section). Particular attention shall be given to remarkable aspects of these particle distributions, for example, particle origins within the IR, which shall play a key role in determining the constraints upon any analytical model seeking to model the radiation load upon a given device in the IR.

4.1 Overview of PISA model

In this section I shall present a full account of the PISA model used to create an analytical model of upsets for the device under test inside the PHENIX IR. In particular, I shall give a detailed overview of the PISA environment itself, the geometry used for the test, the method by which the doses were calculated, and finally the assumptions and calculations made to produce an SEU rate estimate.

4.1.1 Introduction to PISA

The PISA software package is a custom interface to the popular GEANT particle simulation software, a package generally regarded as a standard for purposes of detector simulations. The PISA interface was designed specifically for use with the PHENIX collaboration to simulate detector behavior, having several standard PHENIX detector components designed for simulation in the GEANT tracking

engine, in addition to providing a standard interface to simulate detector response of planned upgrades such as the Silicon Vertex Detector. Users can choose what detectors to “activate” in the IR and select among physical effects to model - for example Cherenkov radiation, Bremsstrahlung, etc., in addition to specifying “sensitivity” of detectors to particular particle types, such as neutral hadrons. In addition, tracking energies can be modified in the various detector media to balance simulation performance with resource consumption, ultimately providing a highly flexible interface which can be used to “fine-tune” detector responses.

Users can select from several event-generation interfaces, from single particle events generated by the user themselves to more sophisticated packages such as HIJING, the event generator used for purposes of this simulation. The HIJING package allows for a completely customizable simulation of nuclear collisions; users can control the atomic mass (A), the atomic number (Z), the RMS values of the collision vertex, and the laboratory momentum, as well as the collision centrality. For purposes of this simulation, the HIJING event generator was configured as to simulate the experimental conditions as closely as possible, with an RMS value of the z-vertex set at 22.0 cm, laboratory momentum $\sqrt{s} = 200$ GeV, with minimum-bias collisions of Au+Au nuclei.

Simulations were conducted on a cluster of 18 HP Tablet PCs, with individual “batches” of 500 events taking approximately 45-55 hours per batch to complete, for a total of approximately 70,000 simulated events.

4.1.2 Assumptions used in PISA model

Chief among the assumptions made within the PISA model is that of radial symmetry in the particle yield distribution about the collision axis in both the experiment and the HIJING event generator. This assumption was ultimately exploited in the geometry used with HIJING event generator for purposes of statistics generation. Additionally, the assumption was made that the particle flux as a function of rapidity changed negligibly in the small area about the interaction point (i.e., $z = 0$ cm). This again was used for statistics purposes in order to widen the exposed sample area, hence increasing the pool of events to study.

Finally, the SEU cross-section of individual particles was taken under the assumptions that the SEU cross-section scaled in proportion to the ratio of the particle’s inelastic scattering cross-section to that of a proton of the same kinetic energy. Thus using cross-section data obtained from [28], the SEU cross-section was calculated for protons from the Weibull curve, then scaled by the ratio of inelastic cross-sections to produce a scaled cross-section contribution.

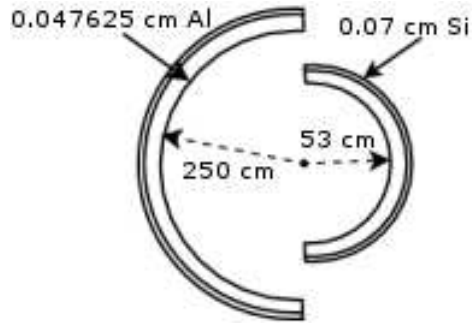


Figure 4.1 Diagram of PISA geometry used for purposes of simulation (not drawn to scale).

The reasoning for this comes from the assumption that the Weibull curve is in fact a convolution of two other functions - the nuclear interaction cross-section of the particle with the Silicon, and then an unspecified “geometric” scaling factor which is the probability of an ionization (and resulting voltage spike) occurring within a “sensitive” region of the device, (as described in [3]), giving the following formula (Equation 4.1) for the integrated cross-section:

$$\sigma_{SEU} = \int F_{geom}(E) \cdot \sigma_{interact}(E) \cdot dE \quad (4.1)$$

This can be rewritten in differential form (Equation 4.2) to give a differential cross-section as a function of energy, i.e.:

$$\frac{\sigma_{SEU}}{dE} = F_{geom}(E) \cdot \sigma_{interact}(E) \quad (4.2)$$

This assumption shall be explored in greater detail in the sections to follow.

4.1.3 Simulation details

Using PHENIX’s PISA software, an analytical model was constructed to simulate the dosage experienced by the Silicon die of the device under test in the PHENIX IR. To simulate the die, two half-annular regions with radii $r = 53$ cm and $r = 250$ cm were inserted into the Silicon Vertex Detector (SVX) geometry. These two annuli were oriented opposite one another, such to prevent “screening” of particles by the inner layer which would otherwise reach the outer layer. For input, PISA’s GEANT interface used over 70,000 minimum-bias Au+Au HIJING events with $\sqrt{s} = 200$ GeV.

Figure 4.1 gives an illustration of the PISA geometry used for the simulation.

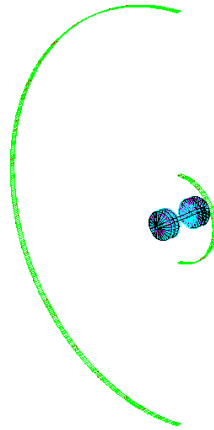


Figure 4.2 GEANT rendering of sample geometry used for simulations (drawn to scale).

Each annuli had a thickness of .07 cm (corresponding to the thickness of the Silicon die of the Xilinx FPGA) and a width of 6.6 cm (three times the ordinary die width, used for greater statistics). Finally, each layer was shielded by a 0.47625 cm passive layer of Aluminum, which served to simulate the screening effects of the heatsink (measured to be 0.3175 cm thick) as well as the device packaging and aluminum enclosure (composing the other 0.15875 cm).

The choice of using an annular region of Silicon was namely for statistics purposes - for the purposes of the simulation, it was assumed that the collision products exhibited radial symmetry about the longitudinal (z) axis. Thus, to obtain the actual absorbed dosages and SEU rates, the calculated values were scaled by the ratio of the chip area to the area of the annular region.

Figure 4.2 shows a GEANT rendering of the custom SVX geometry used for the simulations.

4.2 Calculation of absorbed dosages

To verify the “sanity” of the PISA model and its applicability to the real detector environment, doses from γ particles and neutrons shall be calculated from the particle fluxes using known techniques to calculate human-equivalent doses. These calculations will then be compared to the equivalent doses as measured by the attached dosimetry badges to characterize the quality of the PISA model in simulating the conditions actually experienced by the device in the detector environment.

In this section, I shall present the method in which the absorbed dosages were calculated. In particular, the dosages were calculated as to emulate the performance of the attached dosimetry badges, which are designed to measure the human-equivalent dose at various tissue depths. Hence, the dosage

calculations presented in this section shall seek to simulate these human-equivalent doses. These dose predictions will be compared to the measured doses as a means of evaluating the accuracy of the PISA model itself, and thus the applicability of its predictions regarding the SEU rate.

4.2.1 Use of dosimetry badges in the experiment

Over the course of the experiment, two dosimetry badges were used to measure the ionizing radiation dose the chip was exposed to over the course of running. The first badge was attached to the board while the setup remained in the far position and was removed prior to the board being elevated to the near position. The second badge was attached to the board when it was raised into the near position, however it not able to be removed from the board prior to the end of the run due to the lack of access to the beam during such time. However, as the predicted dose close to the beam was an order of magnitude greater than the far position and the luminosity of the 64 GeV run was order of magnitude lower than that of the 200 GeV run, the dose from the board's exposure in the near position to the beam can be corrected analytically using the dosage measured from the first badge.

Given that the integrated luminosity of the “near” dose was known, the dose from the badge's exposure in the far position can be subtracted off from the estimated dose rate of the first badge, thus giving an estimated dose in the “near” position.

4.2.2 Overview of key concepts in radiation dosimetry

One of the fundamental concepts in radiation dosimetry is the difference between a radiation absorbed dose (in units of rad or Gray) and a human-equivalent dose (measured in rem or Sievert), which is a measure of the energy absorbed by tissue multiplied by a specific “quality” factor which measures the relative damage received by a particular type of tissue at a given particle energy. Given that the primary purpose of the dosimetry badges used for measuring the dose upon the device are to measure doses in humans, the doses obtained from the badges were given in human-equivalent rem form.

Thus, as the quality factor (defined by federal radiation protection standards) for particles such as neutrons will vary as a function of energy, trying to convert an absorbed energy dose into a human-equivalent dose proves to be an inexact method at best. Hence the doses calculated in the model will use a human-equivalent form for neutron sources, which can be obtained directly through dose-equivalent fluence rates defined by the federal government [11]. (By contrast, the federally defined quality factor for γ radiation is defined simply as unity, thus the conversion from energy-absorbed dose to the human-equivalent dose is a trivial one.)

The dose absorbed in the material from photons relies exclusively from the energy imparted by photons into electrons, minus energy carried away by processes such as Bremsstrahlung radiation (i.e., “braking” radiation, the energy carried away by a photon when an electron decelerates). Thus as photons transfer some or all of their energy into electrons (via Compton scattering and photoelectric absorption, respectively), the scattered electrons leave ionizing tracks inside the material, and thus an ionizing radiation dose [1].

4.2.3 Dose from γ radiation

The purpose of the following sections shall be to demonstrate the method used for calculating the human-equivalent dose from photon (γ) sources. Specific attention shall be given to the physical of the dose formula and the calculation of the human-equivalent photon dose for various tissue depths.

4.2.3.1 General formula for γ dose

The calculation of radiation dose from photons is a two-step process - first, in determining the kinetic energy lost by the photon to the material (known as *kerma* - **k**inetic **e**nergy **r**elaxed in **m**aterial), and then in calculating the amount of energy actually *absorbed* by the material (i.e., the dose).

Thus the formula for kerma in a medium is as follows [1]:

$$K_{med} = \phi \cdot \left(\frac{\mu_{tr}}{\rho} \right)_{med} \cdot E_{tr} \cdot 1.6022 \cdot 10^{-8} \frac{\text{rad}}{\text{MeV}} \quad (4.3)$$

Where ϕ is the photon flux, $\frac{\mu_{tr}}{\rho}$ is the mass-energy transfer coefficient (which varies as a function of incident photon energy) for the medium, and E_{tr} is the photon energy transferred into the medium (which should not be confused with E_{ab} , the energy *absorbed* by the medium).

The actual “dose” imparted into a material is then a function of the fraction of energy which is absorbed into the material itself (rather than being carried away). This is calculated through a *mass energy absorption coefficient* μ_{en} , which is related to the mass-energy transfer coefficient by unitless $(1 - g)$ factor in the following fashion [1]:

$$\left(\frac{\mu_{tr}}{\rho} \right) = \frac{\left(\frac{\mu_{en}}{\rho} \right)}{(1 - g)} \quad (4.4)$$

The $(1-g)$ factor is known for specific photon energies, whose values are given in Table 4.1.

Hence, the absorbed dose (in rad) is:

Table 4.1 $(1 - g)$ values for photon absorption from [1].

Energy (MeV)	$(1 - g)$
0.662	0.9984
1.25	0.9968
1.5	0.996
2.0	0.995
3.0	0.991
5.0	.984
10.0	.964

$$D_{med} = \phi \cdot \left(\frac{\mu_{en}}{\rho} \right)_{med} \cdot \frac{E_{ab}}{(1 - g)} \cdot 1.6022 \cdot 10^{-8} \frac{\text{rad}}{\text{MeV}} \quad (4.5)$$

Thus the relationship between the absorbed dose and kerma becomes simply a matter of the scaling factor $(1 - g)$, i.e.:

$$D_{med} = K_{med} \cdot (1 - g) = \phi \cdot \left(\frac{\mu_{en}}{\rho} \right)_{med} \cdot E_{ab} \cdot 1.6022 \cdot 10^{-8} \frac{\text{rad}}{\text{MeV}} \quad (4.6)$$

4.2.3.2 γ dose at various tissue depths

Once the relationship between incident photon energy and dose within a material is established, it is a trivial matter to convert air kerma to a dose at various tissue depths, which is ultimately how doses are characterized by the TLD badge through a conversion factor C_k . Thus the dose at depth i is [1]:

$$D_i = C_{ki} \cdot K_{air} \quad (4.7)$$

This C_k factor, known as the “ambient dose equivalent” (also defined as the standard **H*(10)** by the International Commission on Radiological Units), is an energy-dependent scaling factor applied to the dose to obtain an equivalent dose at a “shallow” depth just underneath the dead layer of human skin (with a density length of $0.007 \frac{\text{g}}{\text{cm}}$), a “lens” depth (of the lens of the eye, a density length of $0.500 \frac{\text{g}}{\text{cm}}$), and a “deep” tissue dose (with a density length of $1.000 \frac{\text{g}}{\text{cm}}$).

The air kerma can be rewritten for this case to provide an easy means of calculating the dose:

$$K_{air} = \phi \cdot \left(\frac{\mu_{en}}{\rho} \right)_{med} \cdot \frac{E_{\gamma}}{(1 - g)} \cdot 1.6022 \cdot 10^{-8} \quad (4.8)$$

where the dose is given in rad and E_{γ} is the photon energy in MeV.

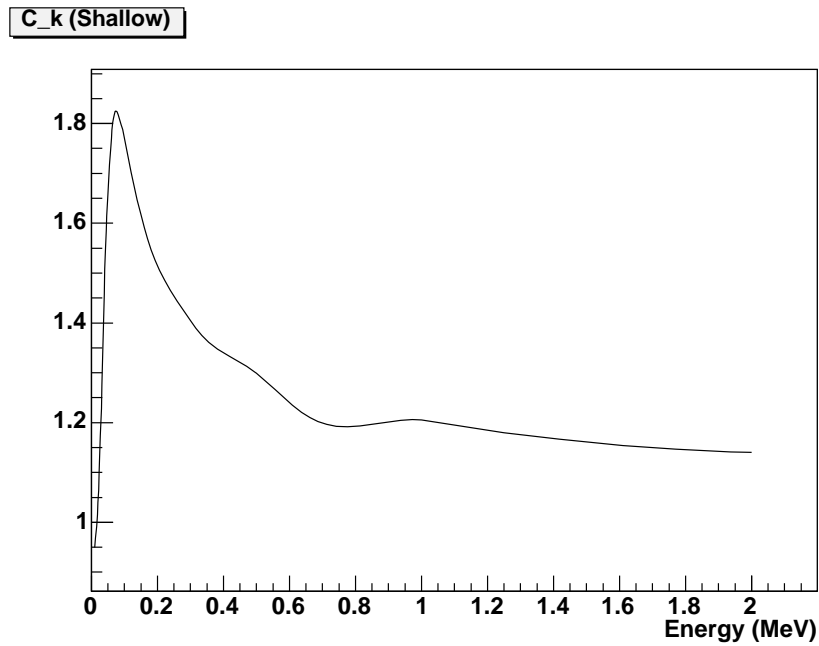


Figure 4.3 Graph of C_k fit used for purposes of calculating shallow-depth photon dose [1].

Taking fits to the energy-dependent values of C_k provided by [1], the equivalent dose at the three tissue depths was calculated from incident photons in PISA. Figures 4.3-4.5 give the C_k fits used for each of the depths (shallow, lens, and deep) calculated in the simulation.

Given a defined photon quality factor of unity [11], the dose conversion from an absorbed dose in rad to a human-equivalent dose in rem becomes trivial.

4.2.4 Dose from neutrons

While there exist several means of analytically calculating the neutron dose directly, these methods do not take into account the “quality factor” which converts a deposited-energy dose (rad) to a human-equivalent dose (rem). As the doses measured by the TLD were in a human-equivalent dose, it was deemed most appropriate to estimate the badge-equivalent dose in a similar fashion. In this manner, it proved much simpler to estimate the human-equivalent dose by the correspondence of dose and fluence, as defined by federal radiation protection standards [11].

Given neutrons of a particular energy, federal standards give an equivalent fluence rate required to produce a human dose of 1 rem per hour. By simply inverting this, one can obtain a fractional dose equivalent of neutrons at particular energies. Hence by fitting this inverted function as a function of

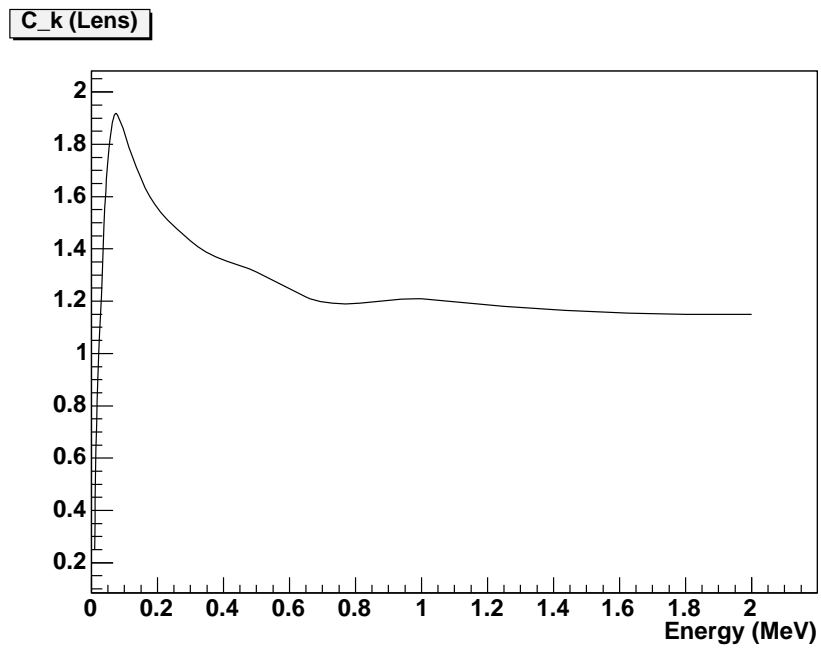


Figure 4.4 Graph of C_k fit used for purposes of calculating lens-depth photon dose [1].

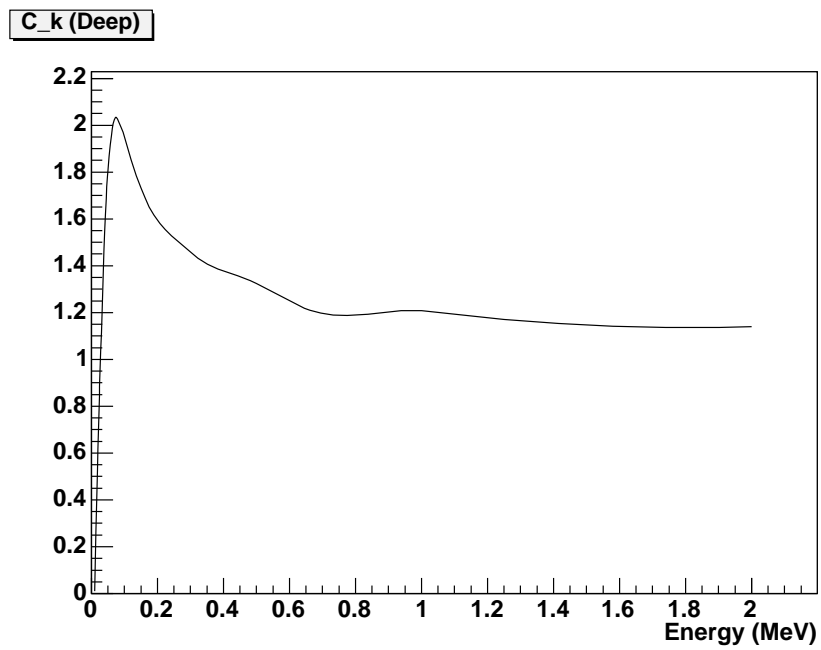


Figure 4.5 Graph of C_k fit used for purposes of calculating deep-depth photon dose [1].

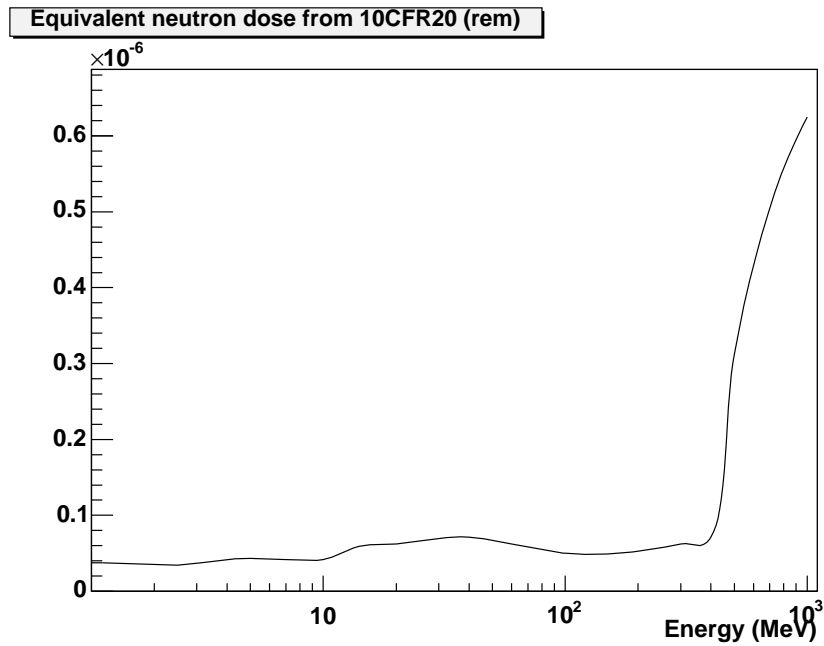


Figure 4.6 Graph of human-equivalent dose for neutrons (in rem) extracted from 10CFR835, as a function of neutron energy (in MeV) [11].

energy, the dose contributions of individual incident neutrons can be calculated, producing the fit shown in Figure 4.6.

4.2.5 Comparison of predicted doses to measured TLD values

In the following sections, I shall present the human-equivalent rem doses as calculated in the prior sections to the values as measured by the TLD badge attached to the test box in the IR, comparing these to the values predicted by the PISA model as a objective measure of the model's accuracy at simulating particle fluences.

4.2.5.1 Radiation doses as predicted by PISA

Tables 4.2 and 4.3 give a comparison of calculated dosages to measured dosages, in rem/event, broken down by the type of radiation source.

As previously noted, the doses calculated by PISA are in human-equivalent rem form, rescaled to a per-event dose rate.

Table 4.2 Comparison of measured human-equivalent radiation dose by TLD badges to dose calculated by PISA for $r = 53$ cm (rem/event).

	Shallow	Lens	Deep	Slow Neut.	Fast Neut.
Calculated	8.264E-10	8.185E-10	8.116E-10	2.682E-10	3.299E-09
Measured	1.35E-09	1.46E-09	1.29E-09	1.53E-10	4.03E-09
Offset (%)	-38.8	-43.9	-37.1	+75.3	-18.1

Table 4.3 Comparison of measured human-equivalent radiation dose by TLD badges to dose calculated by PISA for $r = 250$ cm (rem/event).

	Shallow	Lens	Deep	Slow Neut.	Fast Neut.
Calculated	4.110E-11	3.968E-11	3.894E-11	1.496E-11	2.787E-10
Measured	5.65E-11	5.17E-11	5.22E-11	7.81E-11	2.73E-10
Offset (%)	-27.3	-23.2	-25.4	-80.8	+2.09

4.2.5.2 Comparison of radiation doses as an evaluation of the PISA model

Clearly evident is the reasonable agreement between the PISA model’s dosage calculations and the measured dosages for the far ($r = 250$ cm) positions, where for all doses except for that of slow neutrons, the predicted dose is within $\approx 30\%$ the measured dose, with the predicted slow neutron dose still being within one order of magnitude of the measured dose. Doses for the “near” position prove to provide a more interesting challenge, given the fact that the dose is at best an estimate, given the fact that the second badge was also exposed to a measured amount of integrated luminosity in the far position at 200 GeV and then an unspecified integrated luminosity at 64 GeV. Hence the larger degree of underestimation for the near dose may largely be due to the uncertainty in the exact “dose” received while in the near position.

The case of slow neutrons presents a particularly difficult case for simulations, however. To properly estimate the dose of low-energy neutrons requires setting the tracking thresholds of detector components such as the magnet media down significantly, with the very real expense of computation time and stability to consider. While as a compromise the tracking threshold was set down to 50 keV, it is likely that at least some further accuracy may be recovered by lowering this threshold even lower, as well as lowering the tracking threshold in other media such as the Aluminum layer adjacent to the Silicon as well as that of the Beryllium beam pipe.

Nonetheless, as I shall show in the following section, the peak energy of neutrons created in the detector environment (in particular through interactions with the magnet media) is several orders of magnitude higher, indicating that to some degree the accuracy of the low-energy neutron limited no

matter what. Decreasing these tracking thresholds thus ultimately proves to be a matter of diminishing returns - while lowering the tracking thresholds may deliver a somewhat more accurate low-energy neutron dose, this comes at the expense of exponentially increasing the simulation time by increasing processing and memory requirements and in turn decreasing the stability of simulations.

Despite the failure of such a model to completely account for the thermal neutron doses, the model is overall quite successful at approximating doses from gammas and high-energy neutrons to first order, giving a sound model for calculating the approximate absorbed dose for rad-hard FPGA devices and hence useful lifetime estimates. Likewise, it demonstrates that the estimated SEU rates, which shall be presented in the following section, are based upon a sound physical model. While the residual inaccuracy in the thermal neutron doses is unfortunate (and largely due to computing trade-offs that must be made in the tracking thresholds), it should be noted that these are neutrons with too low of an energy to effectively contribute to the SEU cross-section, as opposed to the medium-energy neutrons of 50-100 MeV that are largely due to interactions with the magnet media and present a substantial portion of the SEU cross-section.

4.3 Calculated particle fluences and momenta spectra from PISA model

In this section, I shall present the calculated particle fluences and their corresponding momenta spectra for particles intersecting the Silicon annuli as simulated by the PISA model.

4.3.1 Particle fluences by type

In this section, I shall present an overview of the observed particle types incident upon the chip. In particular, this shall prove important when estimating the SEU contribution due to particles other than protons and neutrons, for which the SEU cross-sections are experimentally known. For the purposes of interpreting the particle ID distributions, a full listing of particles by GEANT particle ID type is provided in Table 4.4.

Figures 4.7 and 4.8 show the flux of incident particles upon the two annular regions. One will first notice the dominance of neutrons and γ in the particle flux, consistent with what has been observed both in the particle momentum spectra and the measured doses by the TLD badge. Likewise, the most prevalent charged particles appear to be pions (PID = 8 and 9), protons and anti-protons (PID = 14 and 15), and kaons (PID = 11 and 12), in addition to β^+ and β^- , which do not substantially contribute to SEU cross-section. Hence, the choice to examine the SEU contributions of these particular particle

Table 4.4 GEANT Particle ID types.

PartID	Particle
1	γ
2	e^+
3	e^-
4	ν
5	μ^+
6	μ^-
7	π^0
8	π^+
9	π^-
10	K_{long}^0
11	K^+
12	K^-
13	n
14	p
15	\bar{p}
16	K_{short}^0
17	η
18	Λ
19	Σ^+
20	Σ^0
21	Σ^-
22	Ξ^0
23	Ξ^-
24	Ω^-
25	\bar{n}
26	$\bar{\Lambda}$
27	$\bar{\Sigma}^-$
28	$\bar{\Sigma}^0$
29	$\bar{\Sigma}^+$
30	$\bar{\Xi}^0$
31	$\bar{\Xi}^+$
32	$\bar{\Omega}^+$
45	Deuteron
46	Triton
47	α
48	Geantino
49	He3
50	Cerenkov

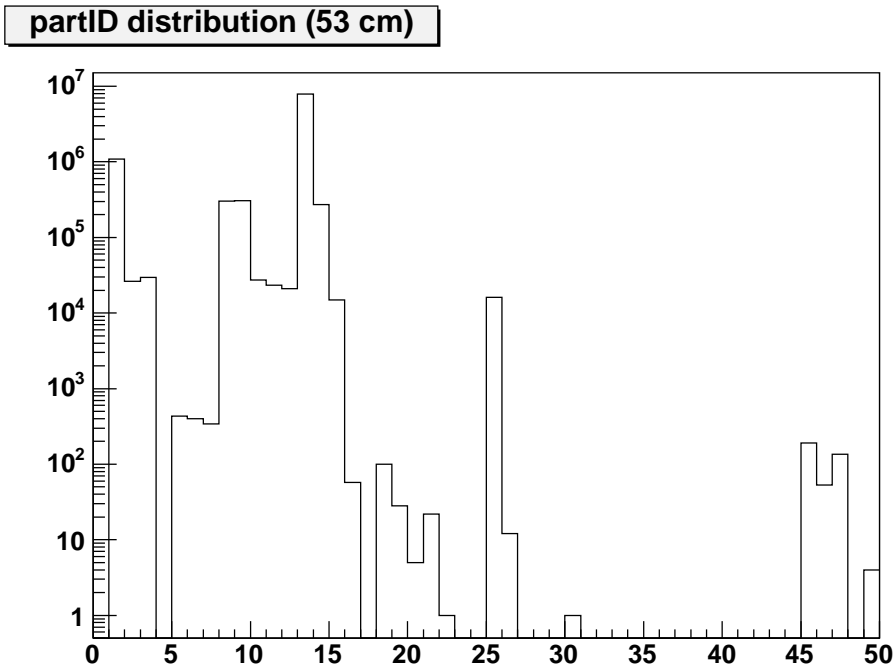


Figure 4.7 GEANT partIDs for particles incident upon the chip in PISA at $r = 53$ cm.

species appears to encompass most of the charged particle flux, and thus estimate most of the potential cross-section.

In the same fashion, the particle tracks created inside the Silicon annular regions can be studied (Figures 4.9 and 4.10), ultimately giving an estimate of the frequency of nuclear interactions induced by radiation as a function of position.

As Figures 4.11 and 4.12 show, this assumption that SEU cross-sections scale as a factor of the ratio of nuclear interaction cross-sections appears to be well-justified. The reasoning for this comes from the fact that one will notice the primary “source” particles for tracks inside the Silicon are neutrons (PID = 13), anti-protons (PID = 15), anti-neutrons (PID = 25), and pions (PID = 8 and 9). Hence it is clear that such particles should contribute substantially to the SEU cross-section.

However, the true test of this assumption shall come from examining the ratio of heavy particle fragment production inside Silicon annulus (i.e., α and other heavy, highly ionizing fragments) by protons as compared to other particle types, scaled appropriately by the relative fluences and interaction cross-section ratios; this test shall be done explicitly in a following section.

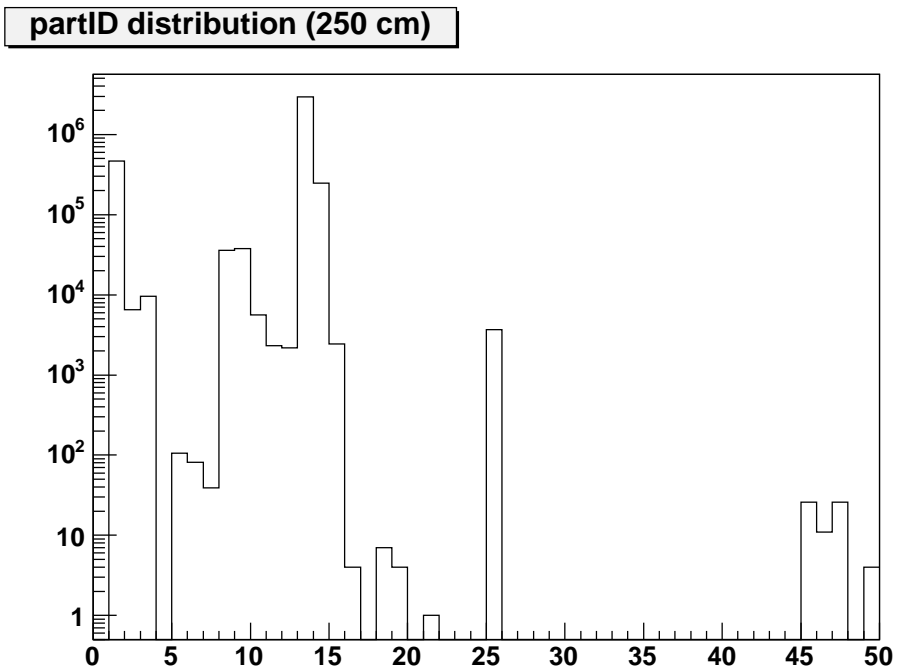


Figure 4.8 GEANT partIDs for particles incident upon the chip in PISA at $r = 250$ cm.

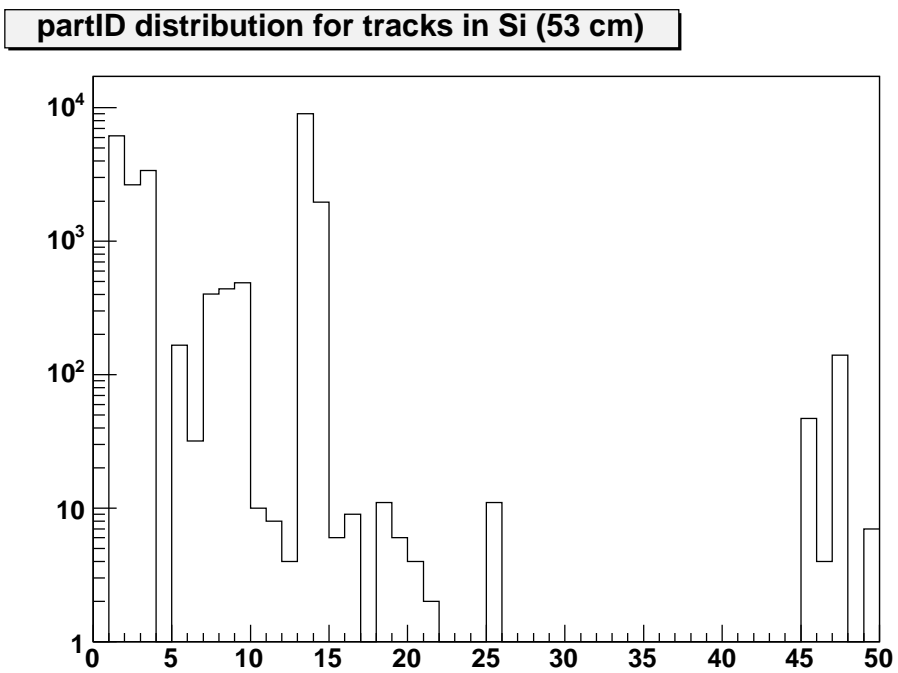


Figure 4.9 GEANT particle IDs for particle tracks in PISA originating inside the silicon annular region at $r = 53$ cm.

partID distribution for tracks in Si (250 cm)

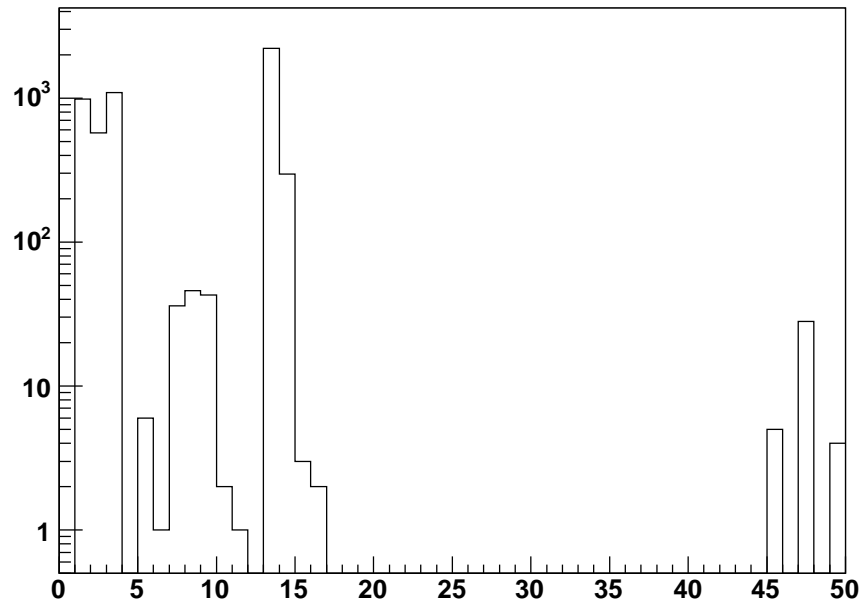


Figure 4.10 GEANT particle IDs for particle tracks in PISA originating inside the silicon annular region at $r = 250$ cm.

Parent PartID for heavy fragments (53 cm)

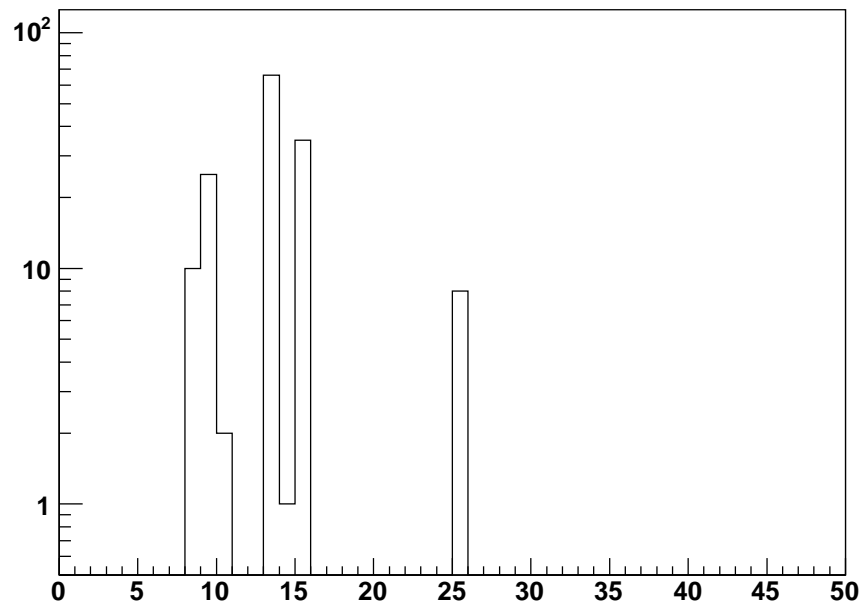


Figure 4.11 GEANT parent partIDs for heavy particle fragments ($PID > 40$) created inside the annular region at $r = 53$ cm.

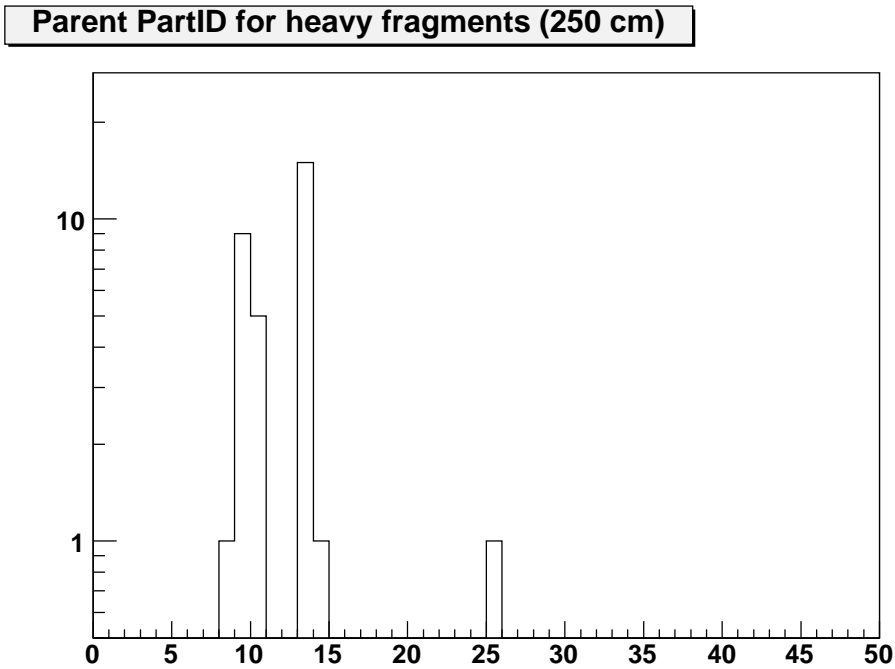


Figure 4.12 GEANT parent partIDs for heavy particle fragments (PID > 40) created inside the annular region at $r = 250$ cm.

4.3.2 Momentum spectra for selected particle types

In this section, I shall present the momentum spectra of particles intersecting the annular region whose SEU contributions were calculated in the PISA model. This shall serve as an important aspect of the analysis of the SEU contribution for various particle types, in particular due to the “selection” effects imposed by the magnetic field which screen out low-energy particles from intersecting the annuli, and in turn, the device under test.

4.3.2.1 Protons and anti-protons

Figures 4.13 and 4.14 give the momentum distribution for protons and anti-protons in the near and far positions, respectively.

One will observe that the momentum distribution for protons and anti-protons follows the expected exponential relationship, centered about a mean energy of around 680 MeV, which would indicate a significant selection bias of protons created in the collision, (as the mean temperature is taken to be approximately 350 MeV for protons).

In addition, both the near and far proton/anti-proton momentum spectra is the appearance of low-

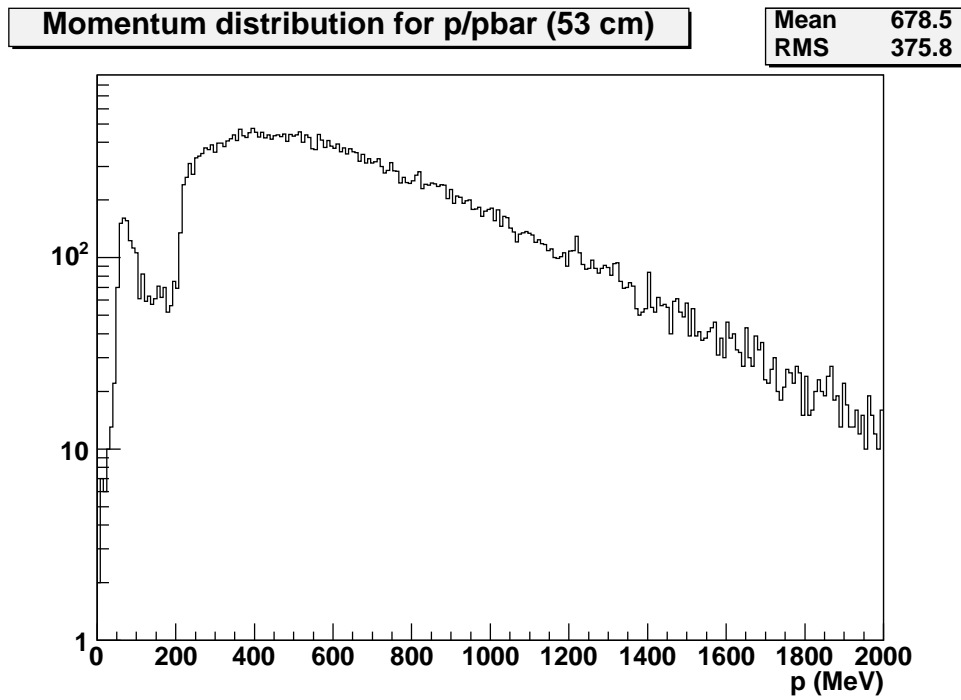


Figure 4.13 Momentum distribution of protons and anti-protons incident upon the annular region at $r = 53$ cm.

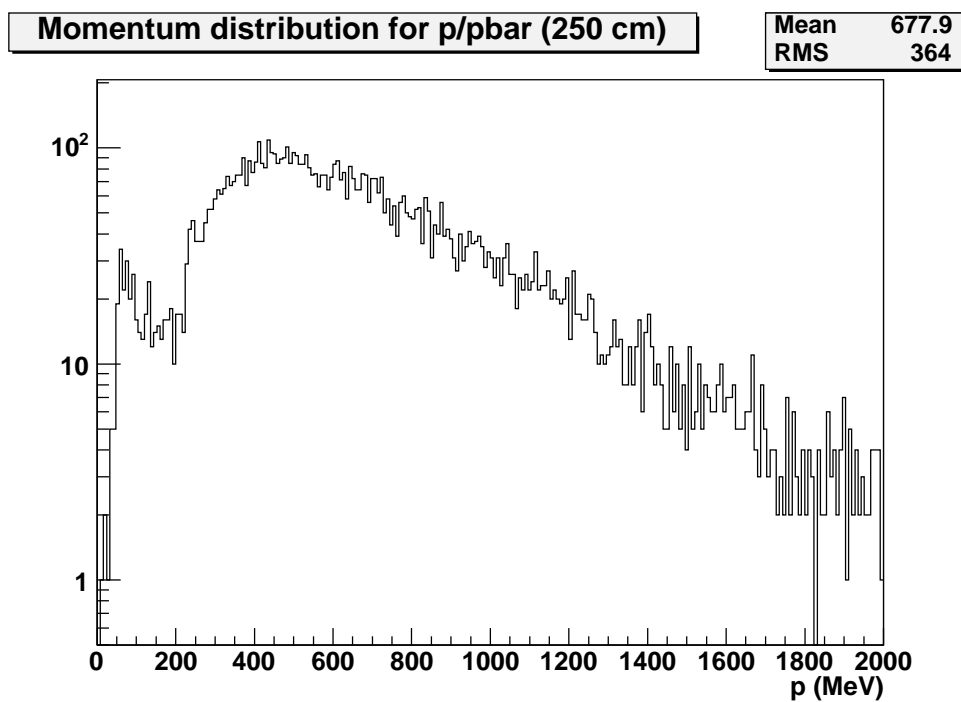


Figure 4.14 Momentum distribution of protons and anti-protons incident upon the annular region at $r = 250$ cm.

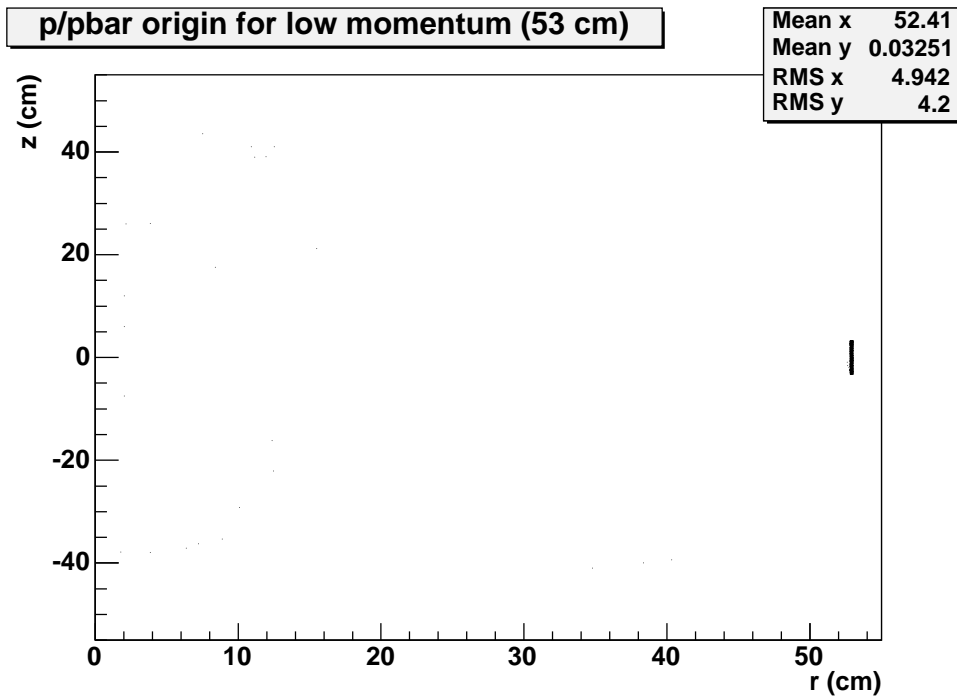


Figure 4.15 Origin of low-momentum ($p < 200$ MeV) protons and anti-protons incident upon the annular region at $r = 53$ cm.

energy proton peak, an artifact which shows up both in the near and far positions, similar to the very strong low-energy neutron peak. Figures 4.15 and 4.16 give the origin of such particles. From these, it is conclusively demonstrated that such a low-energy peak originates exclusively in the Aluminum layer adjacent to the Silicon.

4.3.2.2 Neutrons and anti-neutrons

The momentum distributions for neutrons and anti-neutrons in the near and far positions are given by 4.17 and 4.18.

Neutrons exhibit perhaps the most “interesting” behavior due to their strong domination by low-energy neutrons created by interactions with the magnet media, as demonstrated by Figures 4.19 and 4.19, which give a distribution of the neutron origin coordinates. Such low-energy neutron dominate the particle flux upon the chip by several orders of magnitude. However, these slower neutrons do not show up in the PISA simulation by default; rather, to observe these particles required setting the default tracking threshold energy for the magnet-related media from their nominal values of 50 - 150 MeV down to 50 keV. This in turn significantly increased the required simulation running time by exponentially

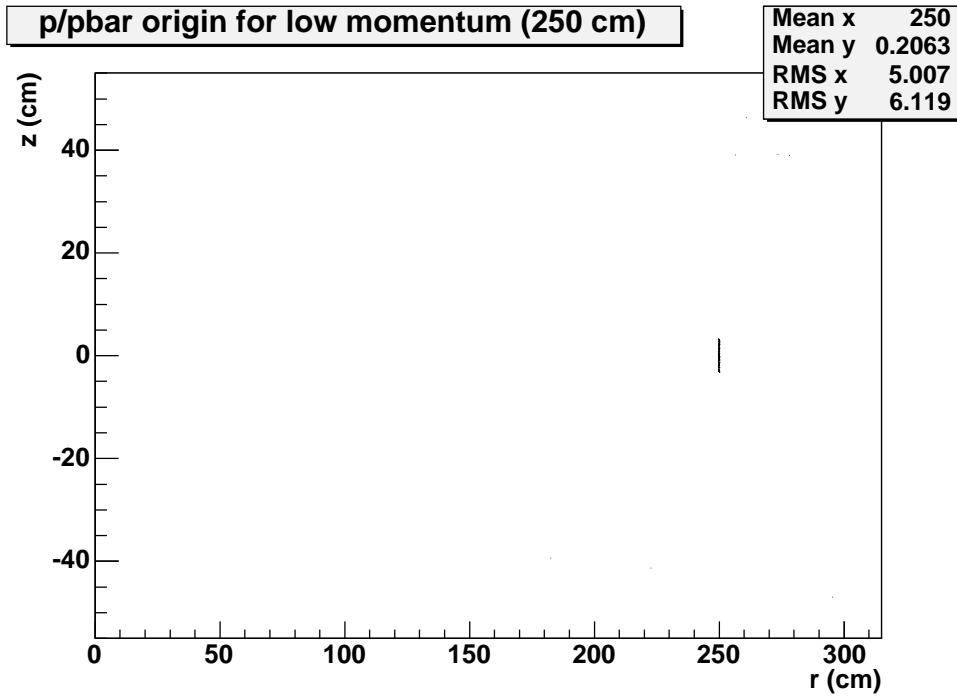


Figure 4.16 Origin of low-momentum ($p < 200$ MeV) protons and anti-protons incident upon the annular region at $r = 250$ cm.

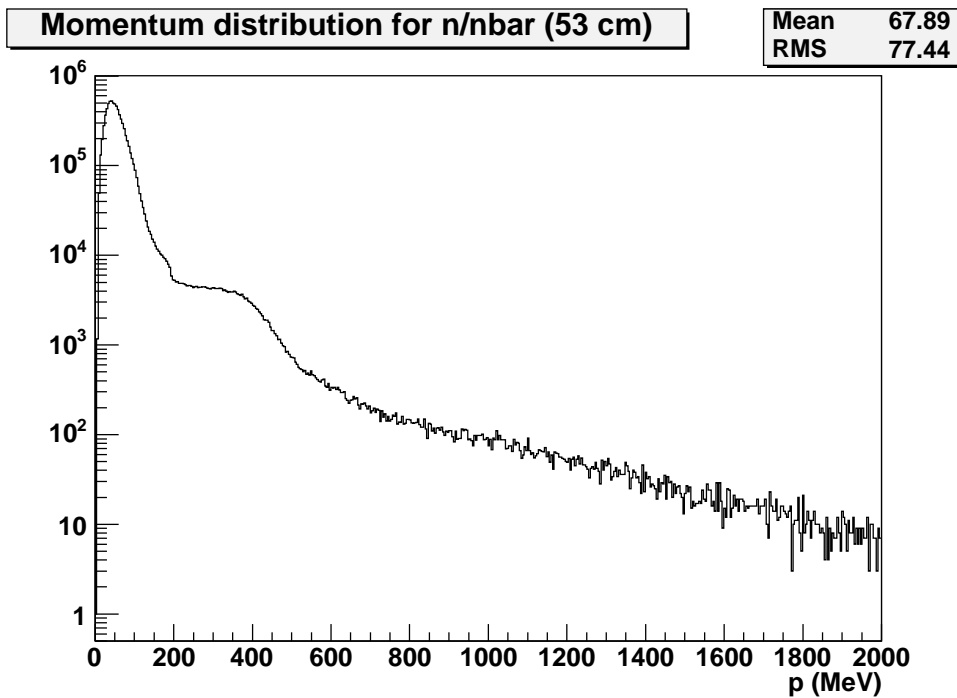


Figure 4.17 Momentum distribution of neutrons and anti-neutrons incident upon the annular region at $r = 53$ cm.

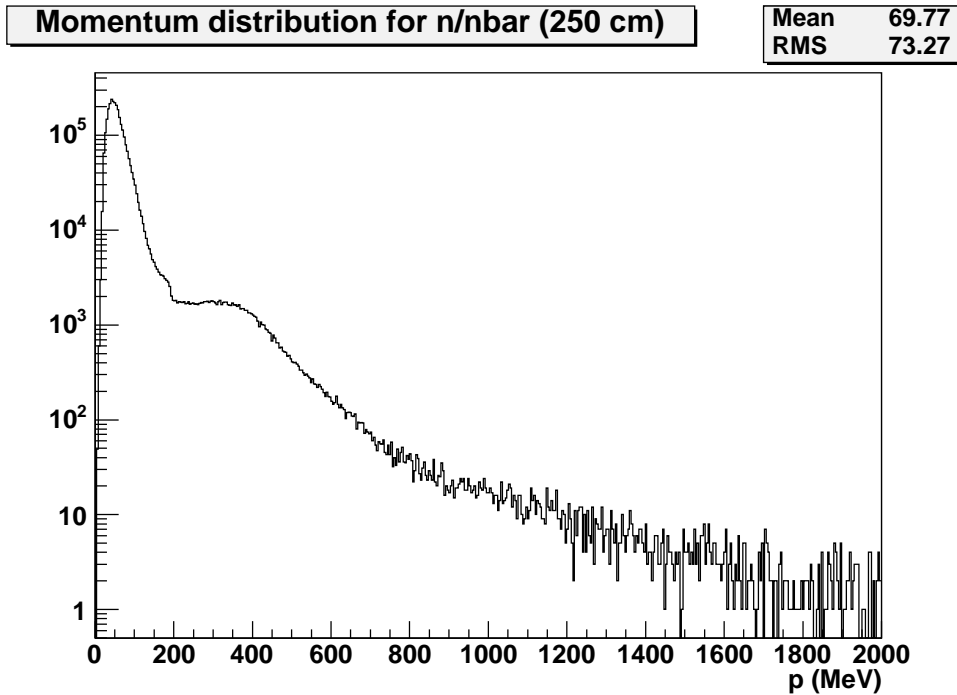


Figure 4.18 Momentum distribution of neutrons and anti-neutrons incident upon the annular region at $r = 250$ cm.

increasing the number of particles tracked. Nonetheless, lowering this tracking threshold proved vital to correctly estimating both the neutron doses (in the low and high-energy regimes) as well as the total SEU rate.

To examine whether the shape of the neutron momentum distribution contained “artifacts” due to tracking cutoffs from non-magnet media, the momentum distribution of neutrons originating from within the magnet media (i.e., $6 \text{ cm} < r < 60 \text{ cm}$, $|z| > 40 \text{ cm}$). The neutron momentum distributions for neutrons originating within the magnets are plotted in Figures 4.21 and 4.22. As one will observe, the low-energy peak originates entirely from within the magnet media, with the high-energy “tail” originating from other sources, including those created from the collisions.

Given the strong dominance of low-energy neutrons, it should come as little surprise that neutrons also strongly contribute to the SEU cross-section, composing approximately 22.5% of the total SEU cross-section in the near position and 30.5% of the cross-section in the far.

In addition, the low-energy neutron “peak” corresponds roughly to the interaction energy onset - Figure 4.23 clearly shows a “peak” interaction energy beginning around 50 MeV. As I shall demonstrate in the following chapter, this energy also corresponds roughly to the “onset” energy of the neutron

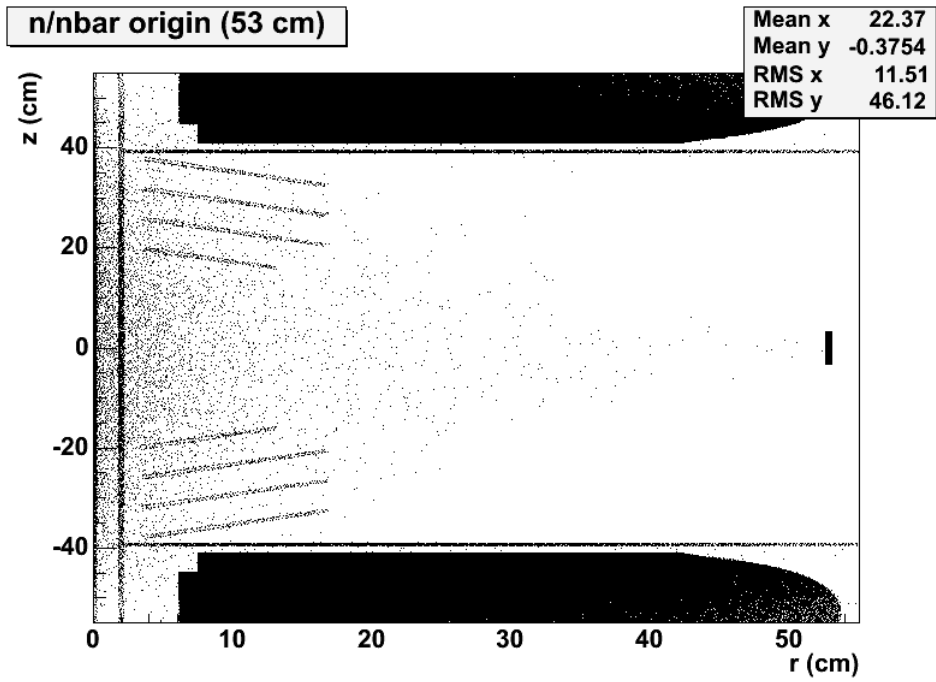


Figure 4.19 Origin coordinates of neutrons incident upon the annular region at $r = 53$ cm.

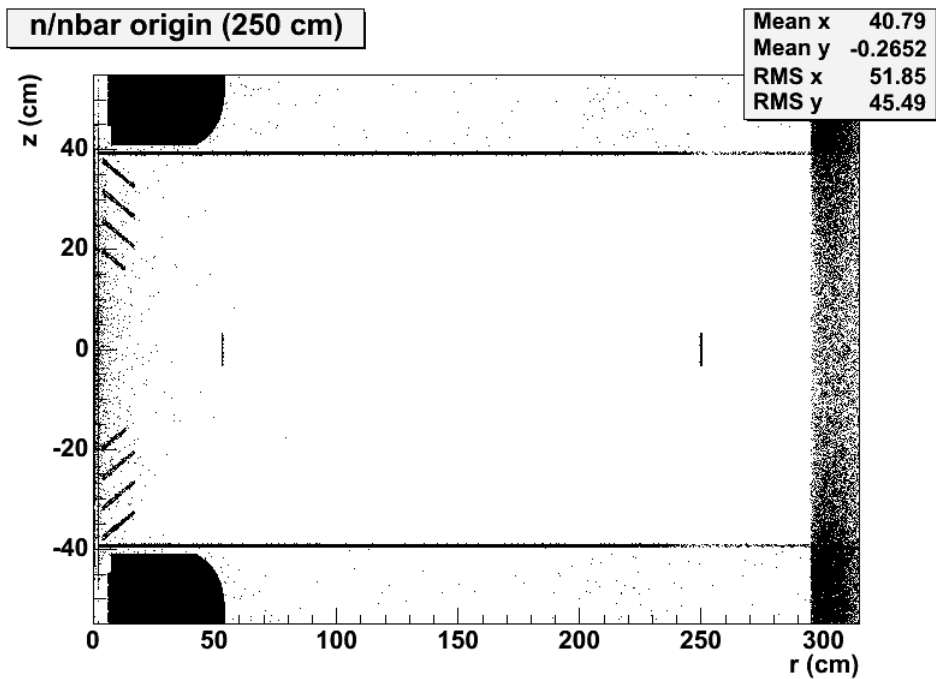


Figure 4.20 Origin coordinates of neutrons incident upon the annular region at $r = 250$ cm.

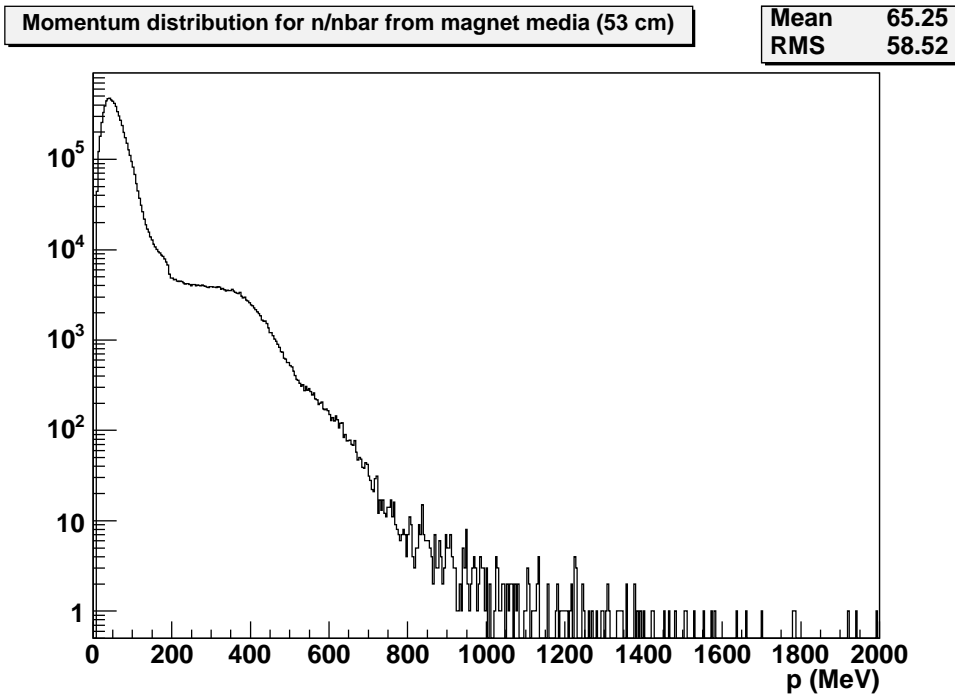


Figure 4.21 Momentum distribution of neutrons originating from the magnet media incident upon the annular region $r = 53$ cm.

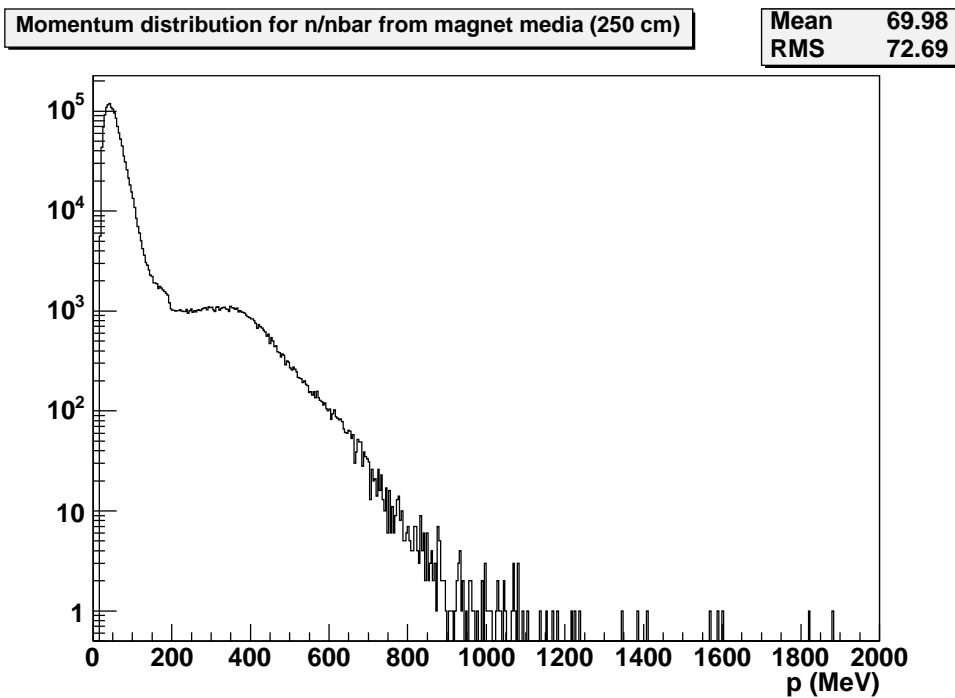


Figure 4.22 Momentum distribution of neutrons originating from the magnet media incident upon the annular region $r = 250$ cm.

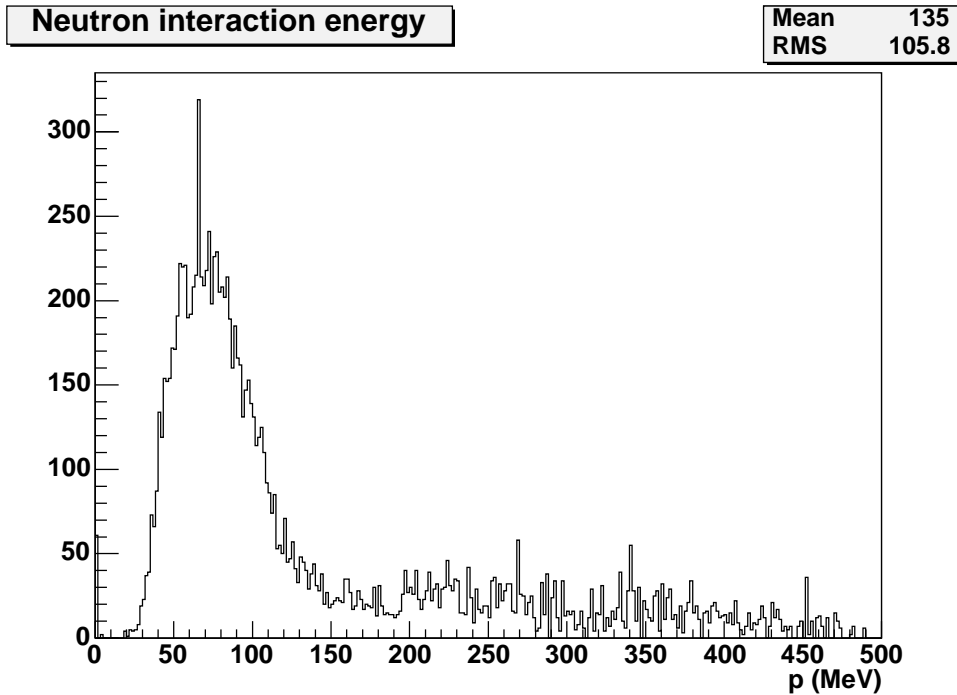


Figure 4.23 Momentum distribution for neutrons/anti-neutrons with child particles created inside the annular region.

Weibull curve derived for the neutron SEU cross-section.

4.3.2.3 Kaons

The momentum distributions for kaons in the near and far positions are given by 4.24 and 4.25. Similar to the case of protons, the kaon distribution neatly follows the expected distribution pattern. Kaons appear to show a similar mean momentum to protons and anti-protons as well, underlying a consistency in the selection bias of particles incident upon the annular regions due to the influence of the magnetic field.

4.3.2.4 Pions

The momentum distribution of pions is given in figures 4.26 and 4.27. Both distributions also follow the same expected momentum distribution pattern consistent with the particle production distribution, with the exception of one curious artifact: a momentum “peak” in the far position at low momentum, due to the incidence of particle decays into pions. Such a peak is pronounced in the far position due to the simple matter of transit time - a longer transit time will ultimately lead to more particles decaying

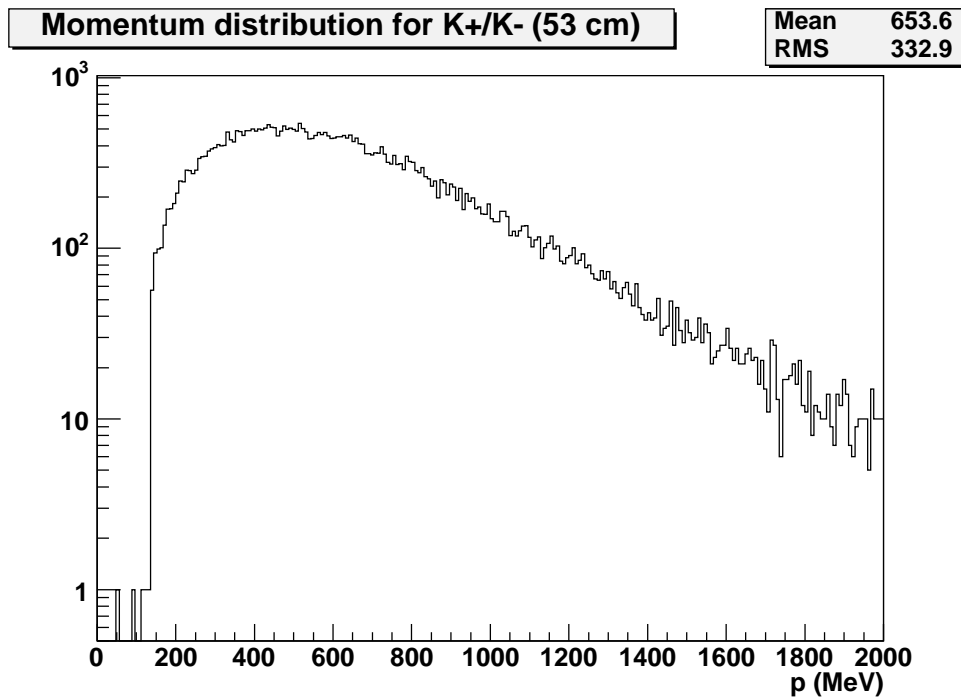


Figure 4.24 Momentum distribution of kaons incident upon the annular region at $r = 53$ cm.

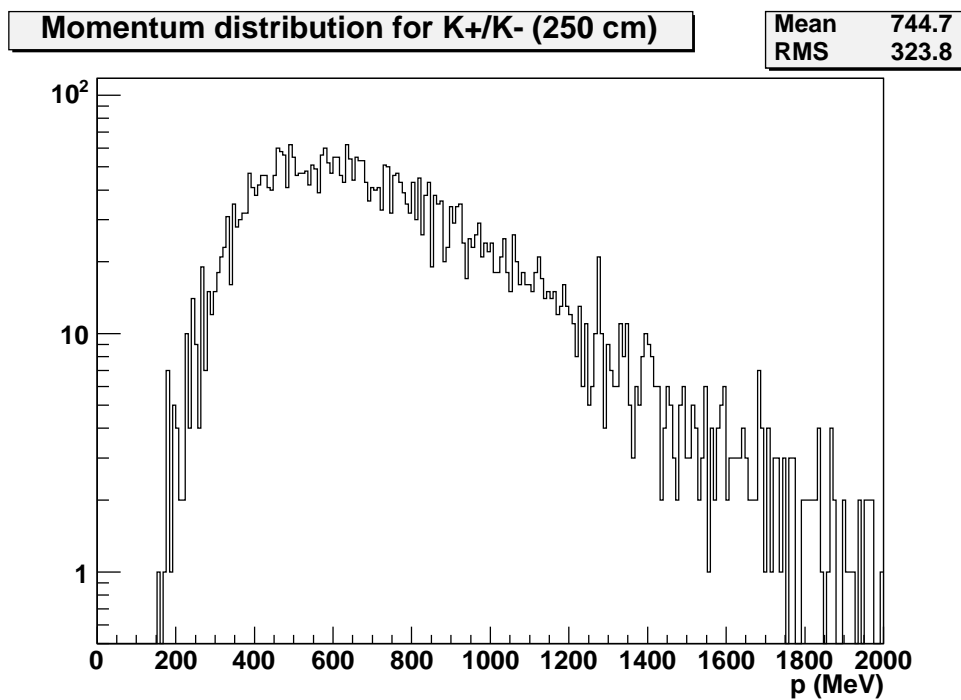


Figure 4.25 Momentum distribution of kaons incident upon the annular region at $r = 250$ cm.

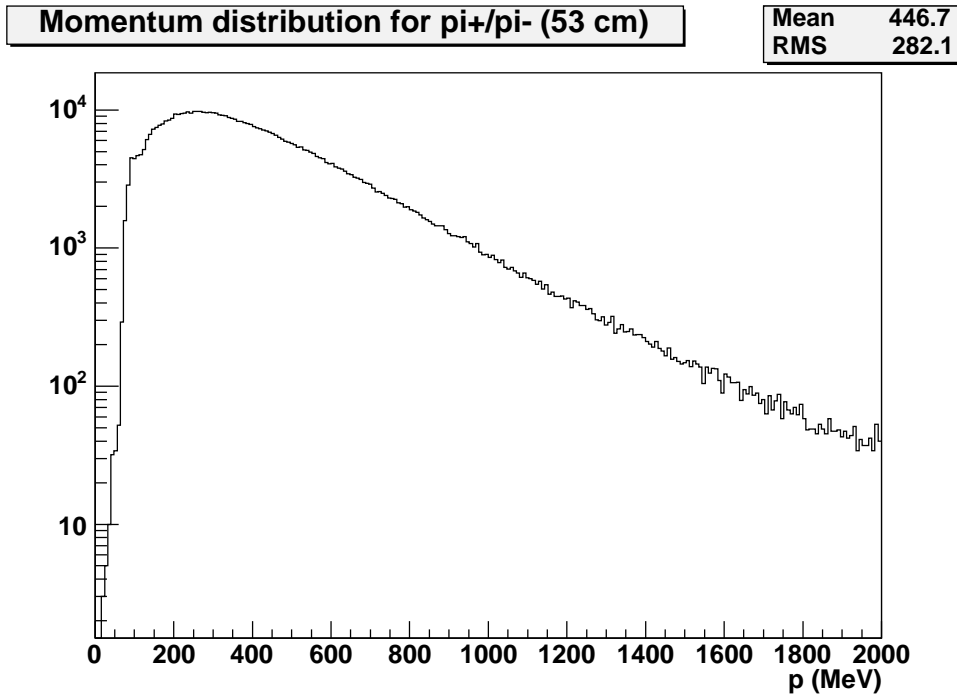


Figure 4.26 Momentum distribution of pions incident upon the annular region at $r = 53$ cm.

before they reach the annular region.

Similar to prior cases of protons and anti-protons the origin coordinates of pions is plotted in Figures 4.28 and 4.29. Unlike the case of protons, the origin of the low-momentum pions is not clearly limited to one region of the IR. Rather, the low-energy peak appears to be a combination of collision products, decays, interactions with the magnet media, and interactions with the Aluminum layer adjacent to the Silicon.

4.4 Summary

In this chapter, I have presented an overview of the PISA model used to simulate the experimental setup, including the basic assumptions made in constructing the PISA model with HIJING event generator, by the means by which a human-equivalent dose was calculated by particle fluences in the PISA model. This dose was then compared to the dose as measured by the attached TLD badges, giving a quantitative measure of the quality of the PISA model. Overall it was found that the model was highly successful at calculating the radiation dose to first order, with the average variance being on the order of 25 – 30% for γ . While the neutron dose showed a higher degree of variance, it nonetheless still

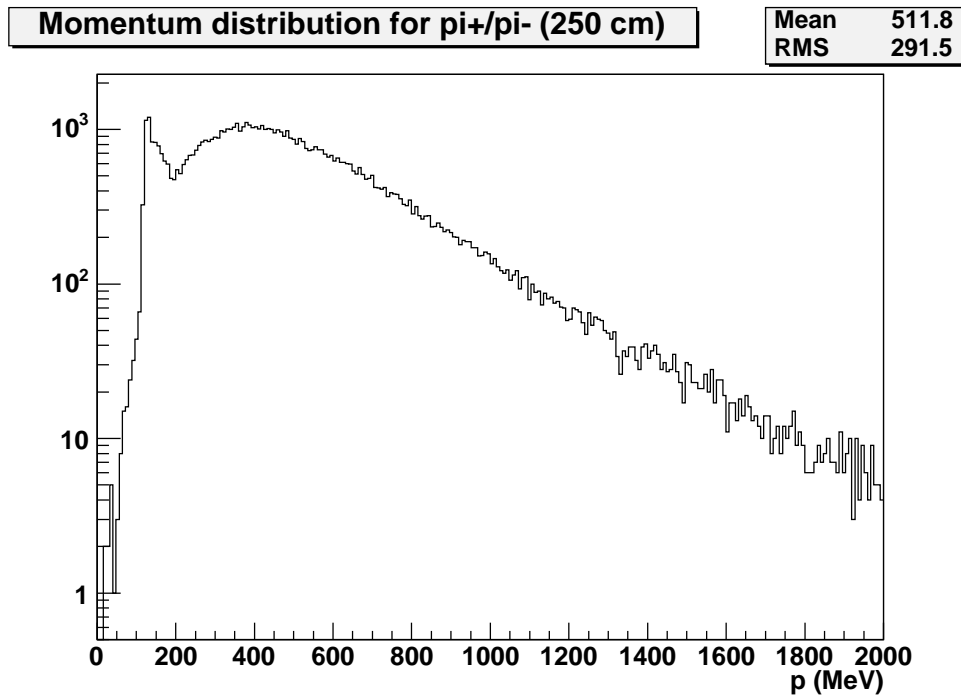


Figure 4.27 Momentum distribution of pions incident upon the annular region at $r = 250$ cm.

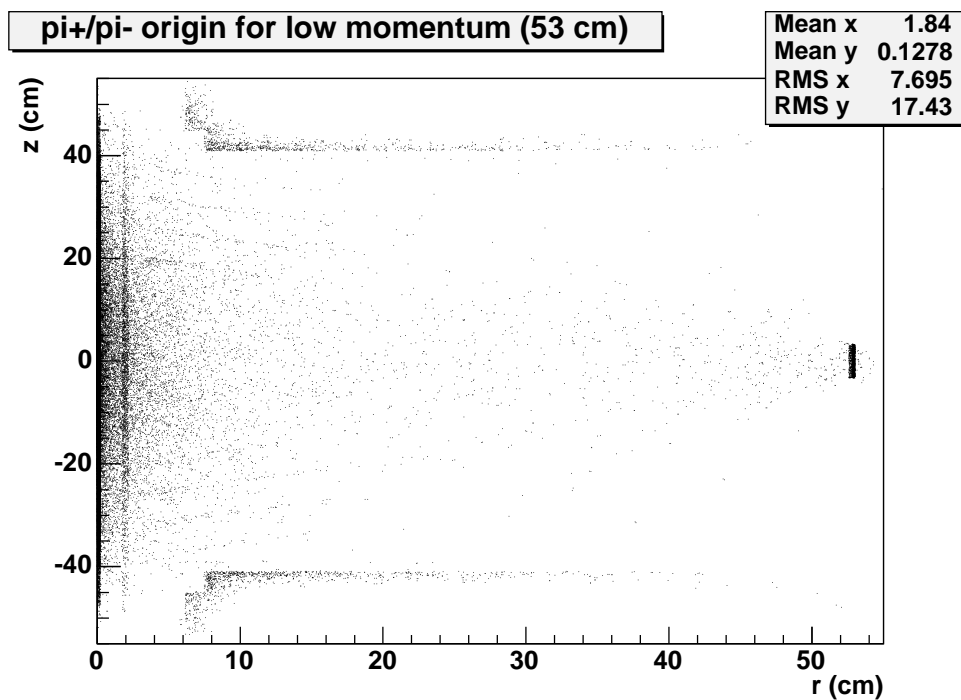


Figure 4.28 Origin of low-momentum ($p < 200$ MeV) pions incident upon the annular region at $r = 53$ cm.

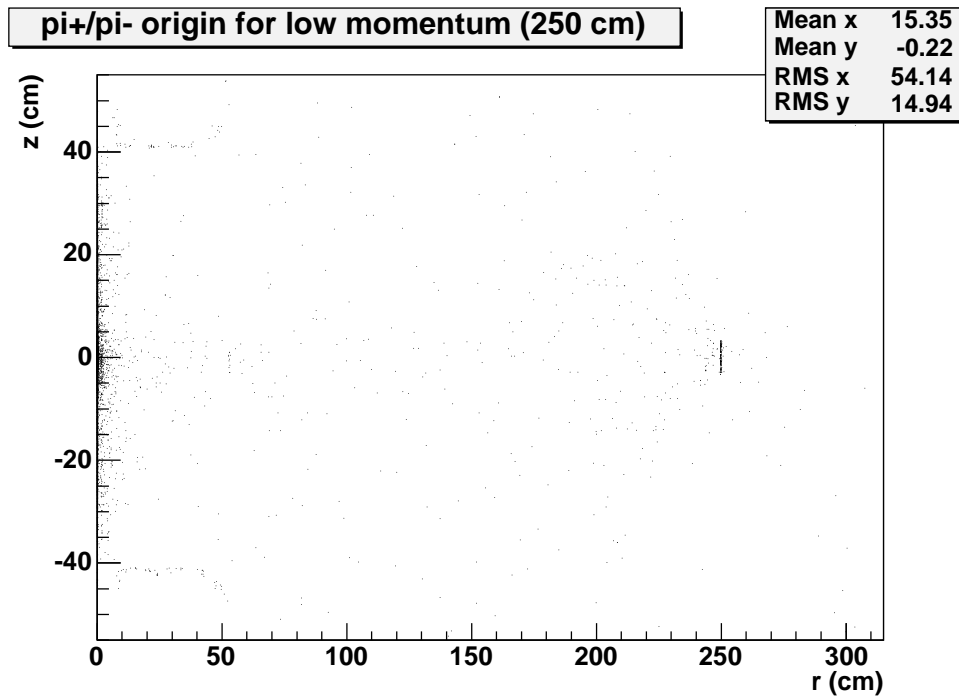


Figure 4.29 Origin of low-momentum ($p < 200$ MeV) pions incident upon the annular region at $r = 250$ cm.

came within the correct order of magnitude as the dose observed by the TLD badges, indicating that the PISA model provides a sound basis for characterizing the radiation dose for use with on-detector electronics, and hence for calculating an estimated upset rate for a given device in the IR.

In addition to analyzing the types of particles incident upon the chip, I have presented the momentum spectra for particles whose SEU cross-section contribution was tallied (i.e., protons/anti-protons, neutrons/anti-neutrons, kaons, and pions), as well as the relative origins of these particular particles. This proves to be an especially important consideration for particles such as neutrons, which were found to be generated chiefly through interactions the magnet media, rather than from collision products.

5 PREDICTIONS AND ANALYSIS OF RESULTS FROM PISA MODEL

In this chapter, I shall present the method by which the SEU rate was calculated in the PISA model, then comparing this to the observed SEU rate in the experiment. Specifically, I shall detail the method in which the SEU cross-section contribution was calculated for particles where the SEU cross-section is not known directly, such as from neutrons and more “exotic” particle types like pions and kaons. Following from this, I shall present the relative SEU cross-section contributions from the PISA model of each of the classes of particles considered: protons, from the data provided by Xilinx, neutrons, from the Weibull curve I shall estimate in this section, and others (such as pions and kaons), through the proton Weibull curve scaling I shall also detail in this section.

In addition, I shall present an analysis of the assumption used with regards to scaling the SEU cross-section for protons by the ratio of the nuclear interaction cross-section of the particle in question to that of protons. This shall be done by evaluating the number of heavier particle “fragments” generated within the Silicon and comparing this to the actual generation rate by these particle types. Specifically, this rate shall be evaluated under the assumption that the production of such heavy fragments has a direct correspondence to the SEU rate.

Given this, it logically follows that if the SEU rate directly scales with nuclear interaction cross-section ratio, the rate of production of heavy fragments, normalized to the flux ratio between protons and other charged particles, should be roughly equal. Hence, this assumption shall be directly tested to evaluate the assumption regarding the scaling of the SEU cross-section for non-protons.

I shall also present an evaluation of the systematic errors in the PISA model, including those introduced by use of the Weibull cross-section fit to the available neutron data, the scaling factors used for applied to the Weibull curve for protons to find the SEU cross-section contributions of other particle types, and from the fluences calculated by PISA itself.

Finally, based upon the PISA model I shall examine areas of uncertainty which still exist in the PISA model and propose various considerations for improvement of future similar experiments.

5.1 Estimation of SEU cross-section contribution of individual particles by particle type

In this section, I shall present the method by which the SEU cross-section contribution for various particle types was calculated. For neutrons, this shall involve the calculation of an energy-dependent Weibull curve based upon available integrated cross-section data for a given neutron energy spectrum. Likewise, for charged particles other than protons whose SEU contribution is an unknown, an energy-dependent “scaling factor” based upon the nuclear interaction cross-section ratio applied to the known Weibull curve for protons shall be introduced and discussed in the following section. Finally, I shall present the relative SEU cross-section contribution for each of the classes of particles considered for each of the positions, based upon the SEU contribution as calculated by the PISA model.

5.1.1 Estimation of a Weibull curve for neutrons based upon integrated cross-section data

5.1.1.1 Introduction

In this section, I shall present an estimated Weibull SEU cross-section curve for neutrons. The motivation for this comes from the fact that SEU cross-sections for neutrons as measured by Xilinx at the LANSCE test facility [3] in addition to independent testing by iRoC [2] estimate the SEU cross-section from neutrons in the following form:

$$\sigma_{\text{SEU}} = \frac{N_{\text{errors}}}{\int \text{Fluence} \cdot dt} \quad (5.1)$$

where the fluence is taken as the integral of the flux distribution as a function of energy, and the fluence rate is taken to be a constant as a function of time. While such a form provides a rough means of estimating the SEU rate due to conditions such as atmospheric neutron flux (which is of particular interest for aerospace applications), it does not provide an actual differential neutron cross-section as a function of energy useful for characterizing the SEU cross-section contribution of neutrons. Rather, while such a “cross-section” carries the appropriate units, it is in fact a convolution of an assumed spectrum (taken to simulate the Hess spectrum of atmospheric neutrons) and the neutron SEU cross-section of the device - hence it is not a “true” cross-section.

Thus the goal of this section shall present a means of estimating a differential SEU cross-section distribution for a Xilinx Virtex-II family device. Chief among the assumptions in this shall be that the SEU cross-section distribution for neutrons will be of the form of a Weibull curve, the functional form

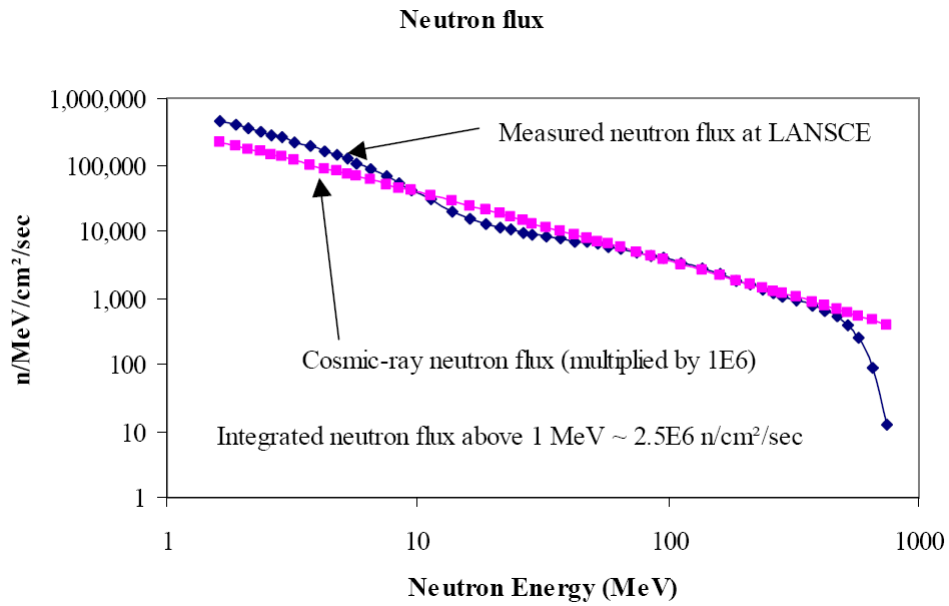


Figure 5.1 Graph of LANSCE neutron spectrum as compared to atmospheric Hess spectrum [2].

as that found for protons. This assumption shall be tested along with alternative forms, in addition to a detailed description of the data used to make this estimate, the methodology in making such a fit to the given functional form, and a deviation from measured SEU rates for neutron exposure that such an estimate provides.

5.1.1.2 Data used for estimate

In independent tests at Los Alamos National Laboratory’s Atmospheric Neutron Science Center, (more commonly known as LANSCE), both Xilinx and iRoC tested the upset rate of a Virtex-II family FPGA in order to test the susceptibility of FPGAs to bit upsets due to atmospheric neutrons. LANSCE’s facility provides an ideal location for accelerated testing due to the fact that its generated neutron spectrum (created through neutron spallation with a Tungsten element) approximately models the Hess spectrum of atmospheric neutrons, scaled by approximately a factor of 10^6 , as shown in Figure 5.1.

Table 5.1 gives the estimated cross-sections provided by Xilinx and iROC, respectively for the Virtex-II family device tested, in terms of an integrated cross-section. Note that Xilinx’s data provides two bins - one of neutron energies above 1.5 MeV, and a second of neutron energies above 10 MeV. Based upon the analysis provided with the iRoC data, in particular their estimation of a “failure in time” rate based upon the flux of atmospheric neutrons of energy > 10 MeV at the level of New York City, it

Table 5.1 Neutron SEU cross-sections per device for a Xilinx Virtex-II family device, as measured by iRoC [2] and Xilinx [3].

Measurement	Cross-section (cm ⁻²)
Xilinx (> 1.5 MeV)	3.53E-7
Xilinx (> 10 MeV)	6.72E-7
iRoC (> 10 MeV)	6.19E-7
iRoC (14 MeV)	3.53E-7

was assumed that iRoC’s spectrum estimates were also for neutrons of energy > 10 MeV. As Table 5.1 shows, this would appear to be a justified assumption, based upon the consistency of this measurement with that of Xilinx.

In addition to the LANSCE data, iRoC also made a measurement of the SEU sensitivity of a Virtex-II device based upon a mono-energetic beam of 14 MeV neutrons. This data was used in addition to the other data points to test the calculated Weibull curve at a specific energy point.

5.1.1.3 Methodology

To obtain the desired Weibull fit, the general Weibull form was taken in Root’s `TMinuit` minimization class [26], minimizing parameters (allowed to freely float) through a standard chi-square test.

Using the functional Weibull form with variable parameters for the saturation cross-section σ_{sat} , onset parameter E_0 , width parameter W , and “dimensional exponent” s , the integrated cross-section for the > 1.5 MeV and > 10 MeV bins was found by taking a spline fit to the LANSCE spectrum and integrating over the appropriate energy, normalized by the integrated fluence, i.e.:

$$\sigma_{>n} = \frac{\int_n^{1000} f(E) \cdot \frac{\partial \sigma}{\partial E} \cdot dE}{\int_n^{1000} f(E) \cdot dE} \quad (5.2)$$

Rewriting this as a discrete integral used with energy “slices” of width $\Delta E = 0.1$ MeV yields:

$$\sigma_{>n} = \frac{\sum f(E) \cdot \frac{\partial \sigma}{\partial E} \cdot \Delta E}{\sum f(E) \cdot \Delta E} \quad (5.3)$$

Thus, by allowing the Weibull parameters to freely float and minimizing the chi-square value for the integrated > 1.5 MeV and > 10 MeV bins and the 14 MeV bin, the resulting equation was found to be:

$$\frac{\partial \sigma}{\partial E} = 3.77022 \cdot 10^{-14} \cdot \left(1 - e^{\left[\frac{(E-1.55605)}{14.9246} \right]^{2.36971}} \right) \quad (5.4)$$

Where the cross-section is measured in $\frac{1}{cm^2 \cdot bit}$ and E is in MeV.

Table 5.2 Predicted SEU cross-section values for a Virtex II-family device from a minimized Weibull-form fit to Xilinx and iRoC data, with offsets from measured values.

Measurement	Predicted (cm^{-2})	Offset (%)
Xilinx (> 1.5 MeV)	$3.52538 \cdot 10^{-7}$	-0.0000574876
Xilinx (> 10 MeV)	$6.71781 \cdot 10^{-7}$	-0.000101647
iRoC (14 MeV)	$3.52939 \cdot 10^{-7}$	-0.000170747

Table 5.3 Predicted SEU cross-section values for a Virtex II-family device from a minimized linear fit to Xilinx and iRoC data, with offsets from measured values.

Measurement	Predicted (cm^{-2})	Offset (%)
Xilinx (> 1.5 MeV)	$3.28713 \cdot 10^{-7}$	-6.75835
Xilinx (> 10 MeV)	$6.92872 \cdot 10^{-7}$	3.13957
iRoC (14 MeV)	$1.2772 \cdot 10^{-8}$	-96.3812

5.1.1.4 Comparison of estimated Weibull curve to measured results

Table 5.2 gives a comparison between the predicted and measured values for an Xilinx XC2V6000 FPGA, with the corresponding errors.

One will notice the good adherence to all of the data points provided by the minimized Weibull curve. While the number of data points used for the fit is limited (and hence the actual values of the parameters would likely depend upon more data), the Weibull form appears to be capable of accurately fitting the available data.

To test the uniqueness of such a fit, other fit forms were attempted, including linear, polynomial, and logarithmic fits. Only a linear fit (given by Equation 5.5) provided any meaningful adherence to the provided data points, yet as Table 5.3 shows, such a fit is of significantly poorer quality than the Weibull fit, although yielding a lower bound upon the systematic error from such a fit.

$$\frac{\partial \sigma}{\partial E} = 3.06086 \cdot 10^{-16} \cdot E - 3.63309 \cdot 10^{-15} \quad (5.5)$$

Figure 5.2 gives a graphical comparison of the minimized Weibull and linear fits to the available SEU data, with the SEU cross-section from iRoC's test with a mono-energetic beam of 14 MeV neutrons [2]. To first order, one will notice that the shape of the linear SEU cross-section distribution approximates the Weibull curve, yielding aggregate divergence rates which differ by less than 10%. Yet the linear fit clearly underestimates the low-energy neutron cross-section, most notably demonstrated by the very

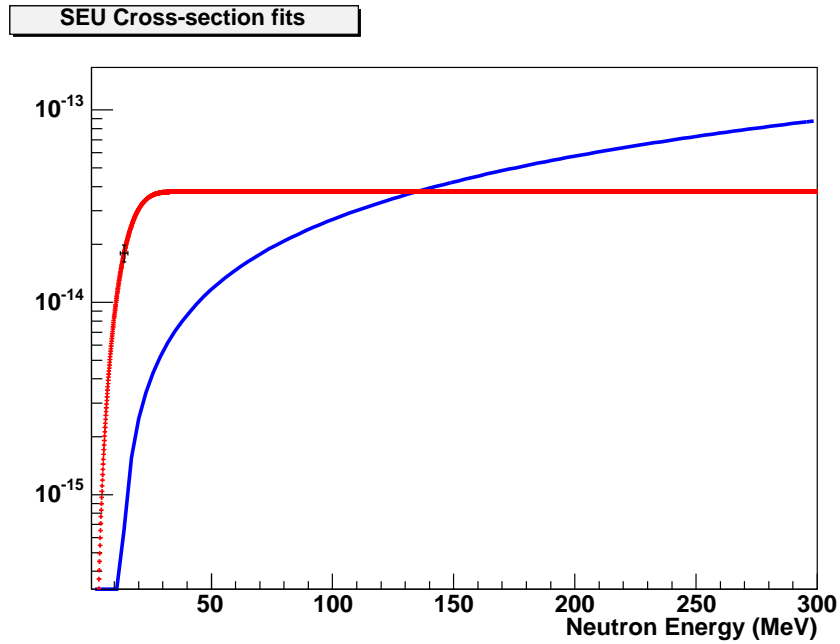


Figure 5.2 Comparison of minimized Weibull SEU cross-section distribution fit with systematic errors from parameter fitting (red) to linear SEU cross-section fit (blue). 14 MeV neutron cross-section as measured by iRoC is also plotted with corresponding systematic errors [2]. Cross-section is given in $\text{cm}^{-2} \cdot \text{bit}^{-1}$.

large divergence in the linear fit from the 14 MeV data, which is matched to very high precision by the Weibull fit. This would indicate that while the “rising edge” of the linear fit allows it to give a gross approximation of the integrated cross-section bins, it does not have the “saturation value” inherent to the Weibull distribution which appears to be an essential component of the cross-section distribution.

Thus, the Weibull form’s fit to the available neutron SEU data appears to expose information on the real physical properties of the neutron cross-section as a function of energy: namely, that such any fit to such a cross-section must contain an “onset” energy where the cross-section “begins” as well as a “saturation” cross-section whereupon the cross-section ceases to increase with increasing energy. Thus, the Weibull form, having such parameters, is capable of accurately modeling the measured SEU cross-section spectrum from neutrons.

While the quality of the fit in its adherence to all of the measured data points merits further examination of the “width” and “onset” parameters, the fact that there is no cross-section measurement for neutron fluences below 1.5 MeV prohibits making definite assumptions about the shape of the curve below these energies. Such data may prove to “bend” the onset and width parameters appropriately,

Table 5.4 Fractional SEU cross-section contribution by particle type for the near and far positions in PISA.

Source	% SEU Contribution	
	Near ($r = 53$ cm)	Far ($r = 250$ cm)
Protons	12.8159	43.3346
Neutrons	22.5973	30.3534
Pions	58.9517	23.4366
Others	5.6315	2.87543

although it would not impact the saturation cross-section, which can be verified from the existing data.

5.1.2 Calculation of SEU cross-section contribution for other particle species

While the cross-section of protons is known as a function of incident particle energy [5] (and the cross-section distribution of neutrons having been estimated in the prior section), this is not true for other more “exotic” particle types which are prevalent in collision products, including pions and kaons.

The assumption was made that the SEU cross-sections of such particles directly scaled to the interaction cross-section of such particles with protons at the same kinetic energy [28]. Thus, for each type of particle, a scale factor was determined by taking the ratio of the measured interaction cross-section over the proton-proton interaction cross-section at the same energy. This in turn accounts for both the lower mean interaction cross-section as well as the several resonance energies for particles such as pions and kaons that a fixed scale factor could not account for.

Using the kinetic energy of the incident particle and the known cross-sections for protons and neutrons, the SEU cross-section contribution for other particle types was calculated by scaling the result through the nuclear interaction cross-sections. Thus a total interaction cross-section per event was tallied for each layer, averaged as a function of integrated luminosity and appropriately scaled for the relative area of the annulus.

This process was carried out for all particle types with a significant proton interaction cross-section, including anti-protons, anti-neutrons, π^+ , π^- , K^+ , and K^- . For the special case of anti-neutrons, it was assumed that the anti-neutron cross-section scaled to the neutron cross-section approximately as the same ratio as anti-protons to protons [20]. These “scaling factors” are shown as a function of particle energy relative to the proton Weibull distribution in Figures 5.3 - 5.5.

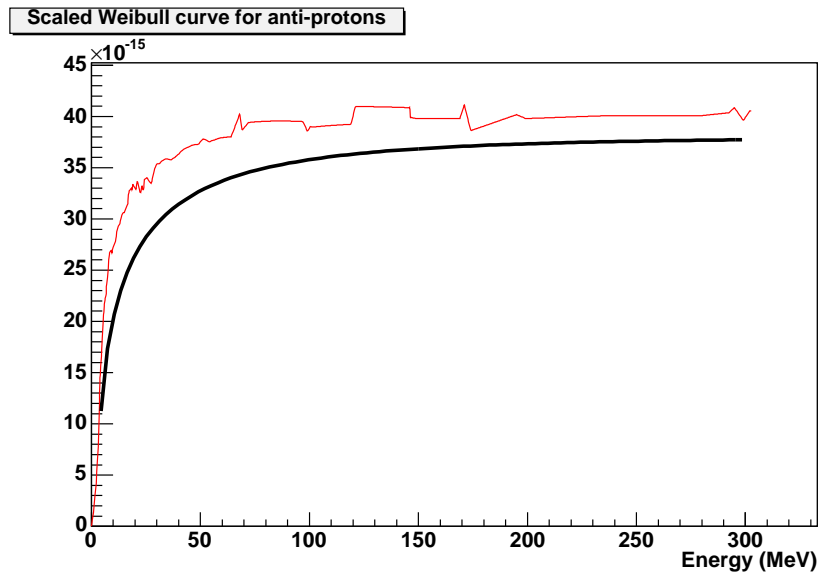


Figure 5.3 Comparison of Weibull distribution for protons from Xilinx [5] (black), as compared to the estimated cross-section for anti-protons, estimated from the nuclear interaction cross-section ratio to protons.

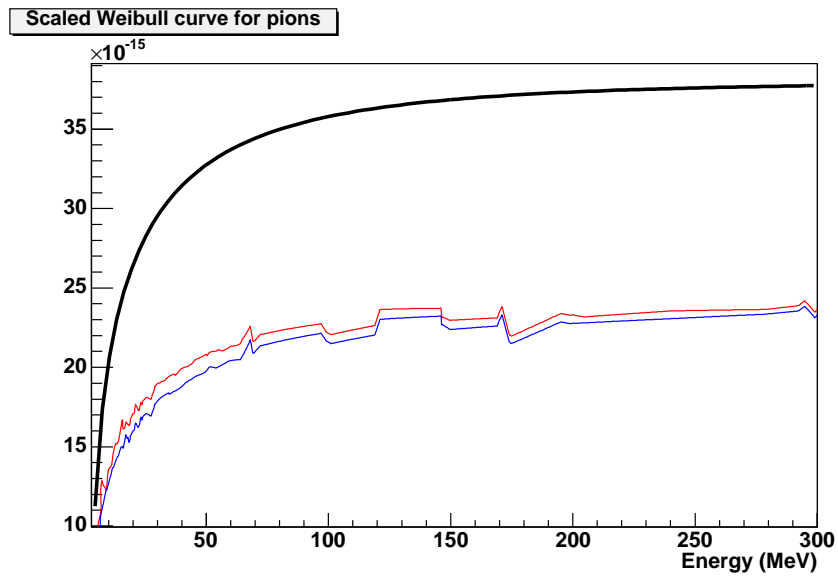


Figure 5.4 Comparison of Weibull distribution for protons from Xilinx [5] (black), as compared to the estimated cross-section for π^- (red) and π^+ (blue), estimated from the nuclear interaction cross-section ratio to protons.

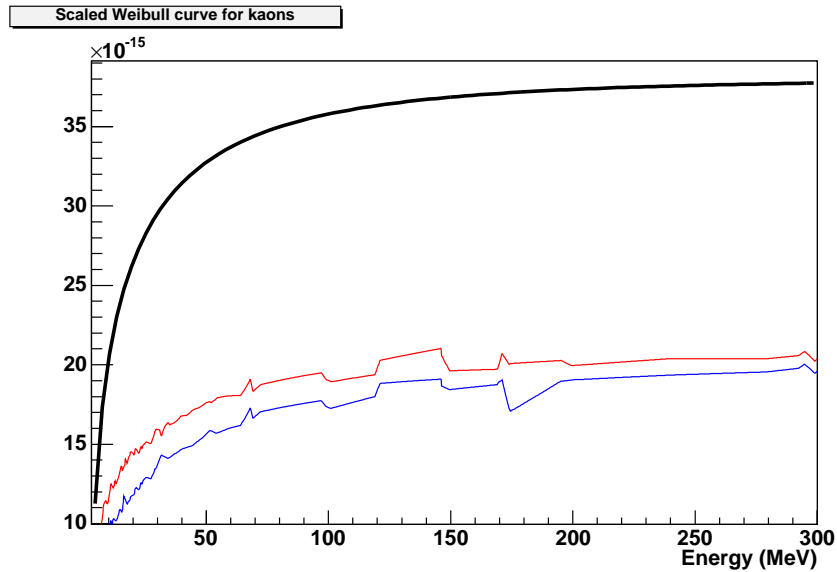


Figure 5.5 Comparison of Weibull distribution for protons from Xilinx [5] (black), as compared to the estimated cross-section for K^- (red) and K^+ (blue), estimated from the nuclear interaction cross-section ratio to protons.

5.1.3 Relative SEU cross-section contribution for various particle types in PISA model

Table 5.4 gives the relative cross-section contribution for various particle types in the PISA model for each position. One will observe that while protons contribute the smallest fraction of the cross-section in the near position, these become the chief source of SEUs in the far position. This can easily be explained by the combination of two factors: one, that the decays of kaons and pions significantly lowers the flux from such particles in the far position, coupled with the fact that the device now sits much farther away from the magnet irons, which serve as the chief source of neutrons incident upon the annular region.

Likewise, one will notice that pions alone vastly contribute to the SEU rate in the near position and still present a significant fraction of the SEU cross-section contribution in the far position. Given this, coupled with the relative lack of experimental data regarding the SEU cross-section contribution of pions, more study as to the contribution of pions to upset rates in SRAM-based devices would most certainly be warranted, especially if they are implemented for use with on-detector electronics.

As I shall show in a following section, such a radical shift in the SEU contribution from the loosely estimated cross-section of kaons, pions, and anti-protons to the better-known cross-sections of protons and neutrons ultimately has a significant impact upon the systematic error range between the two

Table 5.5 SEU statistics for events observed in experiment and predicted values from PISA. (Integrated luminosity values are measured in counts).

	Near ($r = 53$ cm)	Far ($r = 250$ cm)
Mean (observed)	52,862,652	520,110,588
Mean (aggregate)	72,347,356	875,353,200
Standard Deviation (σ)	18,838,151	464,923,378
Predicted	57,751,800	1,005,340,000

positions.

5.2 Comparison of observed SEU rates to predicted rates

In this section I shall present the calculated results for the SEU rates from the PISA model for the near and far positions and compare these to the observed results from the experiment.

Tables 5.5 gives a summary of both observed SEUs from experiment along with the observed mean (defined as the average integrated luminosity observed per SEU event), aggregated mean (defined as the total integrated luminosity divided by the number of SEU events), and the standard deviation of the observed mean, compared to the predicted SEU rates in PISA.

For purposes of statistics, the observed upset distribution was taken to follow a Poisson distribution. Given this form, the mean value of upsets was taken as the aggregate observed mean (i.e., the number of upsets over the total period of observation). Hence the sigma of such a distribution is taken as the square root of the mean (λ), i.e.:

$$\sigma^2 = \lambda \tag{5.6}$$

Thus for these purposes, the σ bounds define a 68% confidence interval, i.e., given the mean value λ , it is 68% likely that any new measurement would fall within the bounds of $\lambda \pm \sigma$. (Likewise, it is 95% likely that a value would fall within $\lambda \pm 2\sigma$).

As a measure of how well the observed data then compares to the model, the probability of the observed number of upsets occurring in bounds of the predictions is given from the Poisson distribution was calculated, where such a probability is given as:

$$p(y) = \frac{\lambda^y}{y!} e^{-\lambda} \tag{5.7}$$

Table 5.6 Statistical evaluation of upsets in the experiment and model. Given are the mean number of upsets over the measured interval for the experiment, from the model, the σ value from the Poisson distribution, and the probability of the experimentally observed number of upsets based upon the predicted values from the model.

	Near ($r = 53$ cm)	Far ($r = 250$ cm)
λ	3	3
σ	1.732	1.732
Predicted	3.758	2.612
$p(y = 3)$	0.2064	0.2180

In this particular case, λ was taken as the predicted mean, while the observed value (y) was taken from the observed data (e.g., 3 upsets). This then gives a probability of the observed mean value of upsets occurring, based upon the mean number of upsets predicted by the model.

For reference, the values of σ in addition to the predicted number of upsets over the observed interval, along with the probability of the observed number of upsets occurring based upon the model, are given in Table 5.6.

From Table 5.6, it should be noted that the experimentally observed number of upsets fall well within the sigma bounds of the PISA model, assuming a Poisson distribution form. Likewise, the probability of exactly three upsets occurring within the experimentally observed time period, based upon the predicted mean values of upsets, is approximately 21% and 22% respectively for the near and far positions, indicating a good agreement between the PISA model and experiment.

Based on these results, the PISA model can be used to make reasonably accurate predictions to the SEU rate to first order, so long as the tracking thresholds are modified within the detector and magnet media in the IR such that an accurate neutron flux can be estimated.

A caveat should be made for both cases however that the observed SEU rates were based off of very low statistics, due to the limitations of the experimental setup (as to minimize interference with other experiments in the detector) and the relative infrequency of upsets in the far position. For example, in over three weeks of constant exposure to beam products, only three SEU events were recorded in the far position - far greater than the average lifetime of a Au+Au fill and easily manageable if a rad-tolerant FPGA solution were put into place in this position with minimal use of SEU resistance strategies.

In as much, the “observed” SEU rates should be interpreted accordingly - with few data points, the trend is still subject to a high degree of statistical error. Thus deviations from this “observed” rate are in some respects estimated based upon estimates - what is useful in this case is their agreement to within

Table 5.7 Ratio of heavy ion production for individual particle type to that of protons, as compared to luminosity ratio by particle type scaled by average nuclear interaction cross-section ratio, $r = 53$ cm.

Type	$\frac{\text{lumin}_x}{\text{lumin}_p}$	$\left(\frac{\sigma_x}{\sigma_p}\right)$	$\left(\frac{\sigma_x}{\sigma_p}\right) \cdot \frac{\text{lumin}_x}{\text{lumin}_p}$	$\frac{\text{ions}_x}{\text{ions}_p}$
\bar{p}	0.0542436	1.15	0.0624	26
π^+	1.11127	0.657	0.730	8
π^-	1.12392	0.629	0.707	22
K^+	0.0857098	0.486	0.0417	0
K^-	0.077608	0.571	0.0443	0

an order of magnitude. Hence, such a model as the one proposed is primarily useful for estimating an approximate rate of expected upsets rather than pinpointing the exact device performance, which is beyond its capabilities.

Thus, the fact that the model can accurately estimate the predicted upset rate to within one sigma using only the Weibull curve for protons provided by Xilinx and the calculated Weibull curves for neutrons for both positions observed marks a resounding success, particularly given the fact as such upsets would come far more frequently in this position, thus requiring a more detailed study of the SEU mitigation strategies required. Likewise, as the dosages experienced by the device in the area dominated by collision particles are an order of magnitude greater (or more) than backgrounds, such a model also proves successful at estimating the average lifetime one could expect out of a rad-tolerant device placed in a region where collision products dominate the radiation dose.

5.3 Comparison of SEU cross-section contribution of various particle types to internal ion fragmentation

In this section, I shall analyze the assumption that the SEU cross-section contribution of various particle types scales in accordance with the ratio of the nuclear interaction cross-section to that of protons. The underlying assumption in this check shall be that the SEU rate is directly proportional to the generation of heavier, highly ionized particle fragments (such as α) within the Silicon lattice [3].

Thus, if the assumption is true that the SEU cross-section contribution of various particles scales approximately in accordance with the nuclear interaction cross-section, the production of heavy ion fragments inside the Silicon should scale roughly in accordance with the number of heavy fragments generated by protons, appropriately rescaled by the flux and interaction cross-section ratio.

Tables 5.7 and 5.8 give a breakdown of the particle production ratio as compared to protons, along

Table 5.8 Ratio of heavy ion production for individual particle type to that of protons, as compared to luminosity ratio by particle type scaled by average nuclear interaction cross-section ratio, $r = 250$ cm.

Type	$\frac{\text{lumin}_x}{\text{lumin}_p}$	$\left(\frac{\sigma_x}{\sigma_p}\right)$	$\left(\frac{\sigma_x}{\sigma_p}\right) \cdot \frac{\text{lumin}_x}{\text{lumin}_p}$	$\frac{\text{ions}_x}{\text{ions}_p}$
\bar{p}	0.00990505	1.15	0.00115	0
π^+	0.146133	0.657	0.0960	1
π^-	0.152262	0.629	0.0958	9
K^+	0.00948061	0.486	0.00461	0
K^-	0.00885384	0.571	0.00506	0

with the average nuclear interaction cross-section scaling factor and the ratio of heavy, highly ionized particles created in the Silicon (i.e., α and He^3 , with charge $q = +2$) as compared to protons. As one will observe, the ratio does not work out as neatly as expected - in fact no direct correlation appears to exist between the interaction cross-section scaling factor and the production of heavy ion fragments in the Silicon annulus. Rather, the production of such fragments seems to be much higher than the luminosity ratio (scaled by the interaction cross-section ratio) would lead one to believe.

This in and of itself is not necessarily a measure of the accuracy of the assumption used for Equation 4.2, namely due to the fact that the creation of heavy particle fragments inside the Silicon is just one of several ways that incident particles can result in the local ionization necessary to result in a state change within a bit.

Hence, to know the fractional contribution to the SEU rate caused by inelastic scattering (e.g., ion fragmentation) would require *a priori* knowledge of either the total SEU cross-section due to said particle types or of the “geometric” cross-section factor, neither of which is known. Thus the problem becomes an issue of one equation and two unknowns; without specific knowledge of the total cross-section by particle type (something which until this point has been only an assumed quantity), it is not possible to isolate the geometric cross-section factor directly, and thus not possible to use the ion fragmentation as a direct measure of the SEU contribution.

Given that the observed SEU rate is in fact an aggregation of *several* processes not limited only to inelastic scattering, it is reasonable to infer from Tables 5.7 and 5.8 that there may in fact be a variability in the the SEU cross-section contribution due to elastic and inelastic scattering between various particle types. This proves to be a perfectly valid assumption given the fact that the elastic and inelastic scattering cross-sections of protons are by no means isomorphic to those of other particles.

To obtain a more accurate picture of the local ionization processes that can lead to SEUs in PISA

would require a more sophisticated low-energy hadron simulation interface than GEANT provides. Specifically this would require a proper modeling of effects such as displacement of Silicon nuclei from their default lattice positions through elastic scattering of incident particles - a task that the most sophisticated models such as LANL's GNASH software are capable of (as it is specifically designed to model particle interaction cross-sections with specific materials such as Silicon), but are beyond the capabilities of the GEANT interface.

5.4 Evaluation of systematic errors within PISA model

In this section, I shall present an analysis of the sources of systematic error within the PISA model and their respective contributions to the total systematic error. For this, I shall consider the following sources: error introduced by the parameter minimization of the Weibull fit for neutrons, error introduced into the total SEU cross-section through the use of a scaling factor for the Weibull curve for particles of unknown cross section (as compared to a scaling factor of unity), and errors in the SEU cross-section due to variances in the total particle fluences, as compared to the values measured by the TLD badges.

The systematic error bounds from the choice of the Weibull fit form for neutrons was taken as the variance in the cross-section as compared to the choice of a linear form, giving a lower bound to the SEU cross-section contribution from neutrons. While Figure 5.2 would lead one to believe the error bound may be very large, it in fact only amounts to an error bound of approximately 8 to 14%.

To calculate the systematic error from particle fluences, the specific offset for the two neutron bins was taken into account for each of the two positions, given the fact that these fluences were a well-defined "known" quantity. Hence, this results in four actual correction factors - a "slow" neutron correction and a "fast" one for each of the two annular positions.

Additionally, the given Weibull fit parameters for the proton SEU cross-section distribution (and accordingly, that for pions, kaons, and anti-protons) was taken as the average experimentally observed data for the XQ2R1000 and XQ2R6000 devices. However, as is evident in Figure 2.5, the experimentally observed cross-section for the XQ2R6000 was on average 10-20% lower than the value of the fit parameters given. Hence, assuming an average over-estimation of 15% in the cross-section, this provides for a possible source of over-estimation in the predicted SEU cross-section for protons, as well as particles whose cross-section was calculated from the proton Weibull form (i.e., kaons, pions, and anti-protons).

Finally, the use of the scaling factor to the proton Weibull curve for particles whose SEU contributions were unknown provided a last source of systematic error. The bounds of this error were calculated by comparing the SEU cross-section contribution for each position to a scaling factor of unity.

Table 5.9 Tabulation of systematic errors in the predicted SEU cross-section for various aspects of the PISA model.

Source	% Systematic Error Contribution	
	Near ($r = 53$ cm)	Far ($r = 250$ cm)
Weibull form	-8.18	-14.7
“Fast” neutron flux	+4.14	-0.508
SEU scaling factor	+33.8010	+12.4455
Proton overestimate	-11.610	-10.445

Table 5.9 gives a breakdown of the sources of systematic error by position and their relative contributions to the total systematic error. One will notice that as expected, the Weibull fit minimization parameters provide the smallest contribution to the systematic error, given the quality of the fit to the available data. Likewise, the boundary of the “scaling” factor for pions, kaons, and anti-protons provides the largest source of systematic error, given the fact that the SEU contribution of such particles comprises the large majority of the SEU cross-section in the near position ($\approx 65\%$) and a significant minority in the far ($\approx 26\%$).

Likewise, as the cross-section profile of protons and neutrons is much better known than that of other particle types, it logically follows that the systematic error profile grows much smaller as the SEU cross-section contribution from such types composes a larger share of the total SEU cross-section.

5.5 Remaining sources of uncertainty

In this section I shall present any remaining sources of uncertainty inherent in the PISA model and avenues for possible remedy, where appropriate.

5.5.1 Contribution from thermal neutrons

Chief among the sources of uncertainty within the PISA model is the contribution from thermal neutrons, which is not appropriately accounted for within the model. This in turn may be a failure of the HIJING event generator to appropriately generate the slow neutrons generated as background radiation in the Au+Au collisions, however no way was found to properly cope with this deficit. It is assumed that given the fact that the dose from thermal neutrons was an order of magnitude smaller than the dose from other sources, this in turn would lead to thermal neutrons providing a second-order correction to the SEU rates and absorbed dosages. More likely however, it is simply a question of the tracking thresholds selected - were a truly accurate picture of thermal neutrons desired above all

else, these thresholds must be lowered even more than they were from their default settings in future simulations.

5.5.2 Uncertainties in particle generation within PISA

The use of the HIJING event generator brings with it additional uncertainties as well, including the accuracy of events generated as compared to the actual events observed within the PHENIX IR. While for the most part it is assumed that HIJING generates reasonably similar events to those observed in PHENIX, the difference in data sources between the experiment and simulation provides another source of uncertainty within the model.

Given the fact that the doses for γ show an average of $\approx 30\%$ variance, it would appear that between the tracking cuts and HIJING event generator, there is going to be some degree of inaccuracy inherent in the particle fluences, most likely due to the choice of tracking cutoff energies. This is especially evident for neutrons, where the variances prove to be much higher (although the doses still fall within the same order of magnitude). This variance may in turn have some impact upon the predicted SEU rate by underestimating the total particle flux upon the chip, and thus underestimating the total SEU cross-section.

5.5.3 Variances from the experimental geometry in the PISA model

One of the most significant possible sources of variance in the PISA model from the experimental results may stem from small variances in the PISA geometry from that of the experiment. The most notable example in this is in the Aluminum heatsink. While the heatsink layer is modeled as a solid layer, the actual layer contains a small $\approx 0.4466 \text{ cm}^2$ aperture at the center, effectively acting as a “window” to incoming particle flux.

Fortunately, the effect of this difference can be tested analytically: a small batch of approximately 5,000 events were simulated in the PISA software without the Aluminum layer from the heatsink itself. If such a layer has a substantial effect upon the cross-section, removing this layer should have a noticeable impact upon the calculated SEU cross-section (and hence the calculated SEU rate). Thus, if such an effect manifests, a correction factor can be applied by simply adding the cross-section of the exposed annulus, scaled by the fraction of the exposed area in the experimental setup.

However, as Table 5.10 demonstrates, the heatsink layer provides a but a minimal correction to the SEU cross-section. Given the fact that omitting the contribution of the Aluminum heatsink entirely does not noticeably impact the SEU rate, it thus can be concluded that any minor differences in the

Table 5.10 Comparison of SEU rate for the PISA simulation with and without the Aluminum heatsink layer.

Position	SEU Rate ($\frac{\text{events}}{\text{SEU}}$)	
	w/ heatsink	w/o heatsink
53 cm	57,751,800	58,524,400
250 cm	1,005,340,000	1,018,600,000

heatsink geometry from the experimental setup do not significantly contribute as a source of uncertainty to the predictions of the PISA model.

5.5.4 SEU cross-section scaling

The final source of uncertainty stems from the assumptions tested involving the SEU contribution of particle types other than protons and neutrons, for which the cross-sections were explicitly known from experiment. While using a scaling factor proportional to the nuclear interaction cross-sections appears to give results reasonably consistent with the experimental observations, it is nonetheless an assumption made mostly by inference from the results of the PISA model, rather than the ability to directly test the cross-sections of particles like pions directly. Future experiments to test the cross-section contribution of particles such as pions directly may prove that such a scaling factor may underestimate the cross-section contribution, making a particular difference when the flux is relatively low (i.e., farther from the collision point).

5.6 Areas for improvement within experiment

One of the most clear areas in which future experiments would benefit would be in the collection of a larger statistics pool. In this experiment, the very low SEU rate hindered the effective collection of statistics in the far position, indicating that an approach similar to that which Xilinx embraced in their Rosetta tests [3], (whereupon a board with 100 devices was exposed to atmospheric flux at various altitudes) would be more desirable. Unfortunately, such an approach may prove to be cost-prohibitive if taken to the same logical extreme, given the high cost of a single device, yet even a test with a fraction of the number of devices would provide better statistical resolution.

Likewise, the available data was highly limited for a position in the “near” location, namely because the experimental setup interfered with data collection by the larger PHENIX experiment. Hence, providing better statistics resolution the near position would require finding a way to mount a device

in the IR which minimizes interference while allowing for the device to be mounted, if such a task is possible.

In addition to this, an important aspect of improving the predictions of any model designed to predict the rate of bit upsets for on-detector electronics would involve gaining more information as to the SEU cross-section contribution of pions. Given the fact that it is estimated that such particles contribute heavily to the SEU cross-section in both the near and far positions (but most especially the near), creating a more accurate model for upsets would ultimately involve evaluating the cross-section contribution of pions in and of themselves. Obtaining experimental data for pion-induced upsets would greatly reduce the uncertainty from systematic errors in the model and possibly provide better resolution in terms of the predicted SEU rate, particularly in regions near the beam interaction point.

Finally, an additional means of gaining greater information about the actual ionizing energy dose on a given device in the IR would be to measure the total dose directly, including the dose left by charged particle tracks. While a dose can be estimated via PISA via the Bethe-Bloch formula, given the thermoluminescent materials on the TLD badge which screen out particles other than γ and β , the charged particle dose is largely unreported by badge. Thus with no reference to measure PISA charged particle predictions against, any prediction made by PISA would be at best an educated guess and little more.

However, based on prior experience with measuring the total ionizing energy dose (including that from charged particles), the solution appears to be in removing the thermoluminescent layer from the badge, thus allowing an “unscreened” dose from all types of radiation sources [29].

5.7 Summary

In this chapter, I have presented an overview of the means by which the SEU cross-section contribution was calculated for various particle types, specifically for neutrons, anti-protons, pions, and kaons. To this end, to calculate the SEU cross-section contribution for neutrons, a Weibull SEU cross-section distribution was estimated from the available data by Xilinx and iRoC. Meanwhile, the SEU rate for other particle species was detailed through the use of an energy-dependent “scaling factor” applied to the proton SEU curve, based upon the ratio of nuclear interaction cross-sections at the given energy.

Upon comparison with the experimental results, it was found that while the model was highly successful at predicting accurate upset rates to first order in both positions, as well as dosages in both positions (with the exception of those from thermal neutrons, which were nonetheless still calculated to within the correct order of magnitude).

Along these lines, I have also provided the relative SEU cross-section contributions as calculated by the model for the various particle types considered. What was found was that while protons compose only a small minority of the SEU cross-section contribution in the near position, they provide the greatest fraction of the dose in the far, with the contribution from particles such as kaons and pions providing the majority of the cross-section. This proves to be reversed in the far position, with protons providing the largest share of the SEU cross-section and the cross-section contribution of kaons and protons providing the least share of the dose. This in turn leads to a drastic shift in the systematic errors for the two positions: given the fact that the SEU cross-section from protons is a measured “known” and that of neutrons is well-estimated from measurements by Xilinx and iRoC, this results in a much greater share of the cross-section coming from well-known sources in the far position, lowering the systematic error profile.

Using the calculated particle fluences from the PISA model, I then proceeded to test the assumption that the SEU cross-section of non-protons scales directly with the ratio of the nuclear interaction cross-section of said particles with that of protons. If the production of heavy particle fragments in the Silicon (such as α) directly corresponds to the SEU rate, it should logically follow that if the SEU rate directly corresponds to the cross-section ratio, the heavy fragment production rate for non-protons should scale accordingly, when the particle flux is normalized to that of the proton flux. Under examination however, this did not prove to be the case.

This does not invalidate the cross-section scaling assumption - rather, given the fact that the SEU cross-section is an amalgamation of several processes which can create local ionization sufficient to create a change in state of bits within an device. For example, in addition to inelastic scattering which produces particle tracks within the Silicon, there also exists a cross-section contribution through Silicon nucleus “recoil” reactions from elastic particle scattering. Given that the inelastic and elastic scattering cross-sections for protons and other particles do not map isomorphically, it is quite possible that a variance in the expected internal ion creation stems from a difference in the ratio between the inelastic and elastic interaction cross-sections. Ergo, without concrete information regarding either the cross-section distribution for these particles or the “geometric” factor which gives the probability of an ionization resulting in a bit change, it is not possible to determine the fraction of the SEU cross-section due to heavier ion tracks being created inside the Silicon.

Finally, areas of uncertainty within the PISA model were examined, including uncertainties resulting from potential variances in the particle fluences from the HIJING event generator and from the experimental geometry used in PISA as compared to that used in the actual IR. To this end, potential

areas for improvement within future experiments were also presented.

Nonetheless, despite the particular limitations of such a model, it should be emphasized that such it still greatly succeeds at the stated goal of providing a scalable means of estimating the SEU rate with reasonable accuracy as a function of position within the PHENIX environment.

6 CONCLUSION

In this section, I shall present a summary of the result obtained from the analysis and experiment in terms of an “expected” SEU rate by taking the calculated and observed SEU rates based upon the RHIC I and RHIC II luminosity as a function of fill time. The means of estimating the RHIC I luminosity as a function of fill time will also be detailed.

The result of this shall be to give a practical “rate” estimate useful for estimating actual performance quality within the IR. Likewise, these luminosity estimates shall be used to give an order of magnitude estimate for doses from gammas and neutrons (as measured by the TLD badge) and charged particles, as estimated from the Bethe-Bloch formula.

6.1 Estimating SEU rates per fill from luminosity data

The prior results above give a prediction of the average number of events before an upset that one could expect, however this alone does not give a useful characterization of the failure rate of any given device. Thus, in order to predict the average rate of upsets that could be expected in a useful fashion, the number of events per fill as a function of time must be calculated.

To calculate a predicted upset rate for RHIC I fills, a series of fits to the ZDCLL1 luminosity data were carried out with a two-term exponential fit (Figure 6.1) with form:

$$ZDC_0 \cdot (\alpha \cdot e^{-t/\tau_{short}} + \beta \cdot e^{-t/\tau_{long}}) \quad (6.1)$$

Table 6.1 Fit parameters for the ZDC rate distribution as a function of time for fits with $\tilde{\chi}^2 < 2.5$.

Parameter	Value
τ_{short}	2,244.66 sec
τ_{long}	14,181.3 sec
α	0.446711
β	0.546705

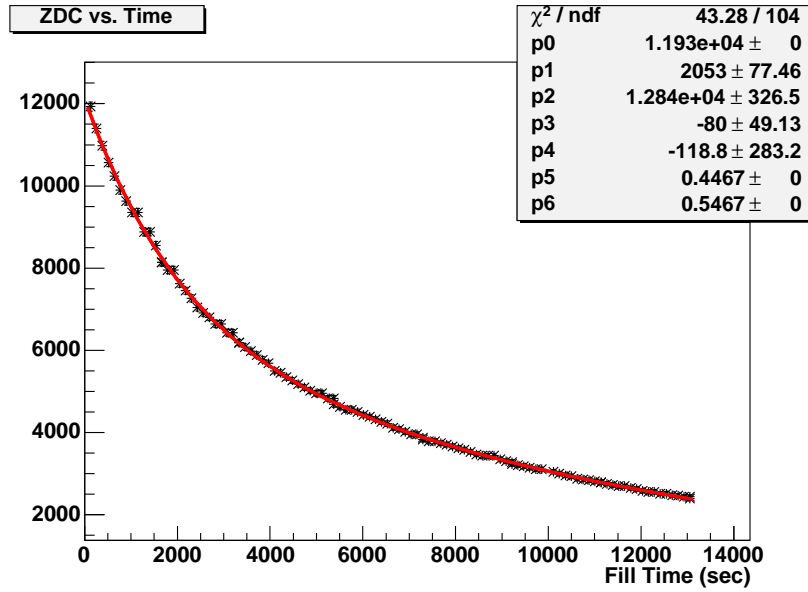


Figure 6.1 Sample fit to PHENIX ZDC data with two exponential terms ($\tilde{\chi}^2 = 0.4162$).

Such a fit was then integrated over time to obtain the average integrated luminosity per RHIC I fill. From this, the SEU probability as a function of time for an individual fill could be calculated.

The mean parameters for all fits to RHIC I luminosity data with $\tilde{\chi}^2 < 2.5$ are given in Table 6.1.

To give a mean number of SEUs per fill, the average number of events in one RHIC I fill was calculated given a maximum observed initial ZDC luminosity of 14 kHz with the above average estimated decay constants of a RHIC I fill (Figure 6.1). This number of events as a function of fill time was then scaled by the expected number of events per upset to yield a predicted SEU probability per fill as a function of fill time.

To calculate the SEU rate as a function of fill time for the proposed RHIC II upgrade, first an overview of the nature of the RHIC II upgrade is in order. RHIC II will have a design which will incorporate electron cooling along the accelerator to ensure a relatively constant ZDC rate once the beam reaches its peak luminosity. Such an improvement in beam luminosity and stability is achieved primarily by reducing the emittance of the beam through the intra-beam scattering of gold ions. This is achieved by scattering the beam ions off of electrons fired from an electron beam in a cooling solenoid. Such collisions of gold ions upon electrons reduce the random-motion energy of ions in the beam and thus enable a “compression” of the beam size, hence reducing emittance losses from intra-beam scattering and enabling much higher, more constant luminosities [12].

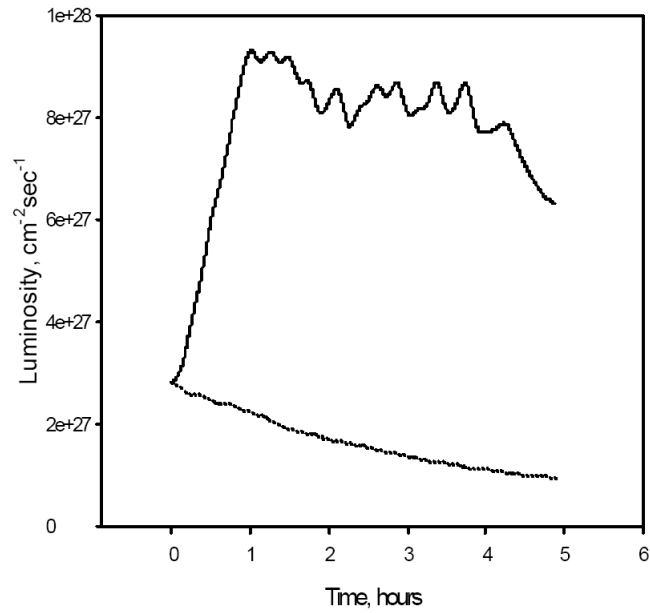


Figure 6.2 Comparison of RHIC fill luminosity as a function of fill time without electron cooling (lower), to RHIC fill luminosity with electron cooling (upper) [12].

To calculate the interaction rate of the RHIC II setup, the luminosity as a function of time (in units of $\frac{1}{\text{cm}^2 \cdot \text{s}}$) is multiplied by the nominal Au+Au cross-section (in units of cm^2) to give a rate in Hz.

Figure 6.2 show plots comparing luminosity with and without electron cooling on the RHIC accelerator. Thus, by taking the RHIC II luminosity (i.e., with electron cooling) projected in Figure 6.2 (top), the beam interaction rate as a function of time was calculated using a nominal Au+Au cross-section of $6.885 \cdot 10^{-24} \text{cm}^2$, giving a mean interaction rate of $\approx 60 \text{ kHz}$.

6.2 Comparison of predicted SEU rates as a function of fill time

As mentioned above, in order to characterize an average failure rate in a device due to neutron/anti-neutron interactions in a useful fashion, the observed upset rate in terms of integrated luminosity was folded into a distribution of the number of events per fill as a function of time. From this, one can obtain a mean number of SEUs per fill as a function of time for both RHIC I and RHIC II fills.

Figures 6.3-6.6 give a graphical representation of an expected SEU probability per bit as a function of fill time, based upon the data observed from both the model and actually testing at RHIC, extrapolated to a standard RHIC I and RHIC II fill with initial luminosities of 14 kHz and 50 kHz, respectively. For each figure is the mean observed SEU rate (solid black), the first standard deviation of the observed

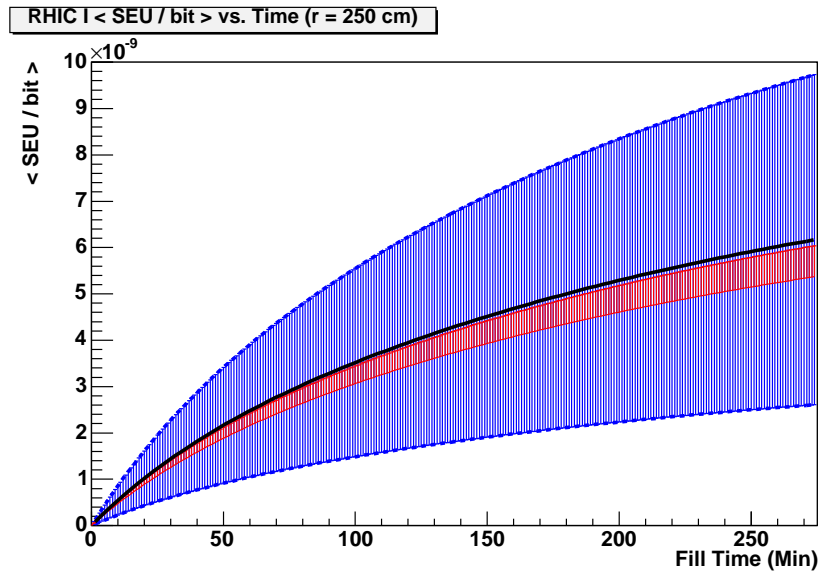


Figure 6.3 Mean SEUs per bit, per device as a function of fill time for Q-Pro Virtex II device in a RHIC I fill with initial luminosity of 14 KHz, far position ($r = 250$ cm). Black, solid: Mean (aggregate) Blue, filled: σ ; Red, filled: Predicted (with systematic errors).

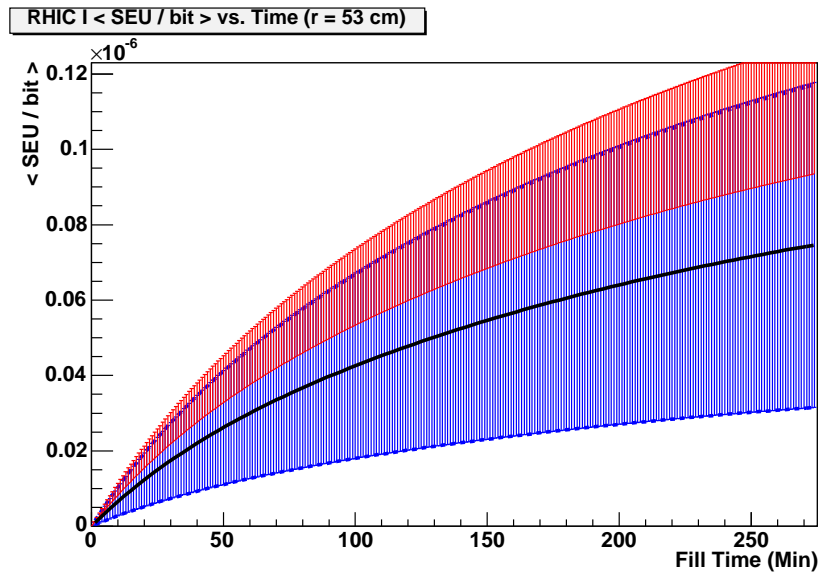


Figure 6.4 Mean SEUs per bit, per device as a function of fill time for Q-Pro Virtex II device in a RHIC I fill with initial luminosity of 14 kHz, near position ($r = 53$ cm). Black, solid: Mean (aggregate) Blue, filled: σ ; Red, filled: Predicted (with systematic errors).

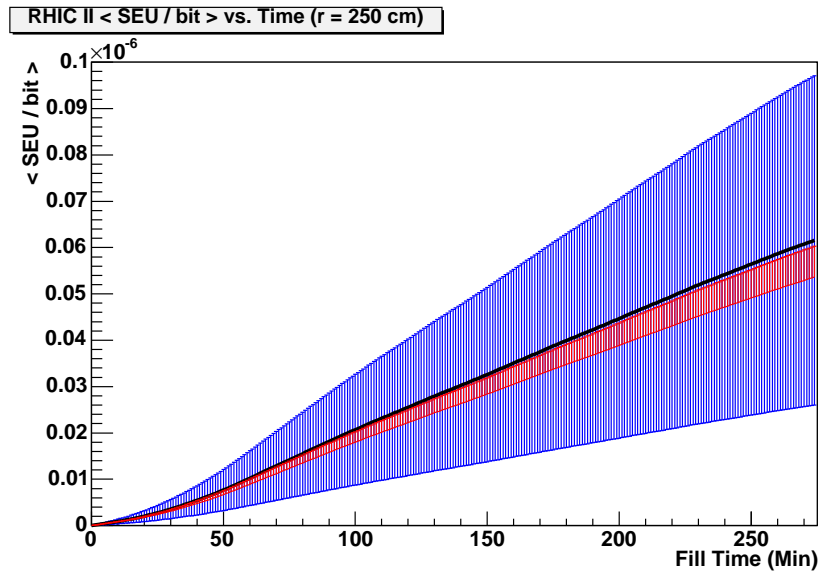


Figure 6.5 Mean SEUs per bit, per device as a function of fill time for Q-Pro Virtex II device in a RHIC II fill with a mean luminosity of ≈ 60 kHz, far position ($r = 250$ cm). Black, solid: Mean (aggregate) Blue, filled: σ ; Red, filled: Predicted (with systematic errors).

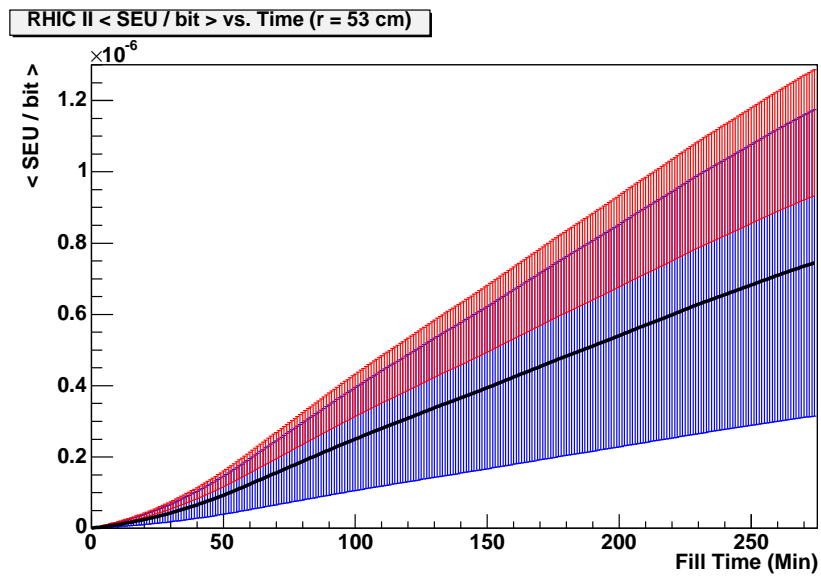


Figure 6.6 Mean SEUs per bit, per device as a function of fill time for Q-Pro Virtex II device in a RHIC II fill with a mean luminosity of ≈ 60 kHz, near position ($r = 53$ cm). Black, solid: Mean (aggregate) Blue, filled: σ ; Red, filled: Predicted (with systematic errors).

Aerospace & Defense FPGAs													
		Device	SMD	Core Voltage	Slices (1)	MULTs	BRAM bits	Configuration bits	Clock DLLs/DCMs	Max I/Os	Manufacturing Grades	Packages	Total Ionizing Dose (krad)
Defense QPRO FPGAs	QPro Virtex-II	XQ2V1000	5962-02529	1.5V	5,120	40	720K	3,987K	8	328	N	FG456, BG575 (6)	—
		XQ2V3000	5962-02530	1.5V	14,336	96	1,728K	10,248K	12	516	N, M, B	BG728, CG717 (2) (6)	—
		XQ2V6000	5962-02531	1.5V	33,792	144	2,592K	21,337K	12	824	M	CF1144 (3) (6)	—
	QPro Virtex-E	XQV600E	None	1.8V	6,912	—	288K	3,969K	8	316	N	BG432	—
		XQV1000E	None	1.8V	12,288	—	384K	6,433K	8	404	M, N	BG560, CG560 (4)	—
		XQV2000E	None	1.8V	19,200	—	640K	9,922K	8	804	N	BG560, FG1156	—
	QPro Virtex	XQV100	None	2.5V	1,200	—	40K	763K	4	180	M, N	PQ240, BG256, CB228 (5)	—
		XQV300	5962-99572	2.5V	3,072	—	64K	1,711K	4	316	M, N, B	PQ240, BG352, BG432, CB228	—
		XQV600	5962-99573	2.5V	6,912	—	96K	3,523K	4	316	M, N, B	HQ240, BG432, CB228	—
		XQV1000	5962-99574	2.5V	12,288	—	128K	5,084K	4	404	M, N, B	BG560, CG560	—
Aerospace QPRO-R Radiation Tolerant FPGAs	QPro-R Virtex-II	XQR2V1000	5962R02529	1.5V	5,120	40	720K	3,987K	8	328	R	FG456, BG575	200
		XQR2V3000	5962R02530	1.5V	14,336	96	1,728K	10,248K	12	516	R, M, V	BG728, CG717 (2)	200
		XQR2V6000	5962R02531	1.5V	33,792	144	2,592K	21,337K	12	824	H	CF1144 (3)	200
	QPro-R Virtex	XQVR300	5962R9957201	2.5V	3,072	—	64K	1,711K	4	162	M, V, B	CB228	100
		XQVR600	5962R9957301	2.5V	6,912	—	96K	3,523K	4	162	M, V, B	CB228	100
		XQVR1000	5962R9957401	2.5V	12,288	—	128K	5,084K	4	404	M, V, B	CG560 (4)	100

Figure 6.7 Table of Xilinx’s Q-Pro radiation-hardened line of FPGAs, including the maximum number of configuration logic bits available for designs and the maximum rated ionizing dose (kRads) [13].

Table 6.2 Mean SEUs per fill for the design under test with 16,394,483 configuration logic bits, assuming a 4-hour fill with a typical RHIC I and RHIC II luminosity profile.

	$\langle \text{SEU/ Fill} \rangle$	
	RHIC I	RHIC II
r = 53 cm	1.1505	10.732
r = 250 cm	0.09509	0.88696

data (dashed blue lines), and the predicted rate by PISA (dashed red).

To provide a concrete picture of the average SEU rate in a fill, the observed mean SEU rate was taken with the integrated luminosities from RHIC I and RHIC II to provide an mean number of SEUs per fill. Table 6.2 gives a mean number of SEUs per fill for RHIC I and RHIC II luminosity profiles, assuming an average fill time of 4 hours with the design used in the test, which utilized 16,394,483 configuration logic bits. One will observe that given the expected improvements in the RHIC II luminosity profile, the mean SEU rate increases by nearly an order of magnitude, thus making SEU mitigation a vital concern in SRAM-based devices, particularly as one locates such devices closer to the beam interaction area.

Figure 6.7 gives a listing of Xilinx’s radiation-hardened line of FPGAs, including the maximum amount of configuration bits available for user designs and the rated total ionizing energy dose, in kRad. The expected amount of upsets per fill can easily be determined for a particular device by scaling the curves provided in Figures 6.3-6.6 by the number of configuration bits in the device to be used, scaled by the expected occupancy.

6.3 Probability of concurrent TMR failure

In this section, I shall present a sample combinatoric exercise under which the probability of a concurrent TMR failure in two or more modules results in a total device failure for a sample design. For purposes of this exercise, the sample design shall be the ALICE1 pixel pilot design implemented by Jonathan Crandall, which used a rudimentary degree of TMR implemented manually in each of the three logical units [14].

First, the probability of a failure in a single triplicated logical unit is given by the following combinatoric:

$$P_{\text{TMR}} = \frac{1}{N^2} \cdot \frac{1}{3!} \cdot (P_{\text{SEU}})^2 \quad (6.2)$$

where $(P_{\text{SEU}})^2$ is the probability of an individual SEU within a bit in a logical device, given by:

$$P_{\text{SEU}} = \sigma_{\text{SEU}} \cdot N_{\text{coll}} \cdot \left(\frac{N_{\text{bits}}}{3} \right) \quad (6.3)$$

where σ is the SEU cross-section per bit, per collision, N_{coll} is the number of collisions, and N_{bits} represents the number of bits in each “logical section.” Given the fact that the total number of bits can be represented as $N_{\text{bits}} \cdot N$, this probability can thus be rewritten as:

$$P_{\text{SEU}} = \sigma_{\text{SEU}} \cdot N_{\text{coll}} \cdot \left(\frac{N_{\text{tot-bits}}}{3 \cdot N} \right) \quad (6.4)$$

Given that N logical devices exist within a single device and that each logical unit consists of three TMR sub-units, the final probability of a concurrent TMR failure becomes:

$$P_{\text{device}} = \frac{1}{N} \cdot \frac{1}{2} \cdot (P_{\text{SEU}})^2 \quad (6.5)$$

Table 6.3 gives the probability of a concurrent failure for the design tested in the PHENIX IR. Note that this relies on the assumption of a worst-case scenario regarding SEUs, namely that each SEU occurs within a *used* configuration logic cell. Yet as testing by Xilinx has shown, most typical designs

Table 6.3 Probability of a concurrent TMR failure for the design under test with 16,394,483 configuration logic bits, assuming a 4-hour fill with a typical RHIC I and RHIC II luminosity profile.

	RHIC I	RHIC II
r = 53 cm	2.7236E-3	2.0576E-1
r = 250 cm	1.8605E-5	1.6187E-3

Table 6.4 Doses from charged particles (calculated from PISA) and from gammas and neutrons as measured by attached TLD badges, converted to radiation-absorbed dose per event (rad/event).

	Charged (PISA)	Deep	Slow Neut.	Fast Neut.
r = 53 cm	9.05044E-9	8.11621E-10	6.95177E-12	2.87624E-10
r = 250 cm	1.91629E-9	5.22249E-11	3.54990E-12	1.95074E-11

only actually occupy 1 in 10 to 1 in 40 configuration logic cells - meaning that SEUs in these units do not cause any actual problems in the user interface whatsoever. Hence, a conservative factor of 10 can be applied to the actual SEU rate, and accordingly to the probability of a concurrent failure [7].

Likewise, such a probability makes no account of other applied mitigation techniques such as active reconfiguration (also known as “scrubbing”), which would drastically lower the observed failure rate in any given device.

6.4 Estimating per-fill dose rates

Using the prior estimated luminosity data, the per-fill dose rate can be estimated for a typical fill profile. Such a rate shall be estimated from two sources - the dose rate for gammas and neutrons as observed by the attached TLD badges, using the appropriate quality factor conversion from a human-equivalent dose in rem to a radiation-absorbed dose in rad. In addition to these sources, the radiation dose of charged particles (with fluences estimated from the HIJING event generator) shall be tabulated using the Bethe-Bloch formula¹, giving a typical per-fill rate for an average RHIC I and RHIC II fill.

Table 6.4 gives the calculated dose rate per event in rad for charged particles from the PISA model, in addition to the converted “deep” gamma dose, “slow” and “fast” neutron doses. A caveat should be made that the charged doses are given without reference data; i.e., the features of the attached TLD badge screened out most non-beta charged particles, leaving no data to reference data to compare the

¹See Appendix A for further discussion of the Bethe-Bloch formula and its application in calculating ionizing energy loss for charged particles.

Table 6.5 Mean total ionizing dose (TID) for RHIC I and RHIC II fills, for both near and far positions (rad/fill).

$\langle \text{TID} / \text{Fill} \rangle$		
	RHIC I	RHIC II
r = 53 cm	0.79490	7.88568
r = 250 cm	0.16783	1.54627

calculated charged particle dose to. It is simply assumed that based upon the fact that HIJING appears to give reasonable particle fluence estimates for neutrons and gammas that a similar principle is true for charged particles. Absent from this calculation however is the contribution of “beam scrape” losses to the charged particle dose, which would undoubtedly manifest a greater contribution to the charged dose nearer to the beam interaction point.

Table 6.5 shows the per-fill dose for RHIC I and RHIC II fills in each of the two positions tested. One will observe that with the expected luminosity improvements in RHIC II, this results in doses approximately five times greater than those observed in RHIC I fills. Nonetheless, the estimated doses from beam and background products appear to be very reasonable, giving plausible device lifetimes that can conceivably survive throughout the entire RHIC experiment.

However, what should be emphasized nonetheless is that these dose estimates neglect the contribution of beams scrape losses, which are likely to be much greater than doses from collision products and secondaries. Thus to provide actual estimates of an expected device lifetime in the interaction region, more study as to the total charged particle doses (including that of beam scrape losses) is needed.

6.5 Summary

In this chapter, I have presented a useful means of characterizing device performance from the calculated and observed SEU rates by profiling the average fill luminosity as a function of time for RHIC I and RHIC II fills. This result can be expressed both as a time-dependent SEU rate and as a per-fill mean SEU rate. In addition, I have applied these methods to the estimated radiation-absorbed doses, calculated for charged particles from the PISA model and from the TLD badges, where the doses were converted from human-equivalent form (rem) to units of radiation absorbed dose (rad).

APPENDIX A CALCULATION OF MINIMUM-Z FOR THRESHOLD $\frac{dE}{dx}$ USING THE BETHE-BLOCH FORMULA

Overview of Bethe-Bloch formula

The Bethe-Bloch formula[19] gives the linear energy transport of a charged particle through a medium per unit length (i.e., as a function of distance traveled through the medium), expressed more succinctly as $\frac{dE}{dx}$. The Bethe-Bloch formula is as follows:

$$-\frac{dE}{dx} = 2\pi N_a r_e^2 m_e c^2 \rho \frac{Z}{A} \frac{z^2}{\beta^2} \left[\ln \left(\frac{2m_e \gamma^2 v^2 W_{max}}{I^2} \right) - 2\beta^2 - \delta - 2\frac{C}{Z} \right] \quad (\text{A.1})$$

Where N_a is Avogadro's number ($6.022 \cdot 10^{23} \text{ mol}^{-1}$), r_e is the classical electron radius ($r_e = 2.817 \cdot 10^{-13} \text{ cm}$), m_e is the electron mass, ρ is the density of the absorbing material, Z is the atomic number of the absorbing material, A is the atomic weight of the absorber, z is the charge of the incident particle in units of the electron charge e , $\beta = \frac{v}{c}$ for the incident particle, $\gamma = \frac{1}{\sqrt{1-\beta^2}}$, I is the mean excitation potential (173 eV for Silicon), δ is the density correction (to be defined shortly), C is the shell correction (also to be defined shortly), and W_{max} is the maximum energy transfer for a single collision.

Defining $\eta = \gamma\beta$, maximum energy transfer per collision W_{max} is defined as:

$$W_{max} = \frac{2m_e c^2 \eta^2}{1 + \frac{m_e}{M_{part}} \sqrt{1 + \eta^2 + \left(\frac{m_e}{M_{part}}\right)^2}} \quad (\text{A.2})$$

This then simplifies to $W_{max} \approx 2m_e c^2 \eta^2$ for $M_{part} \gg m_e$.

Likewise, using the simplified form of W_{max} and $2\pi N_a r_e^2 m_e c^2 = 1.535 \cdot 10^{-4} \frac{\text{MeV} \cdot \text{cm}^2}{\text{mg}}$, A.1 can be reduced to the following:

$$-\frac{dE}{dx} = 1.535 \cdot 10^{-4} \rho \cdot \frac{Z}{A} \cdot \frac{z^2}{\beta^2} \left[\ln \left(\frac{(2m_e \gamma \eta)^2}{I^2} \right) - 2\beta^2 - \delta - 2\frac{C}{Z} \right] \quad (\text{A.3})$$

Shell Correction

For incident particles of very low energy, the fundamental assumption that the bound electron is essentially at rest compared to the velocity of the particle no longer holds, thus prompting a small correction to the Bethe-Bloch formula for very low energies[19]. While a full treatment will not be given here, the empirically-derived formula for the shell correction is as follows:

$$C(I, \eta) = (0.422377 \cdot \eta^{-2} - 0.0304043 \cdot \eta^{-4} - 0.00038106 \cdot \eta^{-6}) \cdot 10^{-6} \cdot I^2 \quad (\text{A.4})$$

$$+ (3.850190 \cdot \eta^{-2} - 0.1667989 \cdot \eta^{-4} + 0.00157955 \cdot \eta^{-6}) \cdot 10^{-9} \cdot I^3$$

The above expression is valid for $\eta \geq 0.1$ [19].

Density Correction

One correction to the Bethe-Bloch formula arises from the fact that the polarization by incident particles tends to shield electrons removed from the path of the incident particle from the full intensity of the electric field [19]. Such an effect naturally depends on the density of the material, given the fact that the polarization will be greater in denser materials than in less dense ones. Thus, the shell correction lowers the effective $\frac{dE}{dx}$ at higher particle energies, expressed as:

$$\delta = \begin{cases} 0 & X < X_0 \\ 4.6052 \cdot X + C_0 + a(X_1 - X)^m & X_0 < X < X_1 \\ 4.6052 \cdot X + C_0 & X > X_1 \end{cases} \quad (\text{A.5})$$

where $X = \log_1 0(\gamma\beta)$ and for Silicon: $C_0 = -4.44$, $a = 0.1492$, $m = 3.25$, $X_1 = 2.87$, and $X_0 = 0.2014$.

Calculating minimum Z for threshold $\frac{dE}{dx}$

To calculate the minimum Z required for the threshold $\frac{dE}{dx}$, all that needs to be done is to insert the given $\frac{dE}{dx}$ into the left side of A.3 (canceling the density terms, as the $\frac{dE}{dx}$ is given in units of $\frac{\text{MeV}\cdot\text{cm}^2}{\text{mg}}$). Next, substituting in the appropriate properties of Silicon, one can solve for the charge of the incident particle z for various values of β , yielding the following table (A.1) for the Q-Pro and Actel series designs:

As one can easily observe, a latchup condition can only be caused by direct exposure to slower heavy ions. While this is a practical concern for space applications, for on-detector electronics this would only

Table A.1 Minimum Z required to achieve LET_{th} as a function of β for Xilinx Q-Pro and comparable Actel series of rad-hardened FPGAs.

β	Min. Z	
	Xilinx	Actel
0.10	44	32
0.20	75	55
0.30	105	76
0.40	133	97
0.50	161	116
0.60	186	135
0.70	211	153
0.80	232	168
0.90	250	181
0.96	254	184

be realized in the worst-case scenario of direct exposure to the heavy ion beam, or in the case of a beam configuration which utilizes collisions between singly charged particles and heavy ions, thus producing heavy ion secondaries.

APPENDIX B DETAILS OF MONTE CARLO CALCULATIONS

In order to plan for the experiment described in this thesis, a simple Monte Carlo model was constructed based upon the assumption that neutron/anti-neutron yield has a 1:1 correlation with proton/anti-proton yield, which is known as a function of rapidity. Likewise, it was assumed for the sake of simplicity that all charged particles were pions, having the same cross-section as protons (an assumption which would later be refined in the more sophisticated PISA model).

Unlike the PISA model, the simple Monte Carlo's purpose was to provide a rough order-of-magnitude estimate of the SEU rate which could be expected in the detector environment. Hence it proved to be much more limited in scope than the PISA model, neglecting second-order contributions from effects such as background radiation and interactions with detector components.

Following the experiment, a second model was constructed using PISA, which not only characterized background effects neglected within the Monte Carlo, but also refined assumptions such as that of the particle distributions and the SEU cross-sections of charged particles other than protons.

Yields for charged particles and neutrons/anti-neutrons

The distribution of charged particles as a function of pseudorapidity was calculated by the PHOBOS collaboration's 0-50% data (taken as minimum bias) [30]. Given that the highest centrality class data available at the time for charged particles went only up to 50%, it was assumed that all centralities above 50% followed approximately the same distribution as the 40-50% centrality class distribution, completing the approximation of minimum bias data, albeit an overestimation.

For the sake of simplicity, all charged particles were assumed to be pions (these being the predominant charged particles created). For each event, a randomly generated centrality class was thrown, which then corresponded to a charged particle distribution for that centrality bin. The number of charged particles N_{ch} was thus calculated by taking the integral over the given pseudorapidity distribution for the appropriate centrality distribution.

By contrast, to calculate the yields of neutrons and anti-neutrons, the assumption was made that

neutron/anti-neutron yields scale in a 1:1 manner with proton/anti-proton yields. For these yields, N_{part} was calculated from the integral of the BRAHMS collaboration's 0-10% data[31], scaled then for the appropriate centrality class using the corresponding Glauber calculations [32] (where $|N_{Glauber}|_{cent=x}$ corresponds to N_{part} for the appropriate centrality bin), i.e.:

$$N_{part} = \frac{|N_{Glauber}|_{cent=x} \cdot \int \frac{dN_{ch}}{dy} dy}{|N_{Glauber}|_{cent=0}} \quad (\text{B.1})$$

For both cases, all that is required from this point to generate a Monte Carlo event is a randomly generated collision vertex (taken as a Gaussian with $\sigma = 30$ cm), the corresponding $\frac{dN}{d\eta}$ distribution for the centrality class (or $\frac{dN}{dy}$ neutrons/anti-neutrons) from which the rapidity/pseudorapidity of thrown particles are randomly sampled, and mean transverse momentum ($\langle p_{\perp} \rangle$, taken to be 350 MeV in both cases).

Event generation

For each event, the first randomly generated properties are the event centrality and the collision vertex. From the event centrality, the number of neutrons/anti-neutrons generated from the event is calculated by scaling the number of neutrons/anti-neutrons per event based upon BRAHMS 0-10% numbers [31], then scaling these numbers by the corresponding Glauber calculation for the centrality class [32].

The collision vertex (which will be referred to as z_0 from here on out) for the event is randomly generated from a Gaussian with $\sigma = 30$ cm. This is then used with the particle kinematics to determine if a collision occurred upon the annular region surrounding $z = 0$ cm.

Neutron/anti-neutron kinematics

For each particle, a rapidity and transverse momentum are thrown from their corresponding distributions. With the collision vertex, it is then possible to determine whether the neutron/anti-neutron intersects an annular region of radius 21.0 cm or 250.0 cm and width 1.2 cm, centered about $z = 0$ cm, and from this, calculate the contribution to the SEU cross-section from its kinetic energy.

The rapidity distribution was calculated as a Woods-Saxon fit to BRAHMS data [31], given as the following for neutrons and anti-neutrons, respectively:

$$\frac{dN_n}{dy} = \frac{28.5869}{1 + e^{\frac{|y|-4.56231}{1.12167}}} \quad (\text{B.2})$$

$$\frac{dN_{\bar{n}}}{dy} = \frac{20.6120}{1 + e^{\frac{|y|-2.66227}{.357470}}} \quad (\text{B.3})$$

From these functions, a unique rapidity for each particle generated was randomly thrown. Likewise, these functions were integrated from the rapidity bounds of -5.36 to 5.36 and scaled by the appropriate N_{part} for their centrality class per the Glauber calculations to give a number of N_{part_n} and $N_{part_{\bar{n}}}$ for each event.

From the rapidity, the longitudinal momentum p_z was calculated as

$$p_z = m_{neut} \cdot \sinh(y) \quad (\text{B.4})$$

as $\sinh(y) = \gamma\beta$ [33], and m_{neut} is in $\frac{MeV}{c^2}$.

Likewise, the transverse momentum was thrown from a distribution of the form:

$$P(p_{\perp}) = p_{\perp} e^{p_{\perp}/350} \quad (\text{B.5})$$

where p_{\perp} is in MeV.

To determine whether an intersection occurs is a question of simple trigonometry - if one considers dimensions Δr and Δz to form two legs of a triangle, it would form a similar triangle as momentum components p_{\perp} and p_z :

$$\tan \theta = \frac{p_{\perp}}{p_z} = \frac{\Delta r}{\Delta z} \quad (\text{B.6})$$

Thus the total z-displacement would be:

$$\Delta z = z_0 + \frac{p_z}{p_{\perp}} \cdot r_0 \quad (\text{B.7})$$

where z_0 is the randomly thrown collision vertex and r_0 is the radius of the annular region. If $|\Delta z| < .6$, the particle ‘‘intersects’’ the annular region when it reaches r_0 and thus the SEU cross-section contribution is calculated.

Charged particle kinematics

The procedure for obtaining basic charged particle properties such as p_z and p_{\perp} is identical to that as carried out in equations (B.4) and (B.5). Unlike neutral particles however, the motion of charged particles is largely determined by the presence of the magnetic field, taken to be 10 kGauss per Run4

conditions. From this, two factors determine whether an intersection with the annular region: the particle gyration radius and the interval of intersection, both of which will be discussed below.

Particle Gyration Radius

Charged particles in a magnetic field will not follow a straight path like neutral particle, but rather a helical path. Thus their gyration radius [3] is:

$$p_{\perp} \cdot c = q \cdot B \cdot r \quad (\text{B.8})$$

$$p_{\perp} = 3.00 \cdot 10^{-4} \cdot B \cdot r \quad (\text{B.9})$$

where pT is measured in MeV, r in cm, and B is measured in Gauss.

Interval of Intersection

Since not every particle will hit the annular region (in fact, only a fraction of a percentage will), one must stipulate the conditions under which a particle will intersect with the chip, thus depositing energy and contributing to the upset cross-section. In the following equations, R_B represents the particle gyration radius while r_0 is the distance to the silicon layer in question, and n is any integer, while the cyclotron frequency ω is given by the following [33]:

$$\omega = \frac{q_e \cdot B}{\gamma \cdot m \cdot c} \quad (\text{B.10})$$

The position vector of the incident particle can be taken as:

$$\begin{aligned} p_x &= m \cdot \omega \cdot R_B \cdot (\cos(\omega t + \phi)) \\ p_y &= m \cdot \omega \cdot R_B \cdot (\sin(\omega t + \phi)) \end{aligned} \quad (\text{B.11})$$

From this, one can find the x and y components of the transverse momentum vector p_{\perp} :

$$\begin{aligned} p_x &= R_B \cdot (\cos(\omega t + \Phi) + 1) \\ p_y &= R_B \cdot \sin(\omega t + \Phi) \end{aligned} \quad (\text{B.12})$$

The coordinates of the annular region can be expressed as the following:

$$\begin{aligned} r_x &= r_0 \cdot \cos(\phi) \\ r_y &= r_0 \cdot \sin(\phi) \end{aligned} \quad (\text{B.13})$$

Thus the point of intersection occurs when:

$$\begin{aligned} a_x &= r_x \\ a_y &= r_y \end{aligned} \tag{B.14}$$

Then solving for the system of equations:

$$\begin{aligned} r_0^2 \cdot \cos^2(\phi) &= R_B^2 \cdot (\cos(\omega t + \Phi) + 1)^2 \\ &= R_B^2 \cdot (\cos^2(\omega t + \Phi) + 2 \cdot \cos(\omega t + \Phi) + 1) \\ &= R_B^2 \cdot (2 \cos(\omega t + \Phi) + 2 - \sin^2(\omega t + \Phi)) \\ &= 2 \cdot R_B^2 \cdot (\cos(\omega t + \Phi) + 1) - r_0^2 \cdot \sin^2(\phi) \end{aligned} \tag{B.15}$$

Thus yielding:

$$\omega t + \Phi + 2\pi \cdot n = \arccos\left(\frac{1}{2} \left(\frac{r_0}{R_B}\right)^2 - 1\right) \tag{B.16}$$

From inspection, one will notice this only yields solutions for $R_B \geq \frac{r_0}{2}$.

The interval of intersection is determined by three parameters: t_0 , the time at which the particle reaches the threshold of the annular region and Δt , the time in which it takes the particle to cross the plane of the chip and z_0 , the interaction vertex. The time interval is solved for by taking the distanced traveled by the particle, divided by the transverse momentum and multiplied by the particle mass. The sign of the transverse momentum p_z plays an important in determining whether a particle is incident upon the annular region - if a given particle's interaction vertex is z_0 is beyond the annular region (centered about $z = 0$) and the product of the interaction vertex and transverse momentum is positive, the particle is moving away from the annulus, thus it will not hit.

Thus t_0 is the time required for the particle to travel between the collision vertex and the edge of the annular region, while Δt is the time required to cross the distance of the annular region, giving:

$$t_0 = \frac{\gamma \cdot M_{part} \cdot (|z_0| - 1.25) \cdot 10^{-2}}{p_z} \tag{B.17}$$

$$\Delta t = \frac{\gamma \cdot M_{part} \cdot 2.5 \cdot 10^{-2}}{p_z} \tag{B.18}$$

(Note the conversion factor in Equations B.17 and B.18 due to the implicit factor of c (taken as unity), where M_{part} is in units of $\frac{\text{MeV}}{c^2}$ and p_z is in units of $\frac{\text{MeV}}{c}$. Thus, one must convert from units of m to cm).

Table B.1 SEU rate predictions from 10,000 events in the simple Monte Carlo for the two annular positions.

Position	Events per SEU
$r = 53$ cm	2.32976E+8
$r = 250$ cm	3.97433E+9

The particle must intersect the annular region in this interval for a collision to take place, giving rise to the following inequality:

$$\begin{aligned}
 t_0 &\leq t_{hit} \leq \Delta t + t_0 \\
 \omega t_0 &\leq \omega t_{hit} \leq \omega \Delta t + \omega t_0 \\
 0 &\leq \left(\frac{1}{2} \left(\frac{r_0}{R_B} \right)^2 - 1 \right) - \Phi - \omega t_0 \leq \omega \Delta t
 \end{aligned} \tag{B.19}$$

SEU cross-section contribution

Once a particle has been determined to have intersected the annular region, its SEU cross-section contribution can be determined using known, empirically derived functions for the SEU cross-section as a function of the incident particle's kinetic energy[20]:

$$P_{SEU}(T) = 3.8 \cdot 10^{-14} \cdot \left(1 - e^{-\left(\frac{T-3}{2.4}\right)} \right) \tag{B.20}$$

where T is the kinetic energy of the incident particle in MeV, calculated as:

$$T = c \cdot \sqrt{(p_{\perp}^2 + p_z^2) + m_{part}^2 \cdot c^2} - m_{part} \cdot c^2 \tag{B.21}$$

The result of equation B.20 is in units of $\frac{\text{SEU}}{\text{event} \cdot \text{bit} \cdot \text{cm}^2}$ and is thus scaled accordingly by the number of configuration logic bits in the device (obtained from FIVIT), the number of events generated, and the area of the chip.

Table B.1 gives the results from 10,000 events generated by the Monte Carlo. As one will notice, the predictions are of significantly poorer quality than those predicted by the PISA model (with the predictions consistently off by a factor of $\approx 4 - 5$), namely due to lack of sophistication in such a model. In particular, the Monte Carlo model completely neglects effects which dominate the radiation dose, such as neutrons generated in background materials such as the magnet media. Nonetheless, it still remained useful in the early stages of the experiment for providing a simple order-of-magnitude

estimate, motivating the actual experiment conducted at PHENIX and the more sophisticated PISA model.

BIBLIOGRAPHY

- [1] James E. Martin. *Physics for Radiation Protection*. John Wiley and Sons, New York, 2000.
- [2] Marcos Olmos. Radiation results of the SER test of Actel, Xilinx and Altera FPGA instances. Technical report, iRoC Technologies, 2003. <http://www.actel.com/documents/RadResultsIROCreport.pdf>, (Obtained: February, 2005).
- [3] Joseph J. Fabula and Austin Lesea. The NSEU response of static latch based FPGAs. In *MAPLD 2003*, Washington, D.C., September 2003. Military and Aerospace Programmable Logic Devices International Conference. Paper C5.
- [4] S. A. Wender B. Takala. Accelerated neutron testing of semiconductor devices, August 2001. <http://wnr.lanl.gov/see/poster.pdf>, (Obtained: March 2005).
- [5] Single Event Effects Consortium. Xilinx single event effects consortium report: Virtex II static SEU characterization. Technical report, Single Event Effects Consortium, 2003.
- [6] P. Graham, M. Caffrey, J. Zimmerman, and D. Eric Johnson. SEE and TID extension testing of the Xilinx XQR18V04 4Mbit radiation hardened configuration PROM. In *MAPLD 2002*, Laurel, USA, September 2002. Military and Aerospace Programmable Logic Devices International Conference. Paper C6.
- [7] Xilinx. Radiation effects and mitigation overview. <http://www.xilinx.com/products/milaero/MilAero.pdf>. (Obtained: October, 2004).
- [8] M. Caffrey, P. Graham, E. Johnson, M. Wirthlin, and C. Carmichael. Single-event upsets in SRAM FPGAs. In *MAPLD 2002*, Laurel, USA, September 2004. Military and Aerospace Programmable Logic Devices International Conference. Paper P8.
- [9] K. Hirose et al. SEU resistance in advanced SOI-SRAMs fabricated by commercial technology using a rad-hard circuit design. *IEEE Transactions on Nuclear Science*, 49(6), 2002.

- [10] J.J. Wang. Total ionizing test report. Technical Report 04T-RTSX32S(U)-D110A1, Actel, 2004. [http://www.actel.com/documents/04T-RT54SX32S\(U\)-D110A1.pdf](http://www.actel.com/documents/04T-RT54SX32S(U)-D110A1.pdf), (Obtained: October, 2004).
- [11] U.S. Government. *Code of Federal Regulations, Title 10*, volume 4, chapter III. U.S. Government Printing Office, January 2004. Chapter 835: Occupational Radiation Protection.
- [12] T. Hallman, T. Kirk, BNL T. Roser, and R.G. Milner. RHIC II/eRHIC white paper. Technical report, RHIC Planning Group for Luminosity Upgrades, February 2003. http://www.bnl.gov/henp/docs/NSAC_RHICII-eRHIC_2-15-03.pdf, (Obtained: March 2005).
- [13] Xilinx. Defense and aerospace product catalog. http://www.xilinx.com/publications/matrix/hire1_color.pdf, (Obtained: March 2005).
- [14] J. Crandall et al. VHDL digital pilot model for ALICE1 pixel chip readout. (unpublished), 2004.
- [15] C. Carmichael, E. Fuller, P. Blain, and M. Caffrey. SEU mitigation techniques for virtex FPGAs in space applications. In *MAPLD'99*, Laurel, USA, September 1999. Military and Aerospace Programmable Logic Devices International Conference.
- [16] Xilinx. *QPro Virtex-II 1.5V Radiation Hardened QML Platform FPGAs*, v1.1 edition, January 2004. <http://direct.xilinx.com/bvdocs/publications/ds124.pdf>, (Obtained: October, 2004).
- [17] Actel. *RTAX-S RadTolerant FPGAs*, v0.5 edition, May 2004. <http://www.actel.com/documents/RTAXSDS.pdf>, (Obtained: October, 2004).
- [18] Actel. Radiation performance of Actel products, version 9, March 2004. <http://www.actel.com/documents/RadiationPerformance.pdf>, (Obtained: October 2004).
- [19] W.R. Leo. *Techniques for Nuclear and Particle Physics Experiments*. Springer-Verlag, New York, second edition, 1994.
- [20] K. Johansson, P. Dyreklev, B. Granbom, N. Olsson, J. Blomgren, and P. Renberg. Energy-resolved neutron SEU measurements from 22 to 160 MeV. *IEEE Transactions on Nuclear Science*, 45(6), 1998.
- [21] C. Carmichael, J. Fabula, C. Yui, and G. Swift. Consequences and categories of SRAM FPGA configuration SEUs. In *MAPLD 2003*, Washington, D.C., September 2003. Military and Aerospace Programmable Logic Devices International Conference. Paper P21.

- [22] M.S. Tyagi. *Introduction to Semiconductor Materials and Devices*. John Wiley and Sons, New York, 1991.
- [23] V. Eremin, E. Verbitskaya, and Z. Li. Effect of radiation induced deep level traps on si detector performance. *Nucl. Instrum. Meth.*, A476:537–549, 2002.
- [24] John Lajoie, Steve Skutnik, et al. Radiation effects on Xilinx field programmable gate arrays: A study of the applicability of programmable logic for use in the PHENIX VTX detector. (unpublished), 2003.
- [25] HiddenSoft. Autoit software. <http://www.hiddensoft.com/AutoIt>.
- [26] René Brun et al. Root analysis package. <http://root.cern.ch>.
- [27] Richard Reciniello, October 2004. Private communication.
- [28] S. Eidelman et al. Review of particle physics. *Physics Letters B*, 592:1+, 2004.
- [29] Robert Pak, February 2005. Private communication.
- [30] B. B. Back et al. Collision geometry scaling of Au+Au pseudorapidity density from $\sqrt{s_{(NN)}} = 19.6$ Gev to 200 Gev. *Phys. Rev.*, C70:021902(R), 2004.
- [31] J. H. Lee. Rapidity dependent net-proton yields in Au+Au at $\sqrt{s_{(NN)}} = 200$ Gev. *Nucl. Phys.*, A715:482–485, 2003.
- [32] K. Reygers. Glauber monte-carlo calculations for Au+Au collisions at $\sqrt{s_{NN}} = 200$ GeV. Technical report, PHENIX, 2003.
- [33] John D. Jackson. *Classical Electrodynamics*. John Wiley and Sons, New York, third edition, 1999.

ACKNOWLEDGMENTS

I would like to first thank Xilinx, who provided both the XQR2V6000 rad-hard FPGA prototype as well as the FIVIT software used for SEU monitoring (along with the accompanying training) free of charge. Specifically, I owe a debt of gratitude to Carl Carmichael and Brendan Bridgford of Xilinx, who arranged for training with the FIVIT software at Xilinx's corporate headquarters in San Jose and answered many questions that came up during the preparation for the test. Much of the success of this experiment was due directly to their assistance.

I would be remiss, however, if I did not specifically recognize the extensive contribution of my adviser, John Lajoie. His contagious passion and enthusiasm for doing physics, along with his dedication to passing both this love and knowledge on to his students, were a constant source of inspiration throughout my entire education process - both undergraduate and graduate.

In addition, I am grateful to Vladimir Rykov of PHENIX for his assistance in setting up the PISA model and Richard Recinello of BNL Personnel Monitoring, who provided much insight into interpreting badge doses.

Finally, I wish acknowledge the support of the RHIC Collider-Accelerator division and the U.S. Department of Energy for making this all possible.